Spring 5-15-2019

SYMMETRY AND DOPANT DIFFUSION IN INVERTED NANOPYRAMID ARRAYS FOR THIN CRYSTALLINE SILICON SOLAR CELLS

Seok Jun Han
University of New Mexico, Albuquerque

Seok Jun Han

Candidate

Chemical and Biological Engineering

Department

This dissertation is approved, and it is acceptable in quality and form for publication:

Approved by the Dissertation Committee:

Dr. Sang Eon Han , Chairperson

Dr. Sang M Han

Dr. Ganesh Balakrishnan

Dr. Tito Busani

SYMMETRY AND DOPANT DIFFUSION IN INVERTED NANOPYRAMID ARRAYS FOR THIN CRYSTALLINE SILICON SOLAR CELLS

by

SEOK JUN HAN

B.S., Chemical Engineering, Hongik University, 2010
M.S., Chemical Engineering, Pohang University of Science and Technology, 2012

DISSERTATION

Submitted in Partial Fulfillment of the
Requirements for the Degree of

Doctor of Philosophy
Chemical Engineering

The University of New Mexico
Albuquerque, New Mexico

May, 2019

ACKNOWLEDGMENT

I have received generous financial and academic supports for my research from an academic advisor, Dr. Sang Eon Han. He has patiently encouraged me to dive into the physics, such as optics, electrostatics, solid state physics, statistical mechanics, and quantum mechanics, with ample time of thinking, which has served as a precious foundation of this research. Every his theoretical, scientific, valuable and professional criticism has helped me to be mature scientifically as an independent researcher. Also, thanks for teaching me optical simulations using the Comsol which have become one of my precious achieved skills. My second academic advisor, Dr. Sang M. Han, also gave me endless support and encouragement for my research. Whenever I got experimental difficulties, each of his guidelines and approaches from comprehensive knowledge was a significant breakthrough in this research.

I would like to thank my dissertation committee members, Dr. Ganesh Balakrishnan and Dr. Tito Busani, for their great support. Also, thank Dr. Paul Stradins for inviting me to the National Renewable Energy Laboratory for sharing solar cell fabrication processes.

The most of experiments have been done in the Center for High Technology Materials. The cleanroom managers, Douglas Wozniak and Steve Wawrzyniec, taught and helped me for the experiments in the cleanroom. Thanks to them, my research has been progressed seamlessly.

Lastly, I would like to convey my deep sense of gratitude to my family, Mom, Dad, Eunju, and Sang Yoon, for encouraging and supporting me to continue study.

Especially, thank Eunju for being with me with love and understanding and Sang Yoon for being such a good baby boy.

SYMMETRY AND DOPANT DIFFUSION IN INVERTED NANOPYRAMID ARRAYS FOR THIN CRYSTALLINE SILICON SOLAR CELLS

by

SEOK JUN HAN

B.S., Chemical Engineering, Hongik University, 2010
M.S., Chemical Engineering, Pohang University of Science and Technology, 2012
Ph.D., Chemical Engineering, University of New Mexico, 2019

ABSTRACT

In this dissertation, we enhance the efficiency of thin flexible monocrystalline silicon solar cells by breaking symmetry in light trapping nanostructures and improving homogeneity in dopant concentration profile. These thin cells are potentially less expensive than conventional thick silicon cells by using less silicon material and making the cells more convenient to be handled when supported on polymer films. Moreover, these cells are widely applicable due to their flexibility and lightweight. However, for high efficiencies, these cells require effective light trapping and charge collection. We achieve these in cells based on 14-μm-thick free-standing silicon films with light-trapping arrays of nanopyramidal dips fabricated by wet etching.

We break the symmetry of nanopyramids by etch mask design and its rotation with respect to a crystallographic direction in silicon substrate. This approach eliminates the need for using expensive off-cut silicon wafers. We also make use of low-cost, manufacturable, wet etching steps to fabricate the nanopyramidal dips. In our experiment, the new symmetry-breaking approach enhances the cell efficiency by 1.1%.

In light-trapping nanostructures, the texture size is comparable to or smaller than the characteristic diffusion length of a dopant. In this size regime, strong inhomogeneity in the dopant concentration often develops in the pn-junction of the cells. The strong inhomogeneity creates electrically inactive regions in the texture. We improve the homogeneity by diffusing a dopant through selective surface regions exposed by wet etch masks. Our experiments demonstrate that this dopant diffusion method enhances the cell efficiency by 0.8%. This method would be generally applicable for other micro/nano structures, semiconductor materials, and optoelectronic devices.

TABLE OF CONTENTS

LIST OF TABLES

LIST OF FIGURES

1. INTRODUCTION

A solar cell generates electricity from solar radiation. A spectrum of radiative power per unit area perpendicular to the direction of the sun at the position of the outside of the earth's atmosphere is called the solar constant or air mass zero (AM0) radiation. This electromagnetic spectrum is used to research solar cells for space applications, and the total power of air mass zero radiation is 1353 W/m^2 [1]. However, thin crystalline silicon (c-Si) solar cells are widely adopted to terrestrial and mobile applications. As the sunlight passes through the earth's atmosphere, solar irradiance is attenuated because of both Rayleigh scattering of short wavelength lights and light absorption by gases constituting atmosphere. Hence, a solar spectrum at the sea level is a function of total traveled distance through the atmosphere. A pathlength of sunlight through the atmosphere is the shortest when the sun is directly overhead, and this solar spectrum is called air mass one (AM1) radiation. The AM1 radiation is the maximum of solar irradiance we can expect at the sea level. However, it is only a special case that rarely happens. Therefore, the most widely used standard solar spectrum is AM1.5 radiation which is the case when the solar zenith angle is 48.19^o with the power density of 1000 W/m^2 at the sea level. The AM1.5 represents an averaged solar spectrum over a year at mid-latitudes. Figure 1.1 compares the AM0 solar radiation with the AM1.5 solar radiation [2].

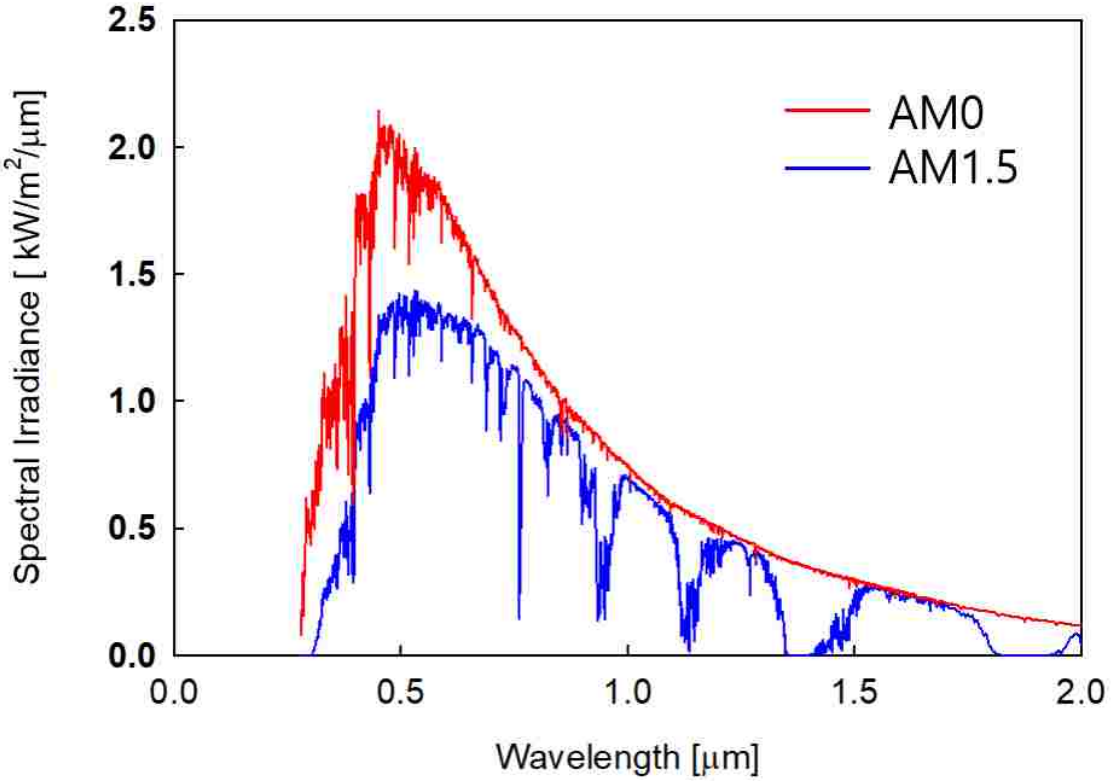

Figure 1.1. The spectral distribution of AM0 (red solid line) and AM1.5 radiation (blue solid line). The AM0 spectrum is measured above the earth's atmosphere, and AM1.5 spectrum is measured at the sea level when the solar zenith angle is 48.19^{o} on a clear day [2].

The large market share (~85%) of crystalline silicon (c-Si) solar cells is expected to continue in the near future [3], and the industry is rapidly moving towards thin crystalline film technologies. The benefit of using thin films is two-fold. The 1st benefit is reduced material cost. The c-Si wafers used in commercial solar cells today are typically 100-300 μm thick and constitute approximately 30-40% of total module cost [4]. Therefore, using thin (~10 μm) c-Si films would provide a substantial cost advantage. The 2nd benefit is reduced weight and great flexibility. A thin c-Si film can

be supported on a light-weight flexible platform instead of conventional thick (~3 mm) glass substrates which constitute most of the module weight. This weight reduction would decrease transportation and installation costs providing savings in the overall balance-of-system costs [5]. In addition to this, a well-known problem of rigid and heavy solar cells is that they are not able to be installed on a curved surface like arched roofs. The lightweight and flexible solar cells can resolve this issue and can be also used for mobile applications, such as clothes, boats, planes, recreational vehicles or military base tents. While the benefits of cost reduction and broader applications are clear, the optical absorption in thin c-Si films is much less than that of thick films. Therefore, the thin c-Si solar cells requires highly efficient light trapping to achieve the comparable level of efficiency of thick films.

A function of solar cells can be divided into two main roles, absorbing sunlight to generate charge carriers and collecting the generated charge carriers as a useful form of energy before charge carrier recombination as depicted in Figure 1.2. Hence, to enhance photovoltaic efficiency, optical pathlength within a solar cell device should be large enough to generate more charge carriers, and the recombination of charge carriers through various mechanisms should be effectively suppressed to increase a charge collection probability. Both aspects of researches, researching optical responses to increase light absorption and researching electromagnetic properties of charge carriers to enhance the charge collection probability, are actively studied. For example, optical studies of solar cells have extensively introduced various light-trapping schemes [6-33]. Also, electromagnetic properties of charge carriers have been actively studied. There are various approaches for passivating a c-Si surface to minimize recombination [34-36].

In the present research, the effects of optical and electrical properties on solar cells will be investigated simultaneously when a light-trapping structure is integrated into a solar cell, because both of the optical and the electrical aspects are equally important to achieve higher photovoltaic efficiency of solar cells.

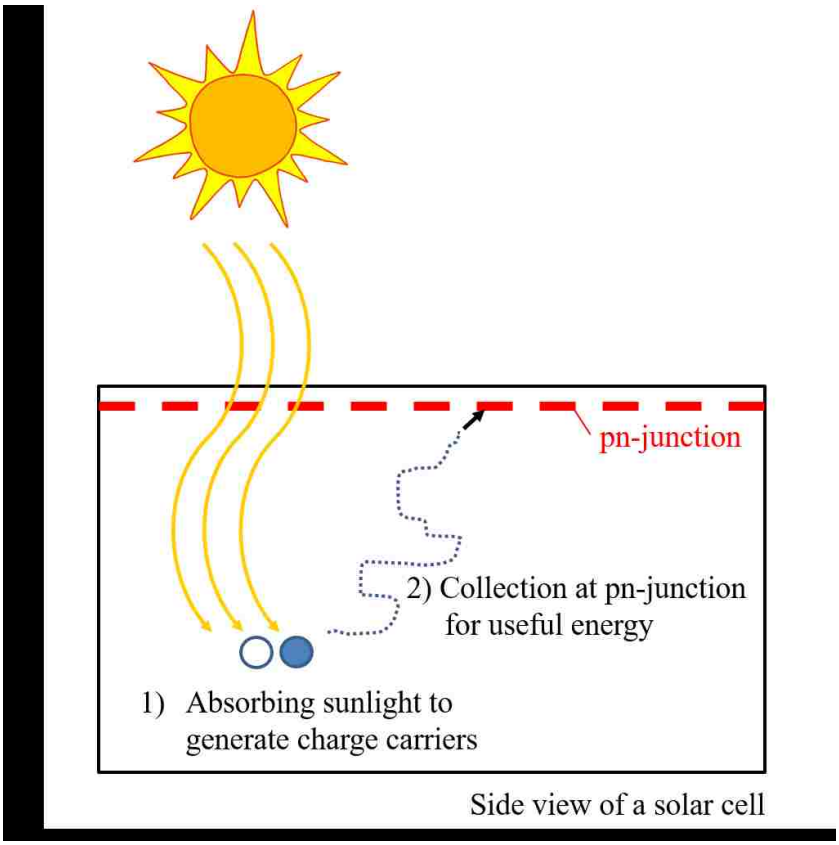

Figure 1.2. A schematic diagram of two main roles of a working solar cell from a cross-sectional view. The first main role of a solar cell is absorbing sunlight to generate charge carriers, and the second main role is collecting charge carriers at pn-junction for a useful form of energy.

The various light-trapping schemes exist today: light scattering by nanoparticles [6-9], random/quasi-random surface corrugation [10-13], nanorod arrays [14-22], and diffraction gratings [24-33]. Firstly, when metal/dielectric nanoparticles are placed on a film [Figure 1.3 (a)], light is efficiently scattered into the underlying film at the resonance frequencies. However, the metal nanoparticles strongly absorb light when they are

placed on weakly absorbing photoactive films [7]. This optical loss limits light-trapping efficiency. In addition to this, the use of metal elements for light trapping cannot be compatible with high-temperature fabrication processes due to sintering of metal. Also, the metal elements, such as gold, silver, or iron, can diffuse into deep silicon and introduce allowed energy levels into the band gap of silicon [37, 38]. These energy levels due to impurities can trap charge carriers in photovoltaics (PV) devices, so recombination of the charge carriers becomes significant. Secondly, the random surface corrugation is another cost-effective manufacturing method to scatter light into the films efficiently [Figure 1.3 (b)]. However, the inherent nonuniformity of a random structure makes it difficult to optimize and improve both electrical and optical characteristics in PV applications [33]. Thirdly, a periodic nanorod array strongly absorbs light, and its optical characteristics can be controlled more systematically compared to the random surface features [Figure 1.3 (c)]. However, the surface recombination of the nanorod structure becomes significant due to its large surface-to-volume ratio [18]. Also, the vertical surfaces of nanorods are difficult to be passivated and metallized by conventional fabrication methods. Lastly, the periodic diffraction grating structure can be fabricated by cost-effective methods, such as nanoimprint or optical lithography [Figure 1.3 (d)]. And, the carefully designed diffraction grating structure can enhance the light absorption of PV devices. Based on the evaluation of various light-trapping schemes, the light-trapping structure for Si-based PV devices should be an impurity-free and periodic diffraction grating nanostructure with a low surface to volume ratio. The inverted nanopyramids structure (shown in Figure 1.4) is a good candidate for light trapping of PV devices because it can satisfy all the criteria above. The applications of inverted

nanopyramids to various types of solar cells are extensively studied [5, 39-42]. It should be noted that macroscopic inverted pyramids can be also used for solar cells, however the physics of light-trapping enhancement is different with that of nanopyramids. In case of macroscopic inverted pyramids, the light trapping can be analyzed by a ray tracing technique [43]. Moreover, the macroscopic inverted pyramid structures which have base size larger than tens of microns are not applicable to thin c-Si solar cells due to a large amount of silicon loss in KOH texturing [39].

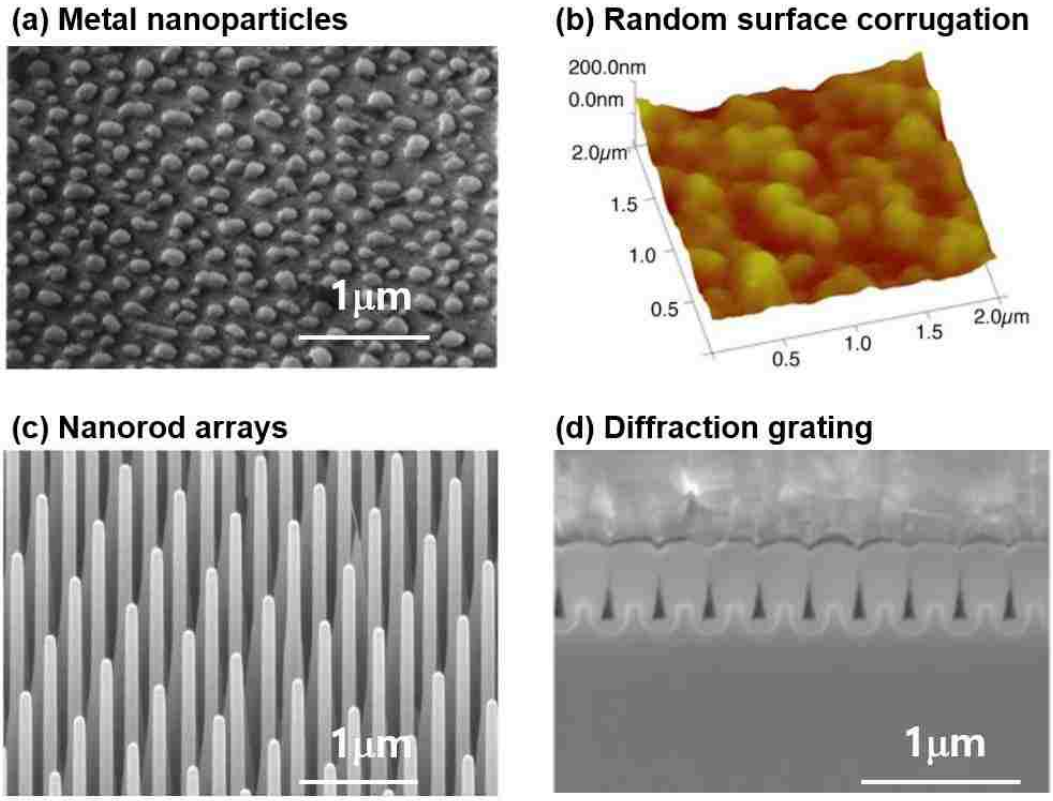

Figure 1.3. Various light-trapping strategies for thin films, (a) scattering by metal nanoparticles [9], (b) random surface corrugation [13], (c) periodic nanorod arrays [23], and (d) diffraction gratings [33].

The light-trapping inverted nanopyramids structure has many unique properties. Firstly, it is cost-effective to be fabricated. The fabrication of the inverted

nanopyramids structure on c-Si takes advantage of intrinsic nature of potassium hydroxide (KOH) wet-etching [44-46]. The etch rate of c-Si(111) is hundreds of times slower than that of c-Si(100). Therefore, after the KOH wet-etching, remaining c-Si(111) surfaces naturally form inverted nanopyramids as shown in Figure 1.4. This conventional wet-etching method with optical lithography to fabricate an inverted nanopyramid array has significant cost advantages compared to fabricating nanostructures with electron/ion beam lithography. Secondly, the inverted nanopyramids structure is entirely compatible with silicon PV device fabrication processes. The inverted nanopyramids structure does not include additional metal/dielectric materials. In other words, the inverted nanopyramids structure after wet etching purely consists of c-Si as shown in Figure 1.4. Hence, we can avoid a risk of contaminating tools and our solar cells' being contaminated by metal during high temperature fabrication processes. Thirdly, the silicon surfaces after the KOH wet-etching are suitable for solar cell fabrication because the number of surface states can be effectively reduced. Generally, the number of surface states is a function of surface area, roughness, and a type of crystalline surfaces [47, 48]. Notice that the surface area of the inverted nanopyramids structure increases only by 1.7 times compared with that of the flat surface. Also, the surfaces of the inverted nanopyramids structure after wet etching are atomically smooth due to intrinsic properties of the KOH wet etching as shown in Figure 1.4. The atomically smooth inverted nanopyramids surfaces can have low density of surface states because the roughness of surface is related to the number of surface states [47, 48]. In addition, the hydrogen terminated silicon atom on c-Si(111) surface has a higher stability than that of silicon atom on c-Si(100) because each silicon

atom on c-Si(111) has only one dangling bond [47]. To summarize, the cost-effectiveness of fabrication, the impurity-free light-trapping structure, the atomically smooth surfaces, the high stability of a hydrogen terminated silicon atom, and the low surface area make the inverted nanopyramids structure suitable to an application of PV devices.

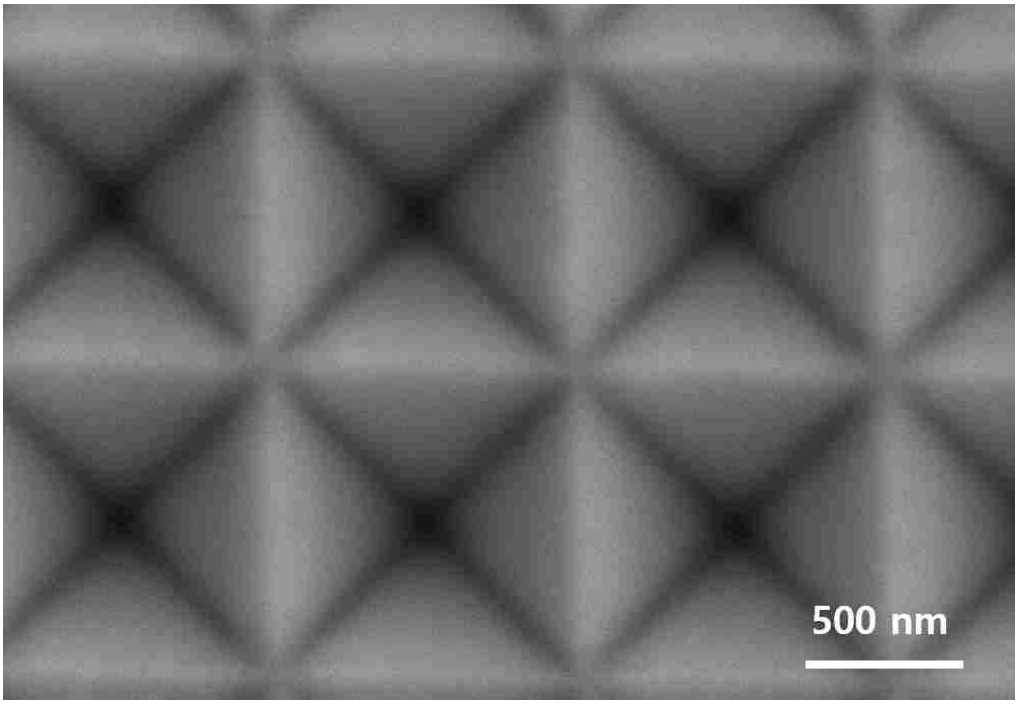

Figure 1.4. A Scanning Electron Microscope image of an atomically smooth inverted nanopyramids structure on crystalline silicon fabricated by potassium hydroxide wet etching. The inverted nanopyramids contain only c-Si(111) surfaces.

The Lambertian limit is a thermodynamic limit of maximum absorption in a film in the geometric optics regime when the surface of the film is assumed as an ideal random scattering media [10, 49]. The enhancement factor of optical path length in a Lambertian film with a bottom reflector is $4n^2$ where n is the refractive index of the film. The Lambertian limit has been compared with many light-trapping structures as a target of light trapping efficiency.

For a successful application of an inverted nanopyramids structure to thin c-Si solar cells, the inverted nanopyramids structure should enhance light trapping without negative effects on the electrical properties of thin c-Si solar cells. For example, a nanorods structure absorbs light effectively, so the light absorption can exceed the Lambertian limit [24]. However, the nanorods structure needs special cares for a solar cell fabrication due to its vertical geometry. For example, the plasma enhanced chemical vapor deposition, pn-junction fabrication, reactive ion etching, and top contact formation on the nanorods structure have challenges for an application to the vertical surfaces. Also, the nanorods structure can have negative effects on the electronic properties of solar cells due to its high surface area to volume ratio. Like this, many research have introduced various light-trapping nanostructures [6-33]. In the present research, we concentrated on the practical value of light-trapping structure specifically for thin c-Si solar cells. Therefore, the effects of inverted nanopyramids structure on both optical and electrical properties of solar cells will be investigated.

Branham *et al*. have already reported a 10-μm-thick c-Si solar cell with 15.7% of photovoltaic efficiency using an inverted nanopyramid array [5]. However, the light-trapping efficiency can be further enhanced when the symmetry of an inverted nanopyramid array is properly reduced. Han *et al.* theoretically showed that proper symmetry breaking in periodic nanostructures enhances light trapping [24, 50]. Symmetry breaking in periodic nanostructures can create new resonant absorption peaks and split degenerate absorption peaks, improving the light absorption over the broad solar spectrum [50-53]. There are many methods for fabricating symmetry-broken nanostructures, such as directional dry etching [52], glancing angle deposition [54], wet

etching on off-cut Si surfaces [55, 56], and multiple exposures in interference lithography [57]. However, fabricating such structures in a scalable, cost-effective, and manufacturable manner remains elusive. Therefore, to further enhance the light trapping of inverted nanopyramids structure, a new approach to systematically break the symmetry in an inverted nanopyramid array will be introduced. The new approach introduced in this study relies on simple and low-cost wet-etch processing steps, which are unnecessary to use expensive off-cut Si wafers. Based on the new symmetry breaking approach, the thin c-Si solar cells with various symmetries of inverted nanopyramid arrays will be fabricated.

The effects of inverted nanopyramids on the electronic properties of solar cells will be also investigated. A diffusion process is commonly used to fabricate a pn-junction in a textured surface of solar cells. In this case, strong inhomogeneity in dopant concentration typically develops along the textured surface when the structural dimension of the texture is comparable to or smaller than the characteristic diffusion length. The inhomogeneity in dopant concentration results in locally overdoped and/or underdoped regions which decrease photovoltaic efficiencies of the solar cells. Moreover, because overall charge concentration is high in thin cells with efficient light-trapping structures, the volume fraction of such inactive regions is high in thin films, potentially resulting in significant degradation in photovoltaic efficiency. To fully harness the advantage of such light-trapping structures, we introduce a unique method for rendering the doping concentration uniform by diffusing a dopant through selective regions of the light-trapping structure.

2. LITERATURE SURVEY

2.1. Symmetry Breaking of Periodic Nanostructures for Thin c-Si Solar Cells

Periodic and random structures have been compared for their light-trapping performance [33, 58, 59]. The performance of the two is found to be similar to each other for silicon photovoltaics. However, it should be limited to the specific structures used in the studies. The reason is that depending on the geometry and scale, periodic structures may provide greater light trapping than random structures and vice versa. Additional complexity in this comparison is that controlling the spatial correlation in random structures has been found to improve the light-trapping efficiency over both periodic and random structures [11, 12, 60, 61]. However, the correlation control requires rather expensive fabrication techniques. Compared to the random structure, the PV characteristics can be controlled more systematically by introducing periodic nanostructures.

Han *et al.* recently reported that proper symmetry breaking in periodic nanostructures enhances light trapping [24, 50]. Figure 2.1 shows the calculated photovoltaic efficiencies of various structures with respect to their effective thickness. The solid black line shows the calculated efficiency of the nanopyramids structure which has 4-fold rotation axis and four mirror planes (C_{4v} symmetry). The symmetry group is denoted by the Schönflies notation. The skewed nanopyramids structure is non symmetric (C_1 symmetry), and the calculated efficiency (solid red line) is close to the Lambertian limit (black dashed) as shown in Figure 2.1. Symmetry breaking in periodic nanostructures can create new resonant absorption peaks and split degenerate absorption peaks, which is improving the light absorption over the broad solar spectrum. T. Cai *et*

al. also reported that the absorptance in thin silicon films increases as a symmetry of nanostructures is reduced from C_{4v} to C_1 as shown in Figure 2.2 [50]. It should be noted that symmetry breaking in macroscopic structures is also found to enhance absorption, but the physics of enhancement is fundamentally different [53, 62].

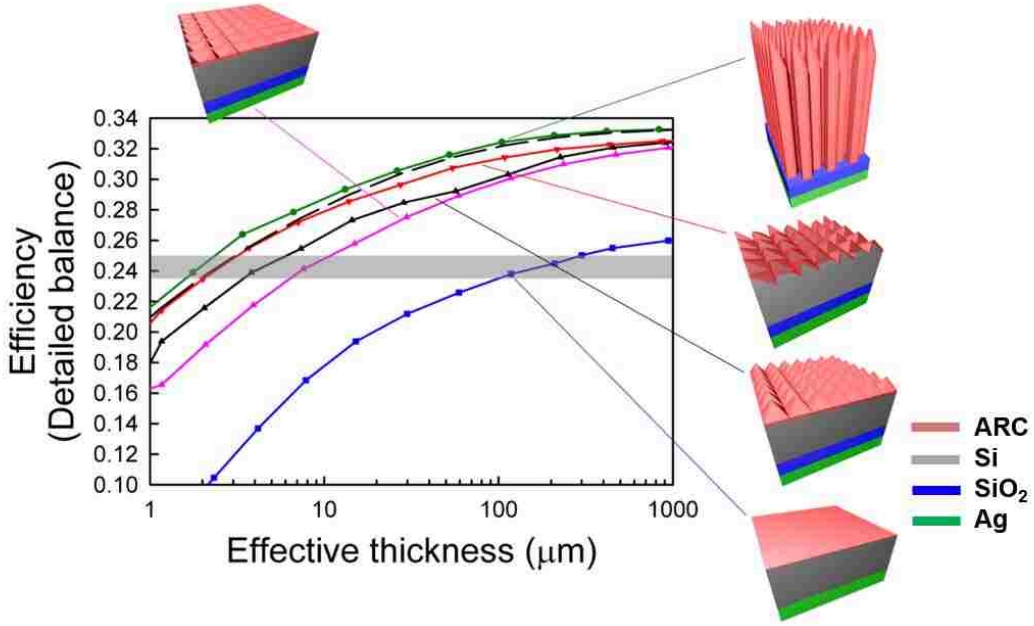

Figure 2.1. Calculated efficiencies of various structures as a function of their effective thickness based on the mass of Silicon. Each structure has an Ag back reflector and a 61-nm-thick silicon nitride anti-reflective coating (ARC) layer. A flat surface, inverted pyramids, pyramids, skewed pyramids, and rods structures are represented as solid blue line, solid pink line, solid black line, solid red line, and solid green line, respectively. As the symmetry of the pyramid structure is reduced to the skewed pyramid structure, the calculated efficiency approaches to the Lambertian limit (dashed black line) [24].

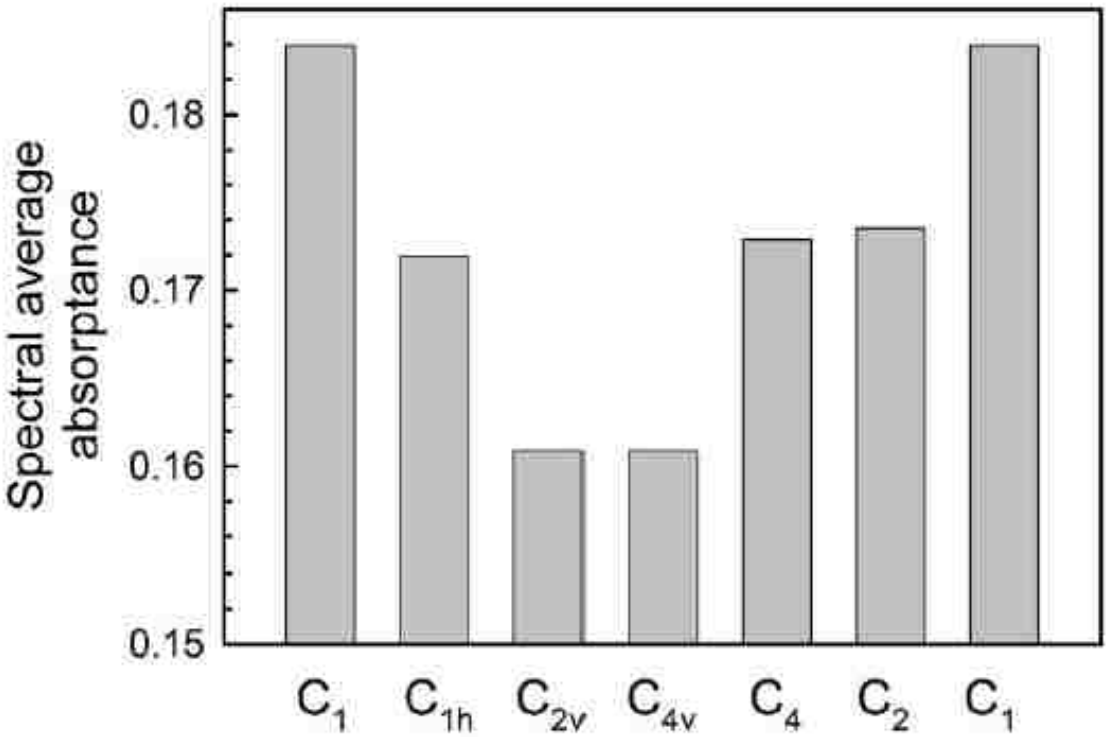

Figure 2.2. Absorptance in Si averaged over the spectrum between 0.7 and 1.0 μm for incidence of unpolarized light [50]. As the symmetry of nanostructure is reduced from C_{4v} to C_1, the absorptance increases.

2.2. Recombination of Charge Carriers

Concentration of charge carrier is in an equilibrium between charge carrier generation and recombination under the dark. When the light is incident on a c-Si layer, pairs of an excess electron and an excess hole are generated. The generated electrons and holes due to the incidence of light are called as excess charge carriers because their numbers are more than their equilibrium values and are relatively free to move in a semiconductor at room temperature. A reverse process is recombination of a pair of an electron and a hole eliminating charge carriers. The concentration of charge carrier is in a steady state between the generation and recombination processes under the light. To maximize the number of charge carriers at the steady state, the recombination should be effectively suppressed, and there are four recombination mechanisms, bulk

recombination, Auger recombination, recombination by a trap, and recombination at surfaces.

As the name indicated, the bulk recombination happens in bulk regions of silicon. It is not related to fabrication processes but related to a quality of the c-Si substrate. Minority carrier lifetime, the averaged time for a charge carrier to stay before recombining, is the most important specification related to the bulk recombination. High-quality and ultra-pure c-Si wafers which have minority carrier lifetime longer than a millisecond are required to fabricate a good efficiency solar cell.

Auger process is recombination of an electron-hole pair giving excess energy to a second electron or a hole instead of emitting a photon as shown in Figure 2.3 [63, 64]. The energetic second electron or hole relaxes back to an initial state by emitting phonons. Because the Auger recombination involves the additional second charge carrier, a probability of the Auger recombination is proportional to $n^2 + np$ where n is concentration of excess electrons and p is concentration of holes. Due to the second order in n, it is generally effective in highly doped regions. Hence, the Auger recombination should be carefully considered during the diffusion processes for fabricating a pn-junction or an interfacial region for metal ohmic contact. When a quality of a c-Si substrate is good, namely the bulk recombination is not significant, the Auger recombination is one of the major recombination processes for c-Si solar cells.

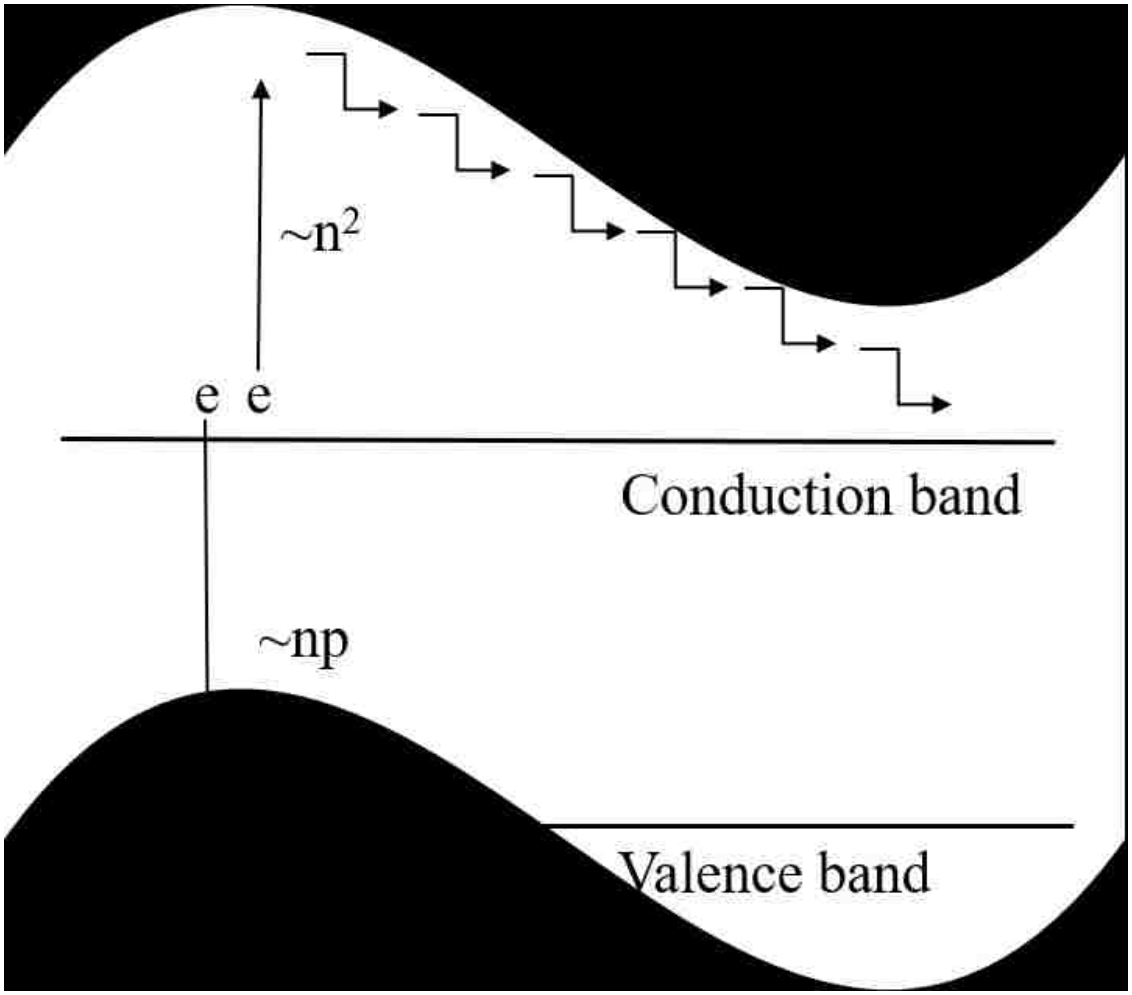

Figure 2.3. A schematic diagram of Auger recombination [63]. The probability of involving both an excess electron and a hole in recombination is ~ n × p, and the probability of a 2nd excess electron being next to the recombining electron is ~n^2. The energetic 2nd electron relaxes back to an initial state by emitting phonons.

Impurities in silicon introduce allowed energy levels within a band gap of c-Si. The impurities which are easily exposed from other users or an environment in a cleanroom at the Center for High Technology Materials (CHTM) have been summarized in Figure 2.4. Notice the metal impurities, Ag, Au, and Fe, introduce energy levels close to the gap center of c-Si. These impurity levels are detrimental for solar cell efficiency because the probability of trapping both an excess electron and a hole in the

impurity levels near the gap center is significant. In addition to this, the diffusivities of Ag, Au, and Fe in Si are ranged from 10^{-10} to 10^{-6} cm^2/s at 900 ^oC [37]. Compared to other impurities, such as boron or phosphorus, the diffusivities of these metals are 10^6-10^{10} times higher. Hence, the contamination of Ag, Au, and Fe should be avoided for the efficiency of solar cells. In this research, a protective layer or a diffusion barrier is used for high-temperature processes to minimize the contaminations from environments.

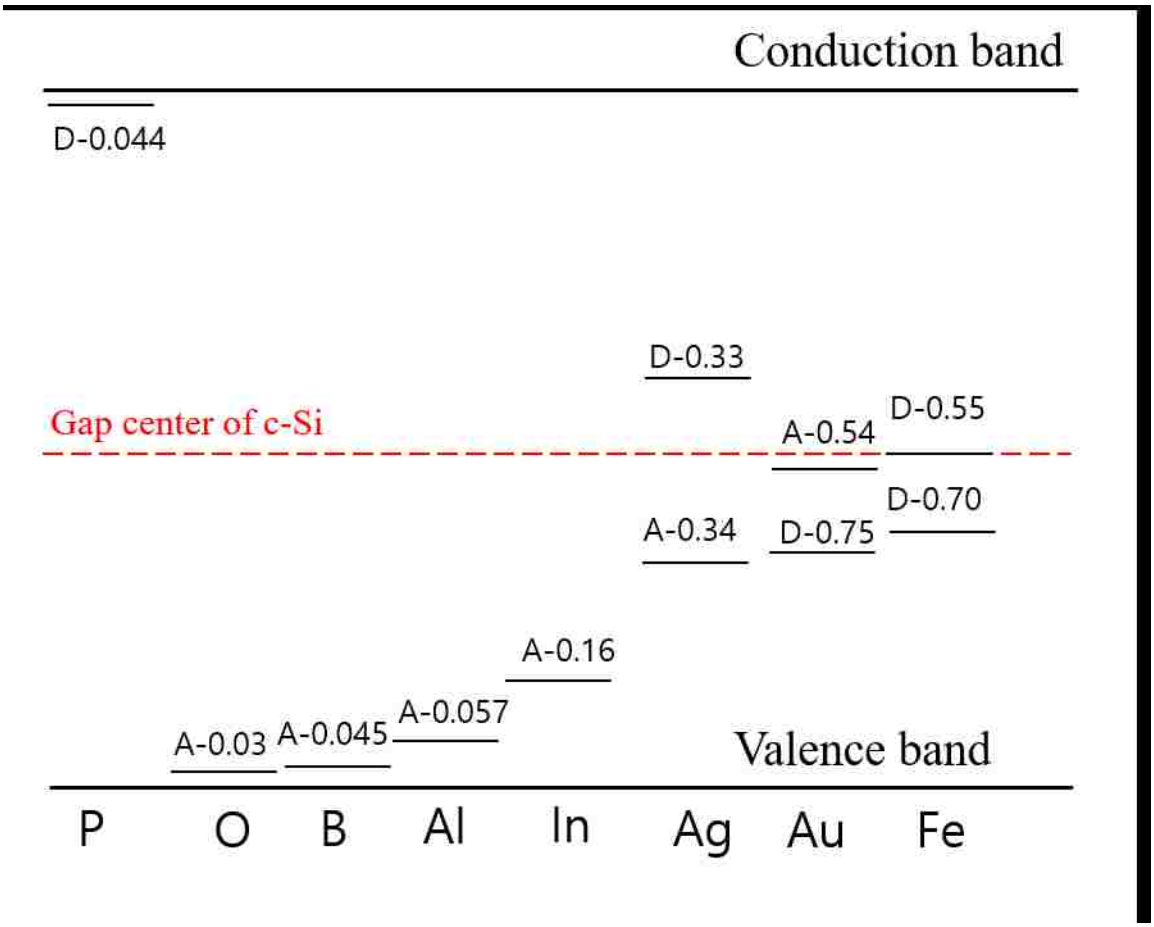

Figure 2.4. Introduced energy levels within a band gap due to various impurities in c-Si. Capital letters, A and D, represents an acceptor level and a donor level, respectively. The numbers next to A- & D- indicate energy difference in eV from a valence band (for acceptor levels) or from a conduction band (for donor levels) [38].

A discontinuity in an array of silicon atoms can be represented as severe defects. This abrupt change in a structure or a periodicity introduces many surface quantum states. In addition to this, dangling bonds of a silicon atom on a surface of Si are associated with interfacial states of electrons. These surface states are within the band gap of c-Si, and suppressing the surface recombination of charge carriers is critical for the high efficiency of solar cells. To suppress the recombination, Nemeth *et al.* introduced a method of polycrystalline silicon (poly-Si) passivation for high-efficiency solar cells [35]. Figure 2.5 shows the concentration profile of doped phosphorus atoms and hydrogen atoms in the triple layer of poly-Si/SiO_2/c-Si. The most of interfacial states are saturated with oxygen bonds by a thermally grown tunneling SiO_2 layer [34, 35]. Because the SiO_2 layer is grown from an underlying c-Si substrate, the periodicity at the interface changes gradually, and the number of the interfacial states is minimized. The remaining interfacial states are further decreased with hydrogen bonds through the forming gas annealing. The properly doped polysilicon passivating layer serves as an inter-layer for an ohmic contact between metal and c-Si [35]. The structural resemblance between c-Si and crystallized poly-Si effectively suppresses the number of surface states. This surface passivating technique is used in the National Renewable Energy Laboratory (NREL), and we adapted it for an application of a solar cell research in the Center for High Technology Materials (CHTM).

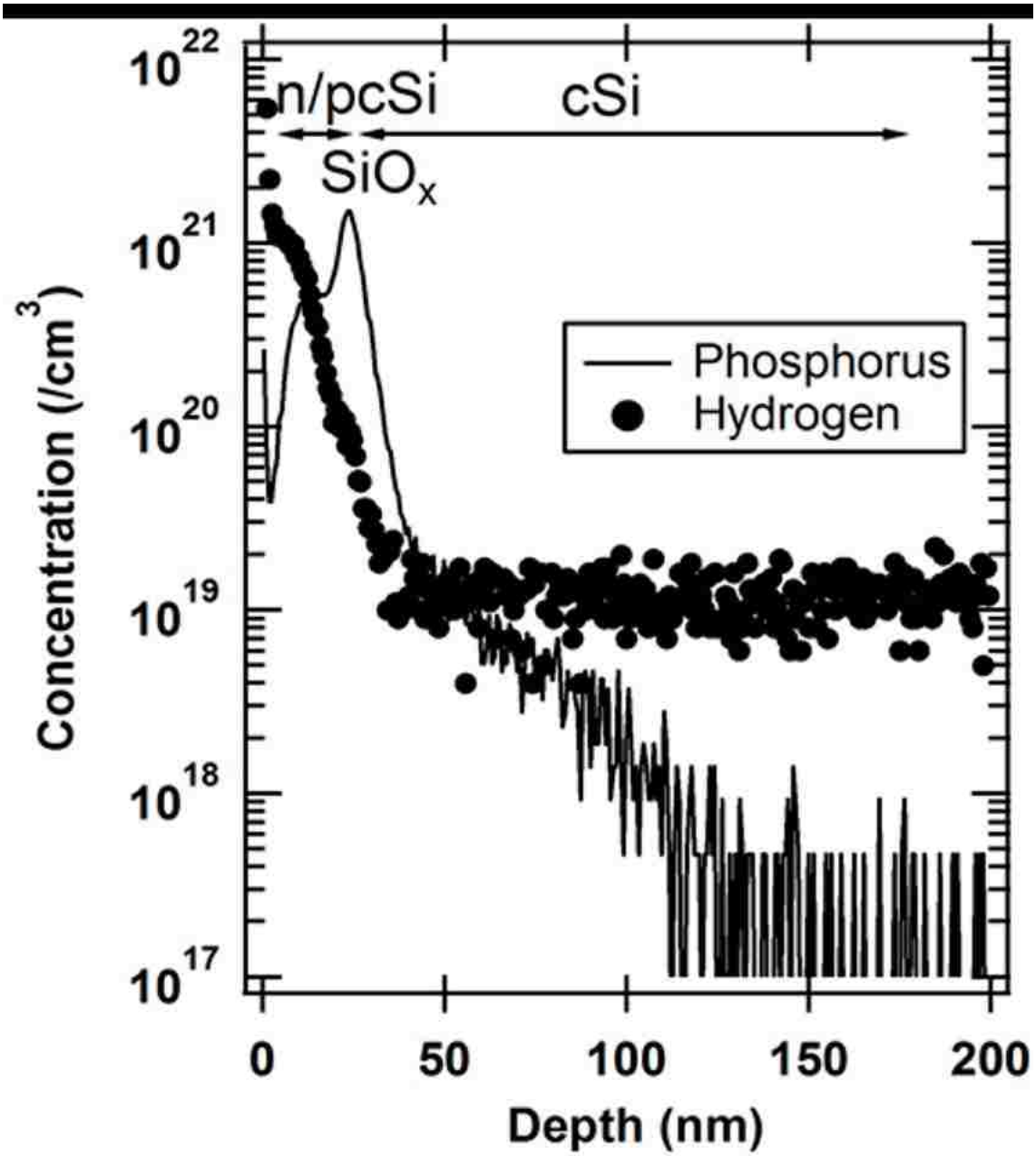

Figure 2.5. The concentration profile of phosphorus and hydrogen atoms along the depth after diffusion and forming gas annealing [35]. The hydrogen concentration represents the concentration of Si dangling bonds terminated by a hydrogen atom. A phosphorous concentration fluctuates at the interface of a tunneling SiO_2 layer which serves as a diffusion barrier.

The diffusion of phosphorus or boron for fabricating a pn-junction or an ohmic contact can introduce the dead layers. The dead layer is a region where dopant precipitation, aggregation of excess dopants into clusters, occurs resulting in a low charge

collection probability. Figure 2.6 shows concentration profile of electrically active phosphorus (P) in silicon after pre-deposition. It clearly shows there is a limit of active P concentration at ~ 4.5×10^{20} regardless of processing time [65]. This upper limit of active dopant concentration (n_e) is equal to the solubility of P in silicon at the temperature of diffusion. Solmi *et al*. experimentally determined the equilibrium concentration of phosphorus (C_{sat}) with phosphorus precipitates as a function of temperature [66]. Because the equilibrium concentration of phosphorus (C_{sat}) is higher than the upper limit of active dopant concentration (n_e) at the temperature higher than 750 ^{o}C as shown in Figure 2.7 [66], the inactive dopant region is easily developed during dopant diffusion. The inactive dopant region significantly reduces charge carrier lifetime so forms the dead layers [67]. This problem becomes more significant when light-trapping nanostructures are applied to solar cells. During making a pn-junction along the nanostructure by dopant diffusion, inhomogeneity in dopant concentration develops significantly due to a geometric effect of the nanostructure. Moreover, because overall charge concentration is high in thin cells with efficient light-trapping structures, a volume fraction of such inactive regions is high in thin films, potentially resulting in significant degradation in photovoltaic efficiency. In this study, the doping inhomogeneity problem due to an inverted nanopyramid array will be discussed in Section 3.4.1, 3.4.3, 4.2, and 4.3.

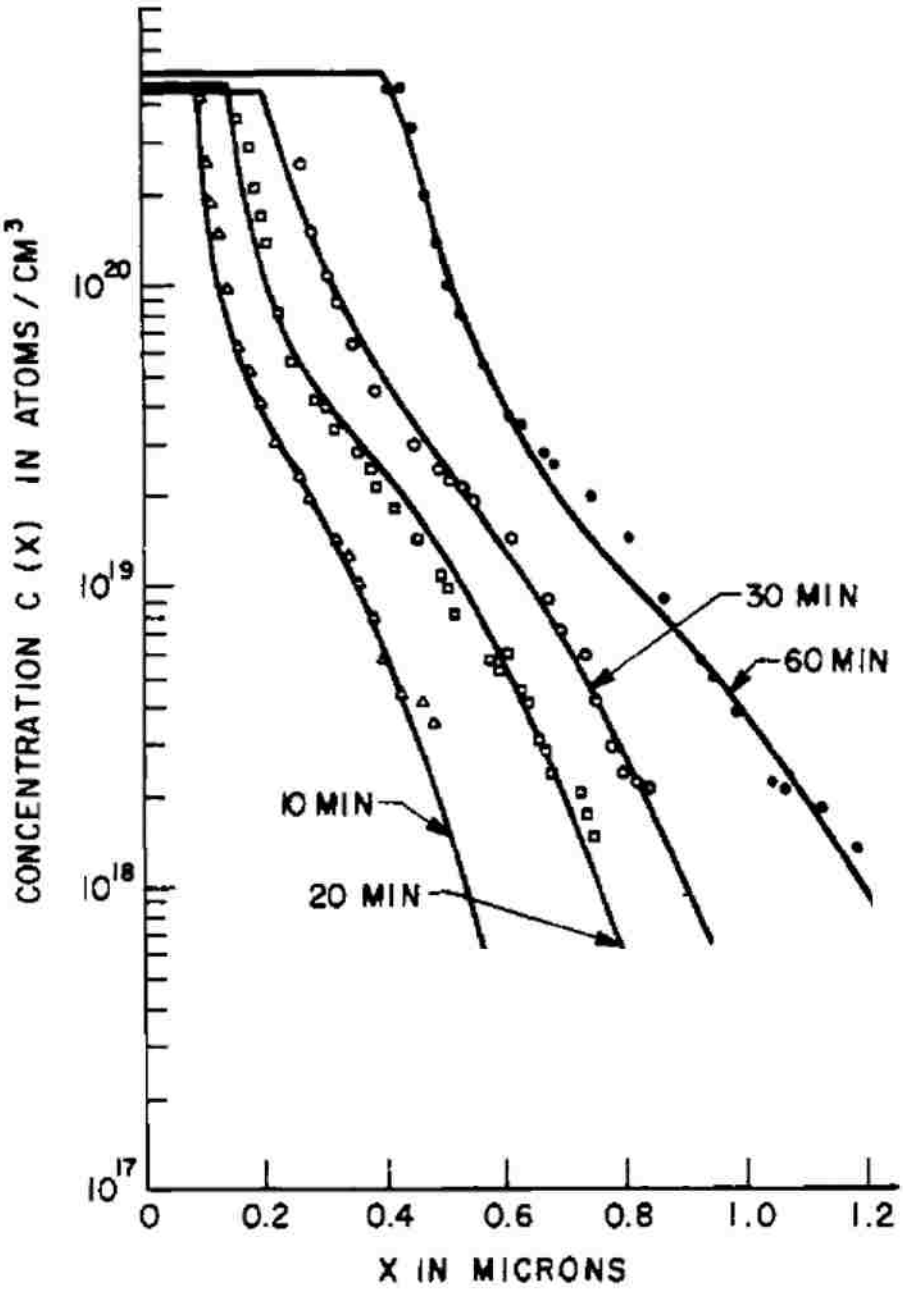

Figure 2.6. The concentration profile of active phosphorous after diffusion using $POCl_3$ source at 950 ^oC for 10, 20, 30, and 60 minutes [65]. The upper limit of active phosphorus is relatively insensitive to the time of diffusion but a function of solubility at diffusion temperature.

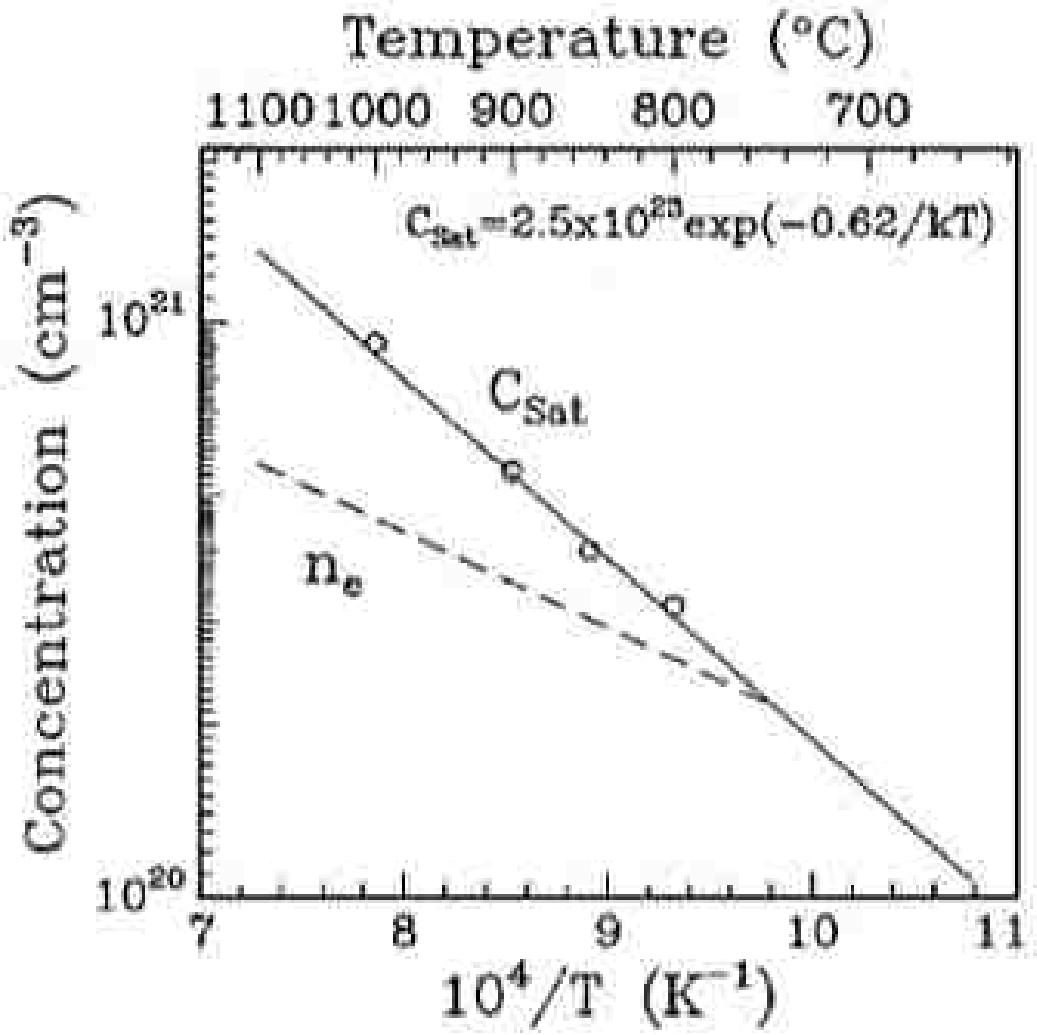

Figure 2.7. Dependence of upper limit of active dopant concentration (n_e) and experimentally determined saturation concentration of phosphorus (C_{sat}) on diffusion temperature [66]. Due to the difference of between C_{sat} and n_e at high temperature, the inactive dopant regions develop.

3. EXPERIMENT

3.1. Wafer Preparation and Cleaning

A c-Si wafer should be carefully chosen for fabrication of semiconductor devices. The impurities commonly found in a c-Si wafer are Aluminum (Al), Boron (B), Carbon (C), Chromium (Cr), Iron (Fe), Manganese (Mg), Nickel (Ni), Phosphorus (P), Titanium (Ti) and Vanadium (V) [60], and the concentration of impurities ranges from 10^{10} to 10^{17} elements/cm^3 [68]. The impurities and defects in a semiconductor introduce allowed energy levels within a band gap of c-Si as described in Section 2.2. Charge carriers in a semiconductor are easily trapped and recombined in these defects or impurities levels [69]. The recombination significantly decreases minority carrier lifetime in a semiconductor; hence it results in poor device efficiency. For high device efficiencies, silicon must not only be very pure but also be in a single-crystal form with essentially zero defects in the crystal structure. The methods used to produce a high-quality crystalline silicon ingot from polysilicon pellets are Czochralski and Float-zone processes [70]. A Float-zone silicon wafer is extremely pure silicon obtained by a vertical zone melting technique [71, 72]. The Float-zone process produces high-quality c-Si wafers for applications of photovoltaic devices as an alternative to the Czochralski method.

In this study, a boron-doped Float-zone c-Si(100) wafer with minority carrier lifetime longer than a 1 millisecond was used for solar cell fabrication. Diameter and thickness of the wafers were 4-inch and ~250 μm, respectively. The doping level of boron was about 10^{15} elements/cm^3, and the resistivity of the wafer is 1-10 ohm-cm.

The c-Si wafer was pre-treated and cleaned by the methods shown in Table 3.1 at the beginning/middle (if necessary) of solar cell fabrication processes. The c-Si

substrate surface can have irreversible damages from high-temperature processes, and these damaged surfaces are removed by isotropic etching and/or plasma etching and/or thermal oxidation. The recipes and roles of c-Si wafer treating processes used in this study are summarized in Table 3.1. In addition to this, the cleaned wafer should be carefully handled to avoid contaminations from the environment. We employed extremely clean tweezers and quartz/glass beakers which were dedicated to each step of cleaning to prevent contaminations of c-Si wafers.

Table 3.1 Cleaning processes for a c-Si wafer used in this research

Process	Recipes	Temperature and duration	Roles
Deionized water rinse	Deionized water	Room temperature for 10 minutes	Rinsing in a flowing batch
Buffered oxide etching (BOE)	20:1 volume ratio of 40% ammonium fluoride and 49% of hydrofluoric solution	Room temperature for a minute	Removing native and chemically grown silicon oxide layer
Piranha Cleaning	3:1 volume ratio of 98% sulfuric acid and 30% hydrogen peroxide	80 ^{o}C for 10 minutes	Removing organic residues
RCA1 cleaning	5:1:1 volume ratio of deionized water, ammonium hydroxide, and 30% hydrogen peroxide	80 ^{o}C for 10 minutes	Removing organic residues
RCA2 cleaning	7:1:1 volume ratio of deionized water, 37% hydrochloric acid, and 30% hydrogen peroxide	80 ^{o}C for 10 minutes	Removing metallic contaminants
Isotropic etching	300:1 volume ratio of HNO_3 and HF	Room temperature for a few minutes	Cleaning of damaged c-Si
Plasma cleaning	O_2 chemistry	Room temperature for a few minutes	Removing organic compounds
RIE etching	CHF_3/O_2 chemistry	Room temperature for a few minutes	Cleaning of damaged c-Si
Thermal oxidation	O_2 100% dry	at 800-1000 ^{o}C for 10 minutes	Cleaning of damaged c-Si

3.2. Crystalline Si Wafer Thinning

Commercially available thin c-Si wafers are expensive and limited to specific types of wafers. For example, the University Wafers supplies wafers thinner than 50 μm, and the price started from $1376 for a 4-inch diameter wafer in 2017. Besides, these expensive thin wafers are limited to a specific type of wafers, which does not offer various specifications of c-Si wafers, such as minority carrier lifetime, type of dopant, diameter, thickness, and resistivity. We have employed thinning of c-Si wafers to resolve these problems. Extremely clean quartz wares including 2-liter beakers and 4-inch sample holders were used in this study. Figure 3.1 shows the thinning system where c-Si wafers were etched by potassium hydroxide (KOH). We used semiconductor grade 50 wt.% of KOH solution [73], and the solution in a quartz beaker was heated to the targeted value, 90 ^{o}C, on a hot plate by a proportional integral derivative (PID) controller with resistance temperature detectors (RTD). Stirring of the solution was necessary before wafers were dipped into the KOH solution to decrease response time and hysteresis of PID control. When the temperature reached targeted value, 4-inch c-Si wafers on a quartz holder were immersed into the KOH solution for thinning.

Figure 3.1. A photograph of a 4-inch c-Si wafer on a quartz sample holder in the middle of thinning. The vigorously formed hydrogen bubbles mix the solution effectively at 90 ^{o}C in 50 wt.% KOH solution.

A rate-determining step of KOH etching is the surface reaction [74], so the thickness uniformity after etching will mainly depend on the temperature gradients of the solution. Although the reaction rate is not limited by the transport of reactants in KOH solution, forming a gas phase bubble on the c-Si surface still can cause thickness nonuniformity. As KOH etches the c-Si, hydrogen bubbles form and block the c-Si surface, which can cause nonuniformity on the c-Si surfaces. In this case, a higher temperature of the solution will help to enhance the uniformity of c-Si surfaces because vigorously formed hydrogen bubbles agglomerate and leave quickly from the surface,

and the phase separation effects are averaged out over the entire regions of c-Si surfaces. H. Tanakaac *et al.* reported that the higher temperature and concentration of KOH solution help to fabricate a smooth surface after c-Si(100) etching [75]. The floating hydrogen bubbles near the surface of c-Si enhance convection in the solution, hence the additional stirring is not necessary to decrease temperature gradients while the thinning is being performed. We measured the thickness at various positions (more than 9 points) over 10 $inch^2$ area on a 4-inch thinned c-Si wafer to check the flatness of thinned wafer using a Peacock thickness gauge. The variation of thickness with respect to the positions of the wafer was negligible in our experiment.

We conducted the KOH thinning on mildly doped p-type c-Si wafers. Unless the wafer is heavily doped with boron, the KOH etch rate does not significantly depend on the type and the concentration of dopant. However, the KOH etch rate is slow on a heavily boron-doped Si wafer because of a high activation energy [76]. Hence, the thinning introduced in this Section can be applied to most c-Si wafers unless the c-Si wafer is heavily boron-doped. We will control the etch rate by boron doping in light-trapping structure fabrication as detailed in Section 5.2. To obtain a thinning rate, the thickness of c-Si wafers has been measured before and after KOH thinning by a peacock thickness gauge station. We were able to obtain 50-μm-thick 4-inch wafers without breaking them at a success rate of 90%. Figure 3.2 shows the wafer thickness as a function of etching time, and the determined thinning rate was about 60 μm/hour/side. A free-standing 50-μm-thick 4-inch c-Si wafer was mechanically strong enough to be handled in the solar cell fabrication processes. Figure 3.3 shows a 50-μm-thick 4-inch wafer held by tweezers without being bent or broken.

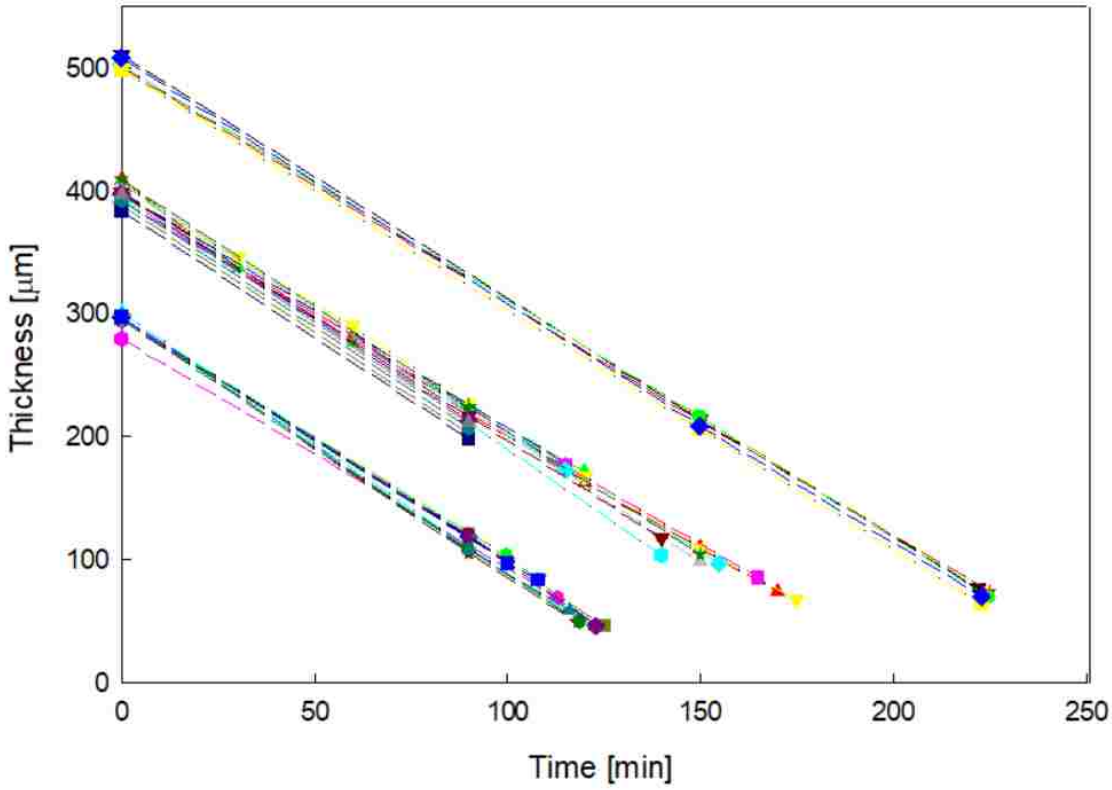

Figure 3.2. The thickness of wafers as a function of etching time at 90 ^{o}C in 50 wt.% KOH. Thirty-three c-Si wafers were thinned down one by one, and the etch rate was about 60 μm/hr/side.

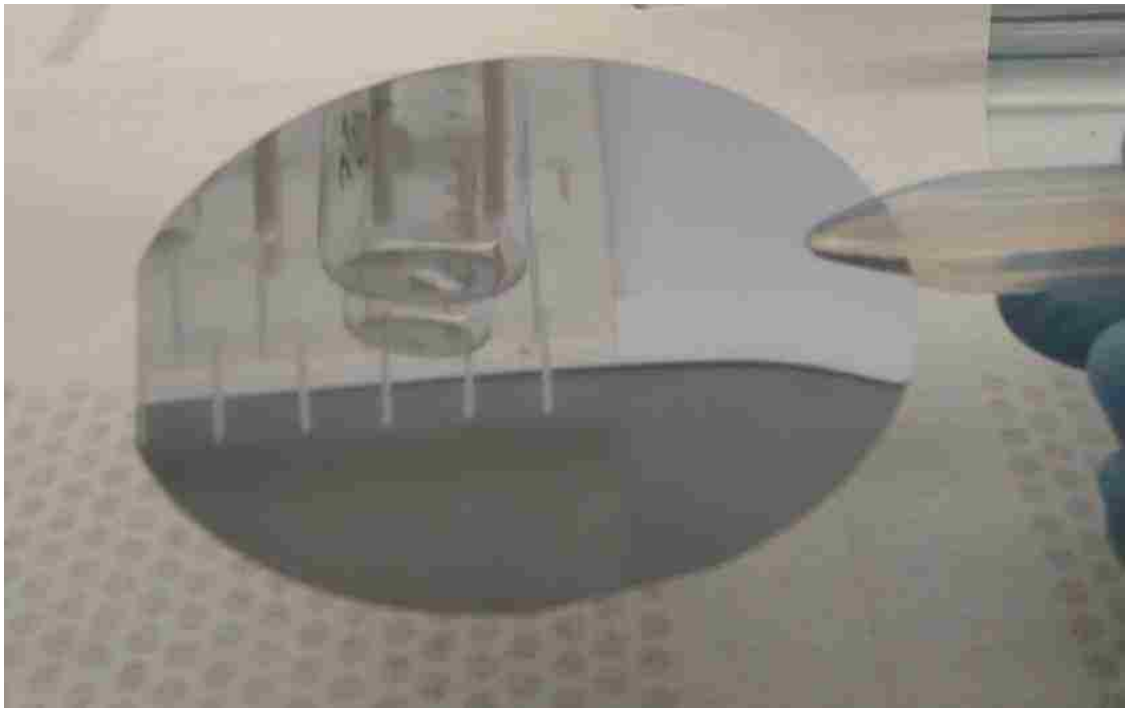

Figure 3.3. A free-standing 50-μm-thick 4-inch c-Si wafer. The thinned c-Si wafers can be handled by tweezers without being bent or broken.

We measured surface roughness of the thinned c-Si wafer by the Dektek profilometer because nanopatterning by an interference lithography (IL) system can be affected by the surface roughness of thinned wafers. The measurement was performed after calibration with 1-μm and 50-μm standard samples. The pictures of c-Si wafers in Figure 3.4 (a) and (c) show that the mirror-like polished surface was conserved well after KOH thinning. We analyzed heights of the surface a Dektek Profilometer [Figure 3.4 (b) and (d)], and the scanned length was 1000 μm with 2000 data points. The heights of wafer after thinning fluctuated by 20-40 nm over local points. This roughness amplitude of the thinned c-Si surface was much shorter than the wavelength of IL laser (355 nm, YAG-Nd laser, Infinity 40-100, Coherent Inc.). Therefore, the thinning did not have any issues on IL nanopatterning. Figure 3.4 (e) shows a good quality of IL nanopatterns on a thinned 50-μm-thick wafer.

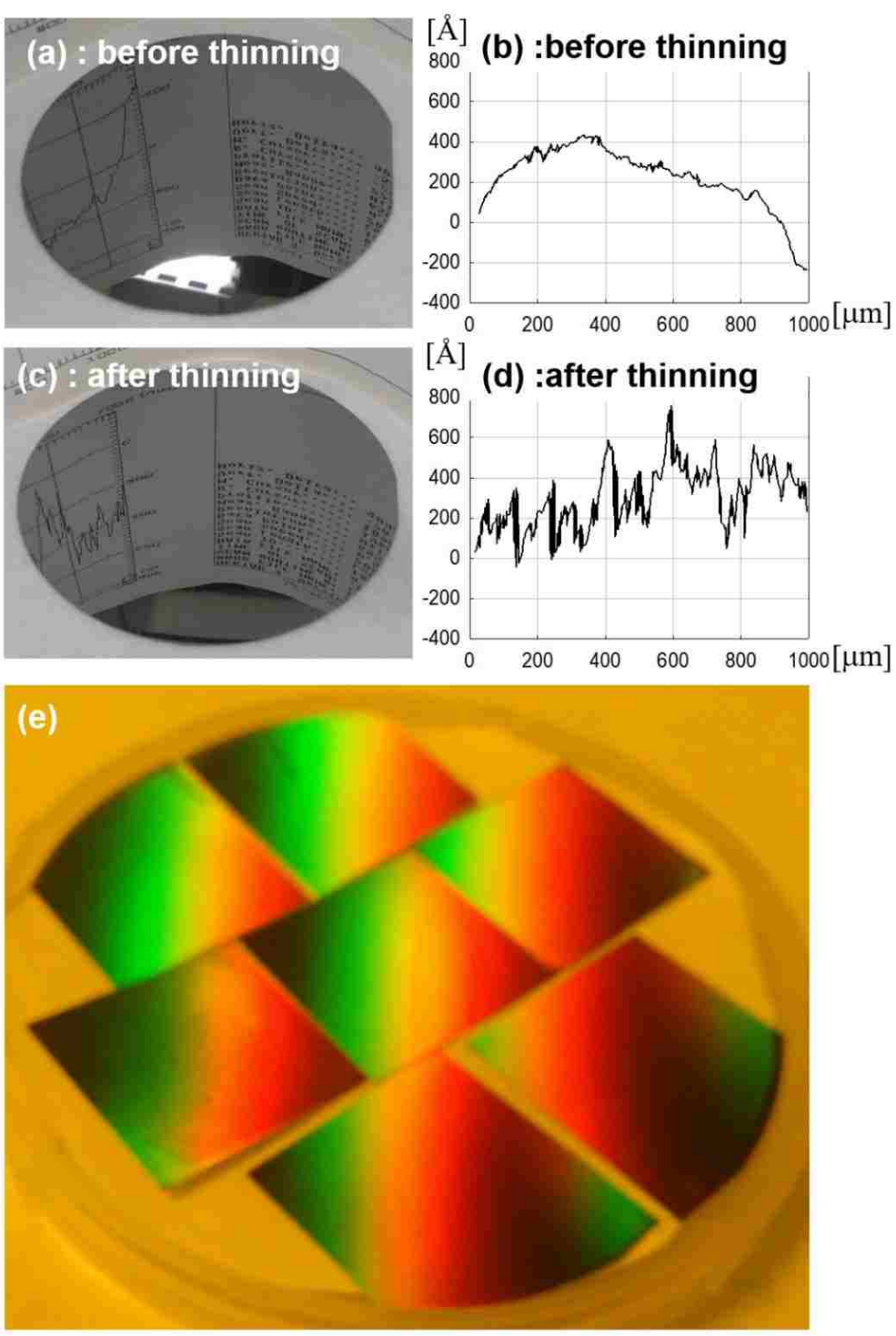

Figure 3.4. A photograph of the c-Si wafer before (a) and after (c) thinning. The polished surface is conserved well after thinning. The reflected mirror image on thinned c-Si wafer (c) indicates that the surface is polished-like. Dektek Profilometer height scans before (b) and after (d) thinning. (e) shows a photograph of uniform IL nanopatterns on thinned 50-μm-thick wafers.

The minimum thickness of a 4-inch c-Si wafer achieved by the thinning without any technical difficulties was about 50 μm. To further thin down to 10-20 μm, a whole 4-inch wafer was firstly thinned down to 50 μm and then cleaved into 2-inch^2 size pieces for further thinning. This two-step approach can achieve an ultra-thin transparent c-Si wafer without any problems. A polished surface before thinning remained as polished-like surface after thinning to 10 μm. The wafer was not only flexible as shown in Figure 3.5 (a) and (b) but also transparent to yellow and green light as shown in Figure 3.5 (c) and (d). The solar cells based on this flexible c-Si film offer unique properties distinguishable from the conventional c-Si solar cells which are usually unbendable and rigid. For example, the free-standing thin c-Si wafers can be contoured on highly curved surfaces. It is discussed in Section 5.2 as future work.

A free-standing 10-μm-thick thinned c-Si wafer can be handled without much difficulty in the texturing and cell fabrication processes. The detailed process for texturing and solar cell fabrication is described in Section 3.3 and Section 3.4, respectively. Figure 3.6 (a) shows a scanning electron microscopy (SEM, JSM-IT100, Jeol) image of an inverted nanopyramid array on a 10-μm-thick thinned c-Si wafer. We characterized symmetries, periodicities, and lattice types of an inverted nanopyramid array from a top view of SEM images, and Figure 3.6 (a) shows lattice constants of a rectangular lattice (800 nm × 870 nm). Also, we used an optical microscopy or an SEM to accurately measure the thickness of thinned c-Si wafer as an alternative to a profilometer and a peacock thickness gauge. Figure 3.6 (b) shows an SEM image of a 9.4-μm-thick thinned c-Si wafer with an inverted nanopyramid array from a side view.

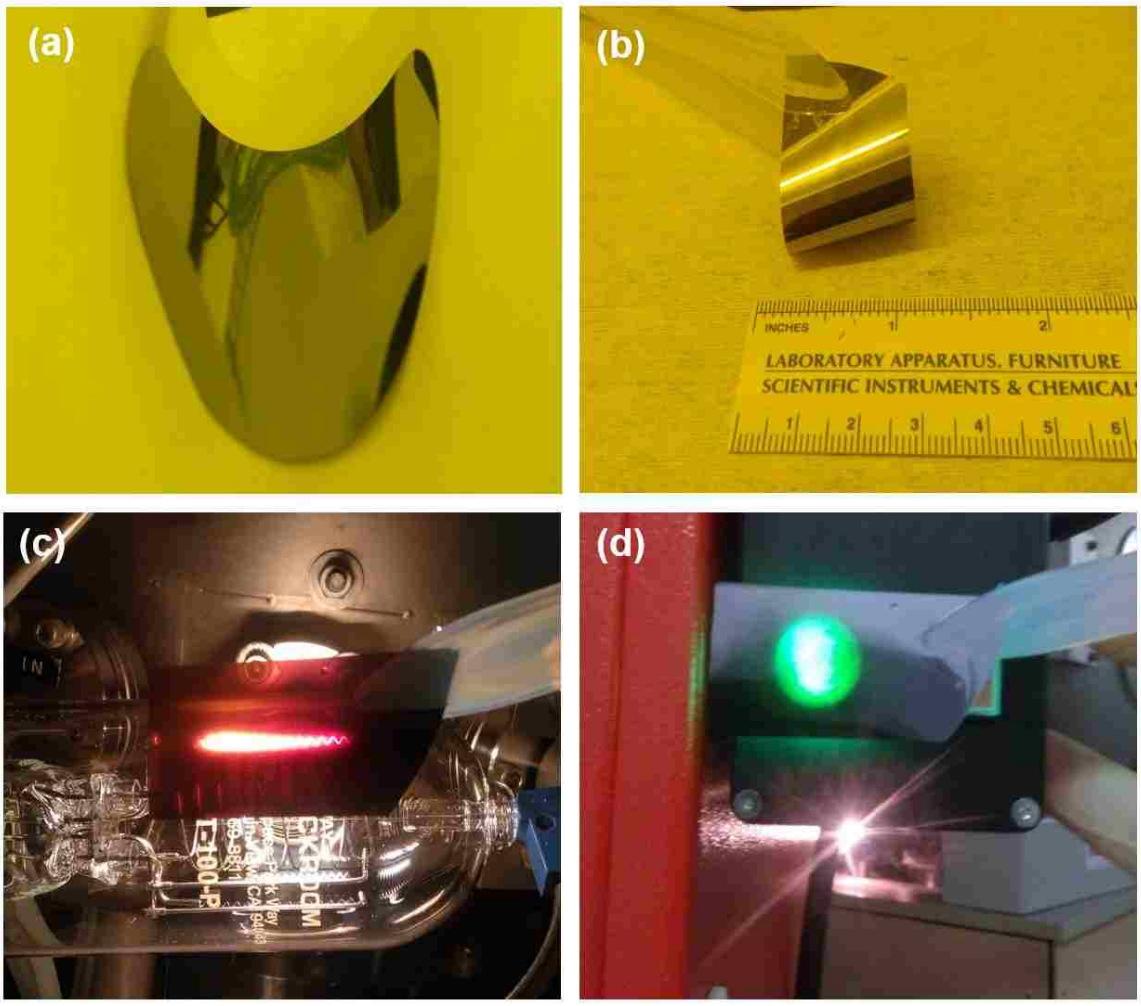

Figure 3.5. (a) A 35- μm-thick 4-inch wafer after the thinning, (b) A 10-μm-thick c-Si wafer, (c) & (d) A 10-μm-thick c-Si film which is transparent to yellow and green light.

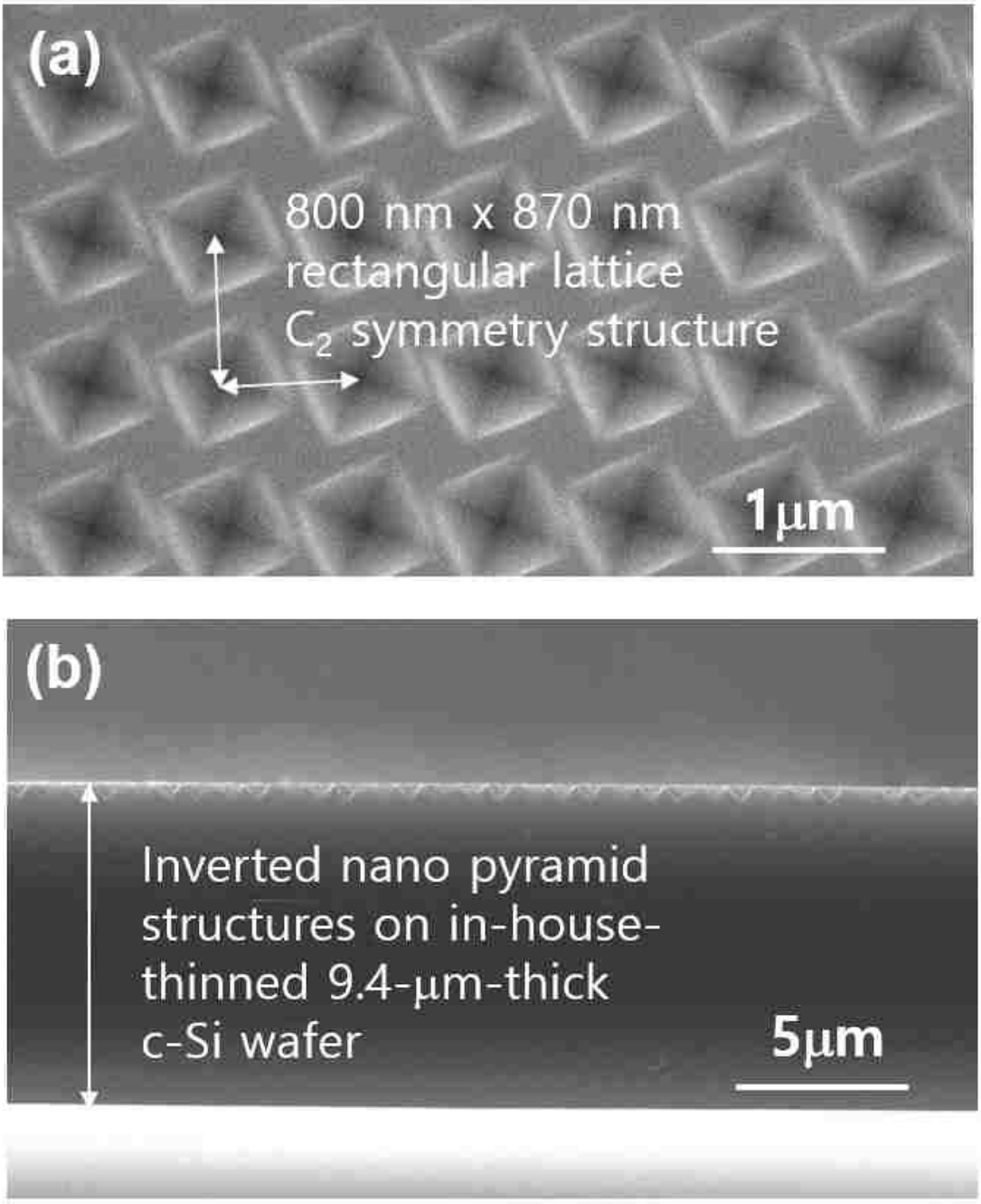

Figure 3.6. An SEM image of a C_2 symmetry inverted nanopyramid array on a thinned 9.4-μm-thick c-Si wafer from (a) a top view and (b) a side view.

3.3. Fabrication of an Inverted Nanopyramids Structure

3.3.1. Fabricating a Potassium Hydroxide Wet Etch Mask

We deposited a silicon nitride (Si_3N_4) layer on a c-Si wafer by plasma enhanced chemical vapor deposition (PECVD) as a mask for potassium hydroxide (KOH) etching. Silane (5% SiH_4/Ar) and ammonia (NH_3) gases were used in this study for chemical reactions to form a Si_3N_4 film at 300 ^oC. As a ratio of silane flow rates to ammonia flow rates increases, the refractive index of deposited SiN_x film increases [77]. We precisely controlled flow rates of feed gases by mass flow controllers. To characterize optical properties of our deposited films, ellipsometry with a Cauchy/c-Si model was used. We optimized the ratio of feed gases for a deposited Si_3N_4 film to have ~1.9 of refractive index and ~zero of extinction coefficient at 633 nm. The thickness of silicon nitride film on our free-standing thinned 14-μm-thick c-Si wafer should be less than 30 nm to prevent the wafer from being bent due to tensile stress developed at the interface of the c-Si substrate and the deposited Si_3N_4 film.

3.3.2. Interference Lithography

We sequentially spin-coated a 160-nm-thick anti-reflection (ARC iCON-16, Brewer Science) layer and a 500-nm-thick negative photoresist (NR7-500P, Futurrex) film on Si_3N_4/c-Si for interference lithography. The temperatures of soft bake for an anti-reflective coating (ARC) layer and a photoresist (PR) film were 180 ^oC and 150 ^oC, respectively. We used Lloyd's mirror interferometry with 355-nm-wavelength-light (YAG-Nd laser, Infinity 40-100, Coherent Inc.) to pattern the prepared substrate (PR/ARC/Si_3N_4/c-Si). Then the substrate was post-baked at 100 ^oC for a minute and

developed in a diluted resistor developer (RD6, Futurrex, Inc.). The scanning electron microscope (SEM) image in Figure 3.7 shows a square lattice of periodic holes in a developed photoresist film in our Lloyd's mirror interferometry system, and the diameter of holes is typically about half of their periodicity. The size of holes can be tuned by changing the recipes of interference lithography and photoresist development.

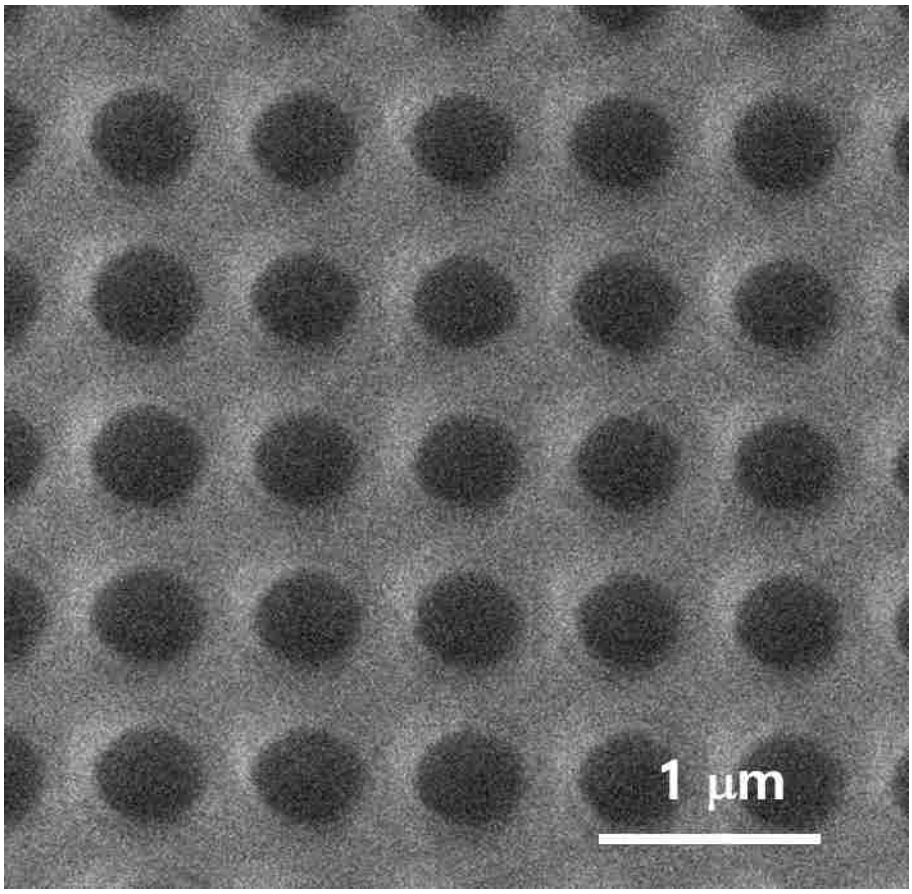

Figure 3.7. An SEM image of circular periodic holes in a photoresist film fabricated by our Lloyd's mirror interferometry system. The diameter of circular openings is usually about half of the periodicity.

3.3.3 Symmetry Control of Inverted Nanopyramid Arrays

The highly anisotropic KOH etching on c-Si(100) wafers leaves etched surface with a fixed angle parallel to c-Si(111) surfaces. An etch rate of c-Si(111) surface is several hundred times slower than other c-Si surfaces, so the c-Si(111) surfaces leave inverted or positive pyramid structures when complete etching of c-Si(100) is performed. Hence, it is difficult to fabricate various shapes of etched structure with different angles of etched surfaces. This reduces degrees of freedom in the fabrication of various shapes of nanopyramids structures. For example, an array of circular opening etch-mask from lithography [Figure 3.7] results in a periodic inverted pyramid structure with c-Si(111) surfaces when complete etching of c-Si(100) is performed. Although we cannot change the shape of each nanostructure, we can fabricate various symmetries of arrays by rotating etch masks about c-Si [001] axis and/or changing lattice types of etch mask. Figure 3.8 illustrates our unique approach to fabricate various symmetries of inverted nanopyramid arrays. In this study, the symmetry groups were denoted by the Schönflies notation. The left column of Figure 3.8 shows various lattice types of etching templates represented by the yellow mask with perforations. We defined the open windows in the etch masks with perforations represented by yellow using lithography and dry etching. The exposed underlying c-Si surface was then etched in KOH solution to create the inverted nanopyramids shown in the right column of Figure 3.8.

The fabrication technique is valid for single crystalline semiconductors, but not for polycrystalline or amorphous materials. However, a metal layer deposited on the inverted nanopyramid arrays can be exfoliated and subsequently used as a bottom contact

to deposit polycrystalline or amorphous materials. Thus, our symmetry breaking method can be extended to non-crystalline films.

In Figure 3.8, we used a square lattice with C_{4v} symmetry as the basis of comparison, where lattice vectors are parallel/perpendicular to the c-Si[110] directions of the c-Si substrate [32]. The first level of symmetry breaking can be achieved by rotating the lattice vector of the etch template with respect to the c-Si[110] direction around the c-Si[001] axis [Figure 3.8 inset]. This lattice rotation effectively results in each inverted nanopyramid rotated around its own apex. Consequently, the mirror symmetry is completely broken while the 4-fold rotational symmetry is preserved. In addition to the rotation, the symmetry can be further broken by arranging the etch windows in non-square-lattice patterns. The possible two-dimensional non-square lattices are rectangular, triangular, centered-rectangular, and oblique lattices [74]. With the previously described sequence of symmetry breaking, we can reduce the symmetry of inverted nanopyramid arrays from C_{4v} to C_2.

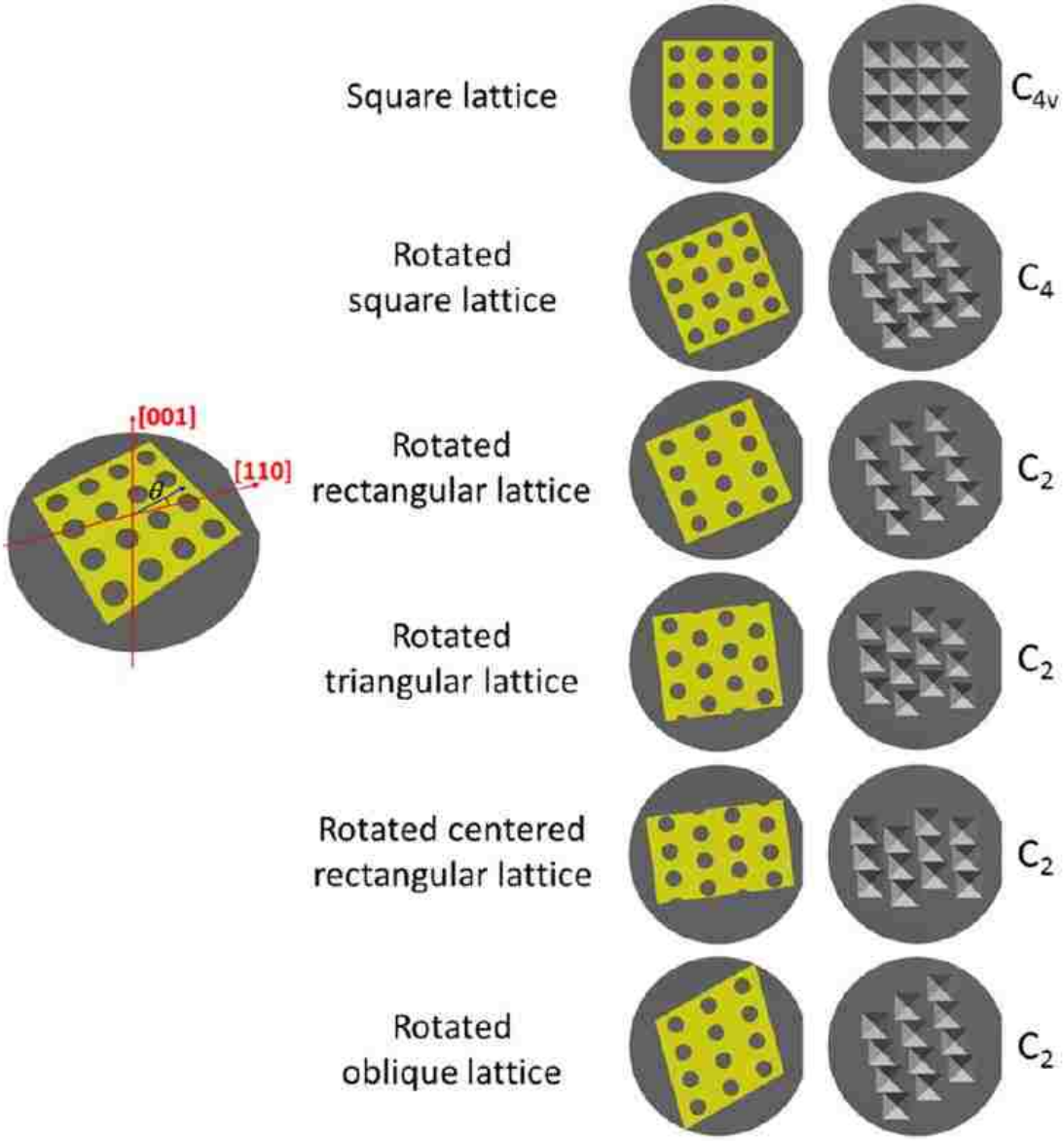

Figure 3.8. A schematic approach to systematically break the symmetry by rotating the etch template (inset) and arranging the openings in various lattice types. Left figures show the etch template rotated about the c-Si[001] axis. The flat region on the right side of each c-Si wafer indicates the c-Si[110] direction. Subsequent etching in an alkaline solution defines inverted nanopyramids on c-Si(100) surfaces (right figures). The resulting symmetries are labeled in Schönflies notation. "Reprinted with permission from ref[78]. Optical Society of America."

3.3.4. Transferring Nano-pattern to Wet Etch Mask

We used reactive ion etching (RIE) for transferring patterns in a photoresist film to underlying anti-reflective coating (ARC) and Si_3N_4 layers. The RIE process consisted of two consecutive steps which use oxygen or CHF_3/O_2 for etching ARC or Si_3N_4, respectively. An ion bombardment through a potential bias between electrodes was highly directional towards the cathode, so the pattern in the photoresist film was effectively transferred to the underlying ARC and Si_3N_4 layers. We used 50-125 W of power at 13.56 MHz radio frequency (RF) to maintain the plasma. A small amount of O_2 was added to the CHF_3 feed gas to boost etch rate of Si_3N_4 and increase sidewall angles [79]. Moreover, the addition of O_2 helped the etch rate to be stable as a function of time avoiding mass transport problems [79, 80]. The process flow of an RIE for transferring pattern in the PR film to the Si_3N_4 layer is described in Figure 3.9.

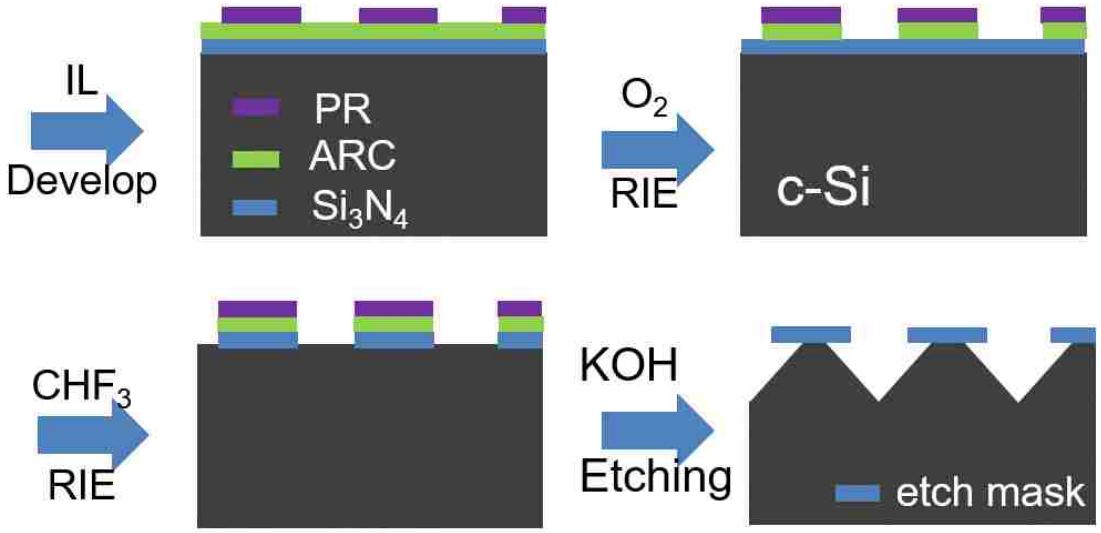

Figure 3.9. A process flow of RIE etching for transferring a pattern in PR to an ARC and an etch mask. Directional bombardments of oxygen or fluorine ions in a potential bias etch underlying films to transfer a pattern.

3.3.5. Potassium Hydroxide Etching

In this research, a potassium hydroxide (KOH) etching of c-Si was used for fabricating a light-trapping structure on thinned c-Si wafers. The KOH etching takes advantage of the intrinsic nature of the KOH wet-etching of c-Si [44-46]. The etch rate of a c-Si(111) surface in KOH solution is hundreds of times slower than that of a c-Si(100) surface. This strong anisotropy naturally left c-Si(111) surfaces when complete KOH wet-etching of c-Si(100) is performed, and these c-Si(111) surfaces formed inverted pyramid structures. In this study, an array of periodic circular openings was used as an etch mask as shown in Figure 3.7, and KOH solution etched the surfaces exposed by mask openings to form an array of periodic inverted-nanopyramids.

We nano-textured the surface at 50 ^{o}C for 10 minutes in 20 wt.% KOH solution. Please noted that temperature and concentration of the KOH solution for nano-texturing

were lower than those in the KOH c-Si wafer thinning (90 ^{o}C and 50 wt.%) [Section 3.2]. In this condition, the KOH etch rate became slow enough to precisely control the size of inverted nanopyramids. We measured the temperature using resistance temperature detectors (RTD). To set the temperature of the KOH solution, output power of the hot-plate was controlled by a PID controller with stirring. The stirring reduced not only the response time of the heating system for an accurate temperature control but also the temperature gradients in the KOH solution for uniform nanostructures. We recorded the temperature data by data acquisition (DAQ, Lab Jack) using an analog output signal of the PID controller. A photograph and a schematic diagram of the KOH etching system are shown in Figure 3.10 (a) and (b).

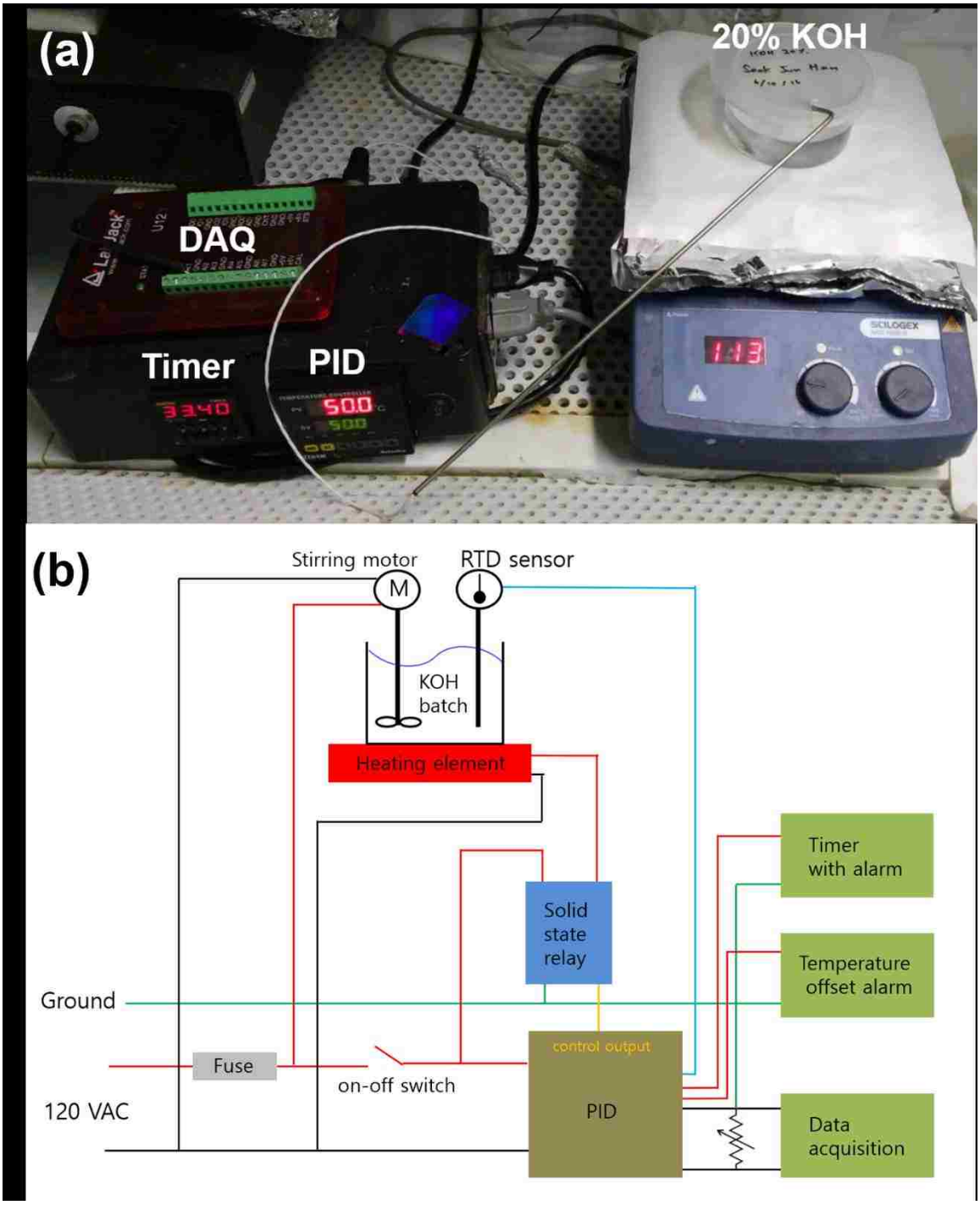

Figure 3.10. A photograph (a) of a schematic diagram (b) and the KOH wet etching system for nano-texturing and thinning of a c-Si wafer. A solid-state relay was used for controlling the heating element. A variance resistor was for calibrating the voltage signals for data acquisition.

3.4. Fabrication of Solar Cells

We adapted a p-type c-Si solar cell fabrication process used in the National Renewable Energy Laboratory (NREL). In this process, a thin (20-100 nm) doped poly-Si layer and an SiO_2 layer(~1 nm) were inserted between a c-Si substrate and a metal contact for excellent passivation [35]. Directly contacting metal on a c-Si substrate without these passivation layers increase the number of surface quantum states due to abrupt change in periodic structure to amorphous structures. The solar cell fabrication process that we adapted based on the NREL process is summarized in Figure 3.11 where the process flow starts from the textured c-Si substrate. In this process flow, the n-type and p-type spin-on-dopants (n-SOD and p-SOD) were used for making a pn-junction on a top surface and an ohmic contact on a bottom surface, respectively, because a diffusion furnace with dopant gas flows and PECVD for doped amorphous silicon were not available in the CHTM. We used bi-directional drive-in to dope both a top crystallized poly-Si layer and a bottom substrate for good ohmic contacts and passivation. Details of the process are described in the Subsections below.

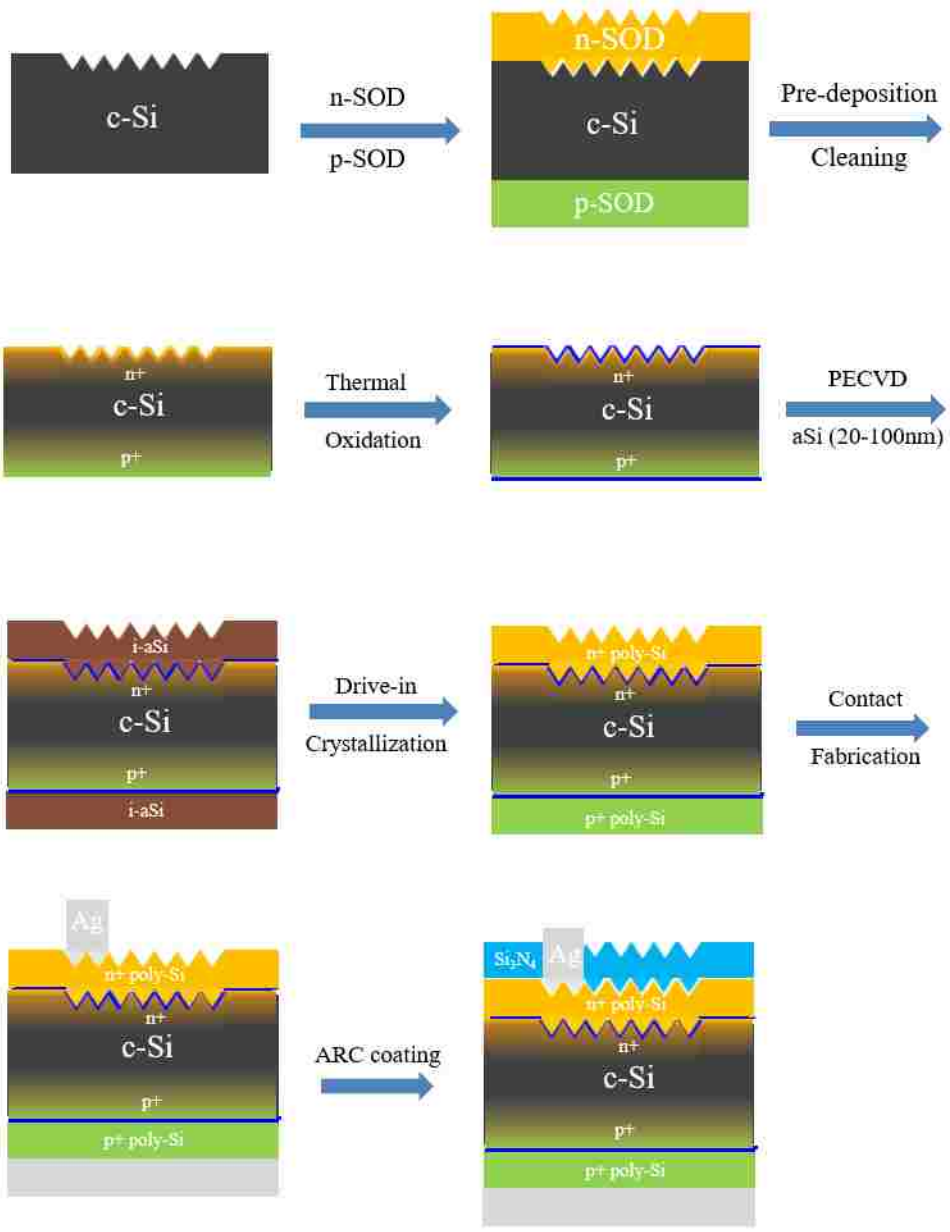

Figure 3.11. A flow diagram of the c-Si solar cell fabrication.

3.4.1. Pre-deposition

In the pre-deposition step, a dopant was diffused into the vicinity of the surface with a contacting source layer by diffusion. We deposited an n-type spin-on-dopant (n-SOD, P-1200, Desert Silicon) layer on top of the inverted nanopyramids structure to form a pn-junction. On the bottom side, a p-type spin-on-dopant (p-SOD, B-200, Desert Silicon) layer was deposited to form a highly boron doped c-Si layer for an ohmic-contact to a metal back reflector. These SOD layers served as source layers during pre-deposition, and the dopant atoms were infiltrated into the vicinity of the surface. We performed the pre-deposition at 960 ^{o}C for 2 hours. After pre-deposition, the surfaces were carefully cleaned because a boron silicide layer on bottom and defects on top could be developed. The boron silicide layer has negative effects on solar cell performance by increasing contact resistances and the number of surface states. Also, a phosphorous atom has a bigger atomic radius than that of boron. Hence, the diffusion of phosphorous can cause damaged surfaces on top. In this study, to remove these boron silicide layer and damaged surfaces, we used the methods of RIE etching, isotropic wet etching, and/or thermal oxidation introduced in Section 3.1. We ramped up the temperature of pre-deposition slowly to minimize the damages from phosphorous diffusion.

Figure 3.12 shows the calculated dopant concentration profile in a cross-section of the c-Si substrate with a grooved surface when the doping was performed by the pre-deposition. The dopant in the calculation was phosphorus (P), and the grooves were triangular in a cross-sectional plane along the dashed red line in Figure 3.12 inset. We used a finite difference method to calculate 2D diffusion profile in triangular grooves. In the simulation, rectangular meshes (5 nm × 7.1 nm) were used with a time step of

0.005 hours. Periodic boundary condition on the side of the unit cell was used. The values of saturation concentration at 960 ^{o}C were adopted for boundary condition from the literature [66].

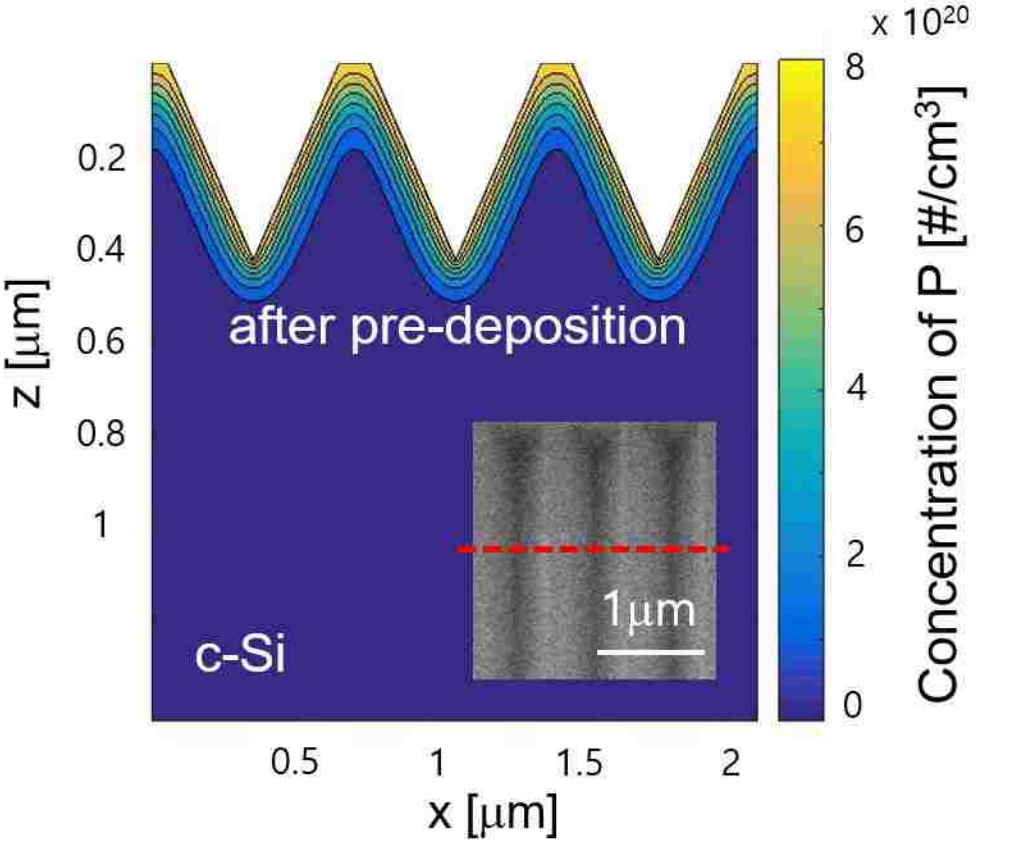

Figure 3.12. Calculated dopant concentration profile in a cross section of c-Si substrate along a dashed red line (in the inset) with periodic triangular grooves. The inset shows an SEM image of triangular grooves in a c-Si substrate after KOH etching.

3.4.2. Surface Passivation

We passivated the top and bottom of pre-deposited surfaces for metal electrodes contact. A proper passivation technique can effectively reduce the number of surface states, which is required for high efficiency solar cells. For the passivation, we made a stack of a tunneling SiO_2 layer and a highly doped polysilicon (poly-Si) layer. The tunneling SiO_2 layer is thermally grown on c-Si substrate for the passivation. And then, an intrinsic amorphous-silicon (i-aSi) layer was deposited by PECVD on SiO_2/c-Si substrate. The bi-directional dopant drive-in was performed to crystallize and dope the i-aSi layer into a highly doped poly-Si layer at 950 ^{o}C for 3 hours. The detailed procedures for the passivation techniques used in this study are described in Subsections below.

3.4.2.1. Thermal Oxidation

A thickness of thermally grown SiO_2 layer is recommended to be less than 2 nm to enable tunneling [81]. The SiO_2 growth rate on different c-Si surfaces is different, and the inverted nanopyramid structure is mostly composed of c-Si(111) surfaces. Hence the c-Si(111) wafers are used in this study. The Deal-Grove model mathematically describes a growth of an oxide layer on a silicon surface [82]. However, a tunneling oxide layer grows much faster than the Deal-Grove model so we investigated the thicknesses of thermally grown SiO_2 layers on c-Si(111) by ellipsometry (M-2000, J. A. Woollam). Ellipsometry is a non-contact and non-destructive optical technique that determines the optical properties (refractive index and attenuation coefficient) and thickness of films. We used a white light source which covers a wavelength range from

270 nm to 1700 nm at various incidence angles from 45^{o} to 85^{o}. The c-Si(111) wafer was pre-treated to remove a native oxide layer, and then a SiO_2 layer was grown at 700 ^{o}C for the duration from 3 minutes to 12 minutes. Figure 3.13 shows the thickness of SiO_2 layers measured by an ellipsometer with the model of Cauchy/effective medium (1 nm)/c-Si. The oxidation time and thickness of SiO_2 layers are summarized in Table 3.2. The silicon atoms at the interface of a thermal SiO_2 layer and a c-Si substrate are naturally inter-connected by covalent bonds, which minimizes abrupt change in structure and the number of dangling bonds at the interface. However, due to the distance mismatch between Si-Si interatomic distance (2.35 Å) in c-Si and the Si-Si second neighbor distance (3.05 Å) in SiO_2, there are remaining Si dangling bonds at the interface. We terminated these dangling bonds by hydrogen using forming gas annealing for 10 minutes at 400 ^{o}C.

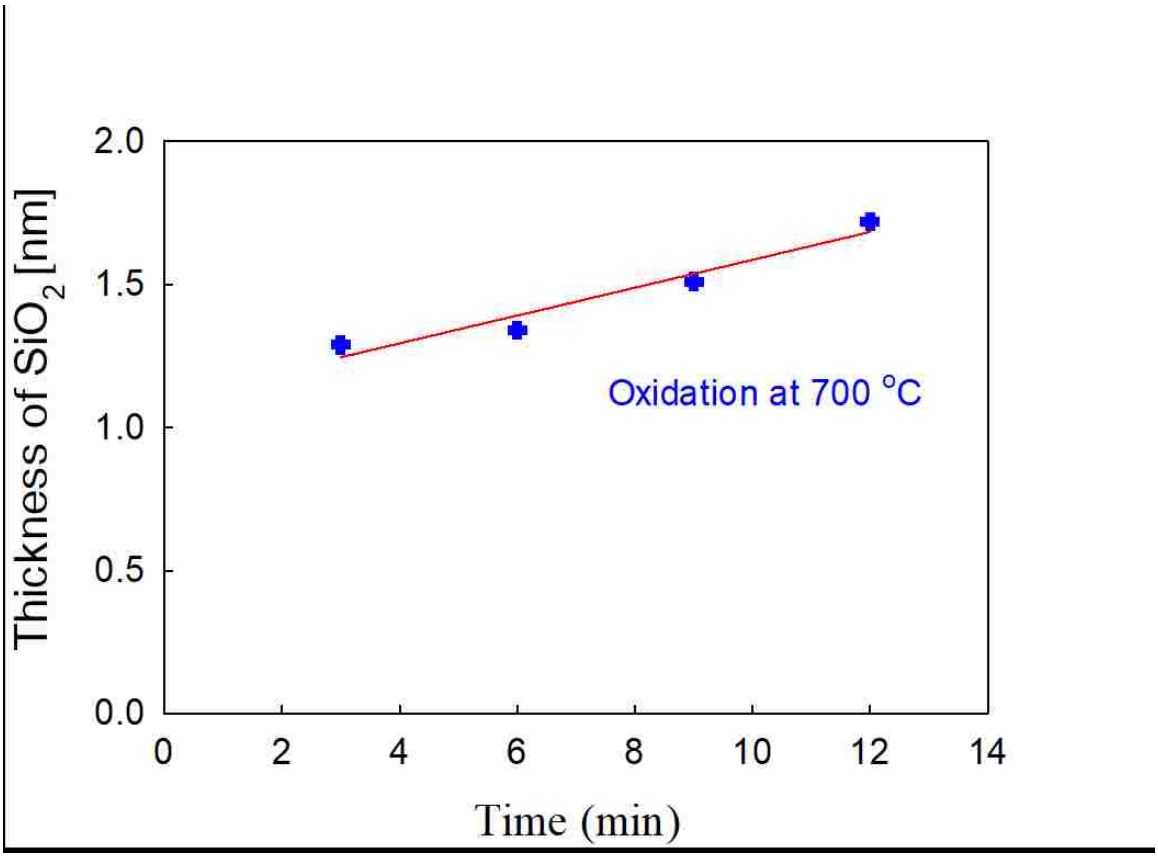

Figure 3.13. Thickness of thermally grown SiO_2 layers on c-Si(111) as a function of oxidation time at 700 ^{o}C.

Table 3.2 Thickness of thermally grown SiO_2 layers at 700 ^{o}C on a c-Si(111) substrate

Oxidation time	Thickness of SiO_2
3 minutes	1.29 nm
6 minutes	1.34 nm
9 minutes	1.51 nm
12 minutes	1.72 nm

3.4.2.2. Plasma Enhanced Chemical Vapor Deposition for Amorphous Silicon

In our passivation approach, a good uniformity of 20-100 nm thick intrinsic amorphous Si (i-aSi) layer was required for high efficiency of solar cells. The 20-100 nm thick i-aSi layer is too thin to analyze with an SEM. Hence, we deposited thick (4 μm or 8 μm) i-aSi layers by PECVD to accurately measure the rate of i-aSi deposition and the number density of plasma dust particles. The formation of plasma dust particles is due to a homogeneous gas phase nucleation which grows negatively charged silicon particles trapped electrostatically in the plasma. The sizes of dust particles increase until the gravitational and electrostatic forces are unbalanced [83, 84]. These plasma dust particles on a deposited film reduce solar cell efficiency on our inverted nanopyramid structure. In this study, we varied a pressure of silane gas, which contains 95% Ar, and RF power to optimize the quality of an i-aSi film. The experimental conditions and results are summarized in Table 3.3. Figure 3.14 (a) shows SEM (left) and optical (right) images of an 8-μm-thick i-aSi layer deposited by PECVD at the pressure of 850 mTorr silane/Ar. Operated RF (13.56 MHz) power was 100 W, and the measured deposition rate was ~40 nm/minute. As shown in Figure 3.14 (a), many plasma dust particles were on the deposited i-aSi film, and their diameters were about 3 μm. We deposited another 8-μm-thick i-aSi film at reduced RF power of 50 W while maintaining the pressure of SiH_4/Ar as 850 mTorr. A deposition rate was unchanged at ~40 nm/minute, but the diameters and the number density of plasma dust particles were significantly reduced. However, large plasma particles were observable in an optical microscope image as shown in Figure 3.14 (b). In our experiment, the best quality of an i-aSi film was achieved when the pressure was 450 mTorr silane/Ar and RF power was

50 W. In this case, the deposition rate was reduced by a factor of two as the pressure was decreased from 850 mTorr to 450 mTorr, and Figure 3.14 (c) shows a deposited 4-μm-thick i-aSi film. The diameter of the plasma dust particles was about 300 nm, so they were indistinguishable in an optical image. Therefore, if we make a solar cell with this film, optical scattering by plasma particles can be minimized because both the diameter and the number density of plasma dust particles are small enough. All the experiments were done at 300 ^{o}C, and the general trends of our experiments agreed well with the Perrin's research [83, 84].

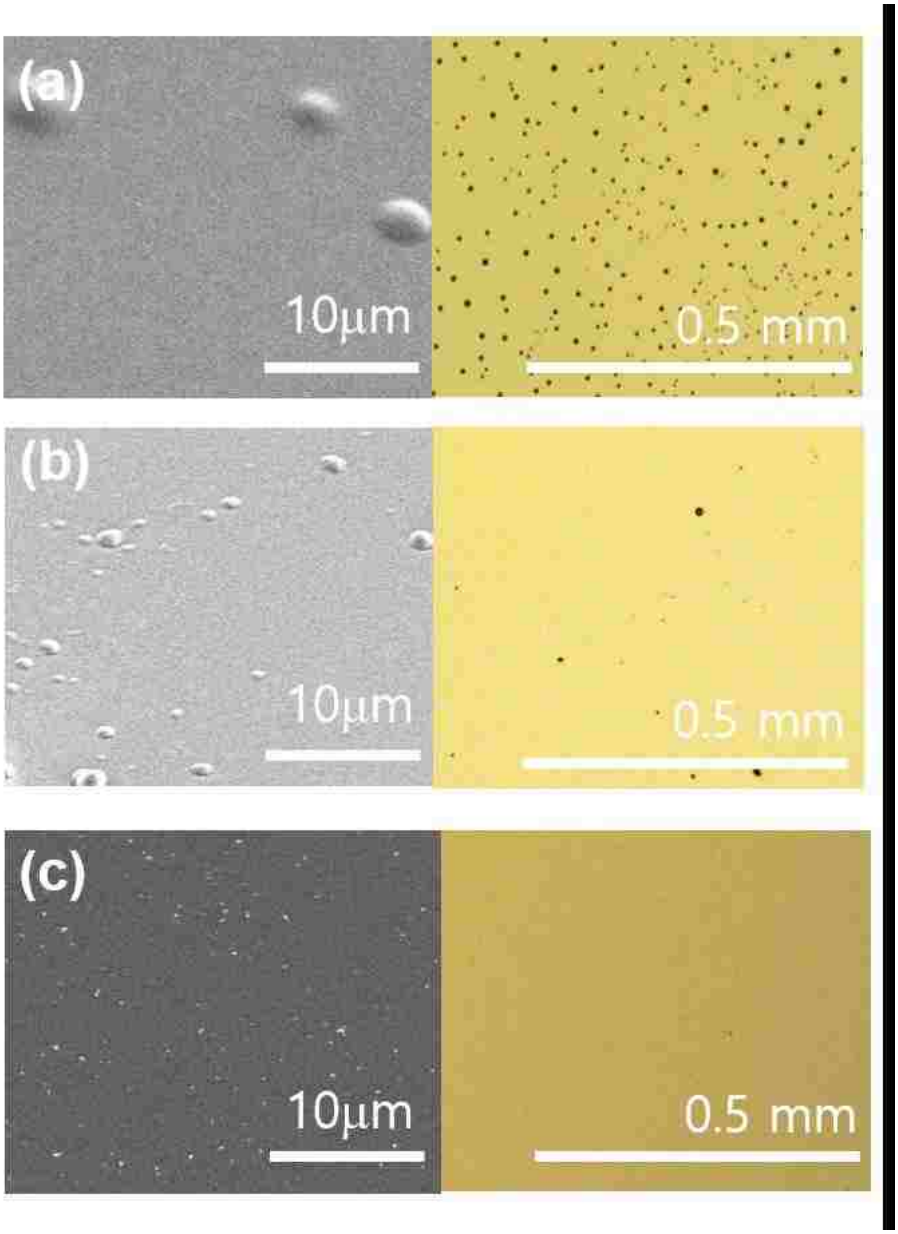

Figure 3.14. SEM (left column) and optical (right column) images of PECVDed i-aSi layers under the condition of (a) 850 mTorr silane, 300 ^{o}C, 100 W, (b) 850 mTorr silane, 300 ^{o}C 50 W, and (c) 450 mTorr silane, 300 ^{o}C, 50 W.

Table 3.3 Effect of pressure and RF power on i-aSi PECVD at 300 ^{o}C

Pressure of 5% SiH_4/Ar	RF Power	Deposition time	Thickness	Deposition Rate	Diameter of a Plasma Dust Particle	Number Density of Particles (> 1 μm)
850 mTorr	100 W	20 minutes	8 μm	40 nm / minute	~ 3 μm	~72.3/μm/mm^2
850 mTorr	50 W	20 minutes	8 μm	40 nm / minute	~1.5 μm	~4.9/μm/mm^2
450 mTorr	50 W	20 minutes	4 μm	20 nm / minute	~0.3 μm	~0.6/μm/mm^2

3.4.2.3. Bi-directional Drive-in and Crystallization

We diffused dopant atoms into the vicinity of the surface with a contacting source layer by the pre-deposition described in Section 3.4.1. The impurities near the surface was diffused deep into the substrate through a drive-in process. We performed drive-in bi-directionally to diffuse dopant atoms into both an underlying c-Si substrate and a top thin poly-Si layer at 950 ^{o}C for 3 hours. During the bi-directional drive-in, the dopant atoms diffused deep into the c-Si substrate to form Gaussian dopant concentration profile, and the thin poly-Si layer was highly doped to make an interfacial layer for an ohmic contact with metal electrodes. A gradual and smooth change of dopant concentration in c-Si substrate reduces the recombination of charge carriers by decreasing the number of surface states. We covered the substrate with a 100-nm-thick SiO_2 layer to protect the substrate from contaminations during the bi-directional drive-in. The protective SiO_2

layer was deposited by PEVCD at 300 ^{o}C. To calculate the concentration profile, the dopant concentration in Figure 3.12 was used as an initial condition. The calculated dopant concentration profile after drive-in with periodic triangular grooves is shown in Figure 3.15. The targeted pn-junction depth was about 500 nm for our solar cells. Our calculations showed that dopant concentration along a textured surface can vary by a factor of two because the periodicity of structure (700 nm) is comparable to the desired thickness of pn-junction (500 nm). This inhomogeneity in concentration has negative effects on solar cell efficiency and will be studied in Section 4.2.

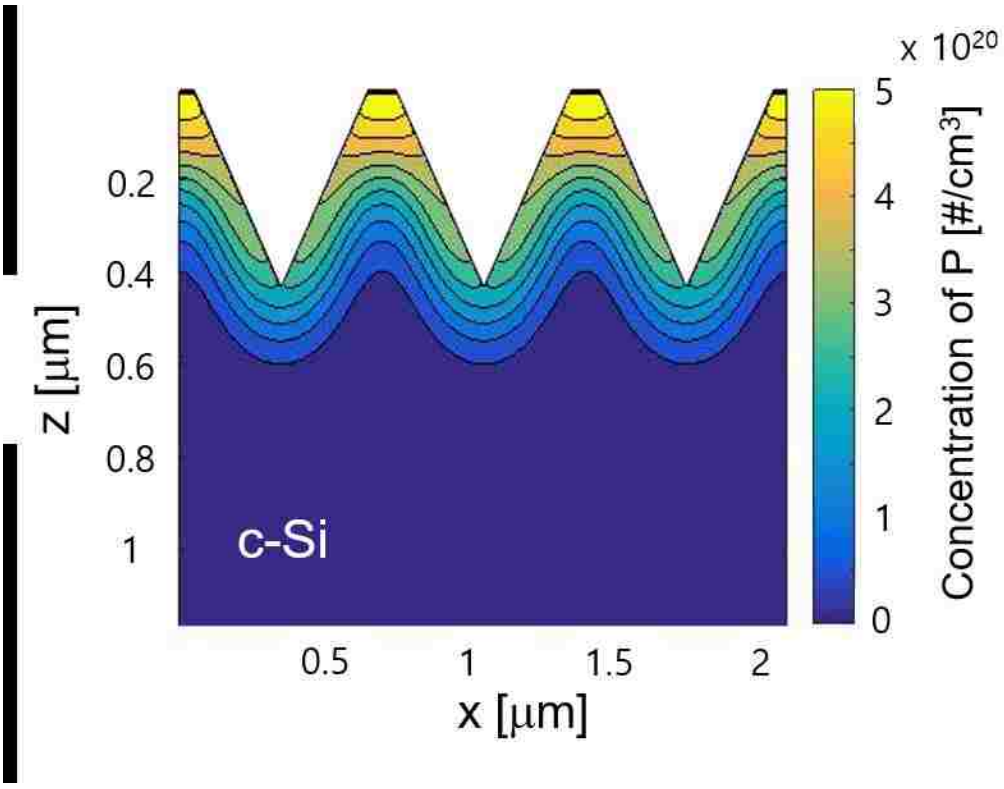

Figure 3.15. Calculated dopant concentration profile after drive-in in a c-Si substrate with periodic triangular grooves. The concentration profile roughly represents that in a cross section of an inverted nanopyramid array (top view in the inset) marked by a red-dashed line.

A 50-nm-thick of i-aSi layer on top of the structure is crystallized to poly-Si while temperature is ramped up for drive-in. The temperature was slowly ramped up from 200 ^{o}C to 950 ^{o}C at the rate of 83 ^{o}C/hour. The required temperature for crystallization was above 800 ^{o}C. The pre-deposited dopant atoms also diffused into a poly-Si layer during the bi-directional drive-in, hence the layer became a highly doped poly-Si layer to reduce a width of Schottky barrier width for ohmic contacts through tunneling. The crystallized doped poly-Si layer on a c-Si substrate provides a gradual transition from c-Si to metal [35].

A quality of crystallized poly-Si layer depends on the initial state of an i-aSi layer. For example, hydrogen in an i-aSi layer releases hydrogen gases (H_2) from $(Si\text{-}H)_n$ complexes in voids during crystallization, and thermal expansion of H_2 in voids forms blisters [85]. Figure 3.16 (a) and (b) show optical images of 100-nm-thick poly-Si layers crystallized from i-aSi layers deposited at (a) 450 mTorr and (b) 250 mTorr at 50 W by PECVD. Even though both i-aSi films were highly uniform, they become very different in uniformity after crystallization.

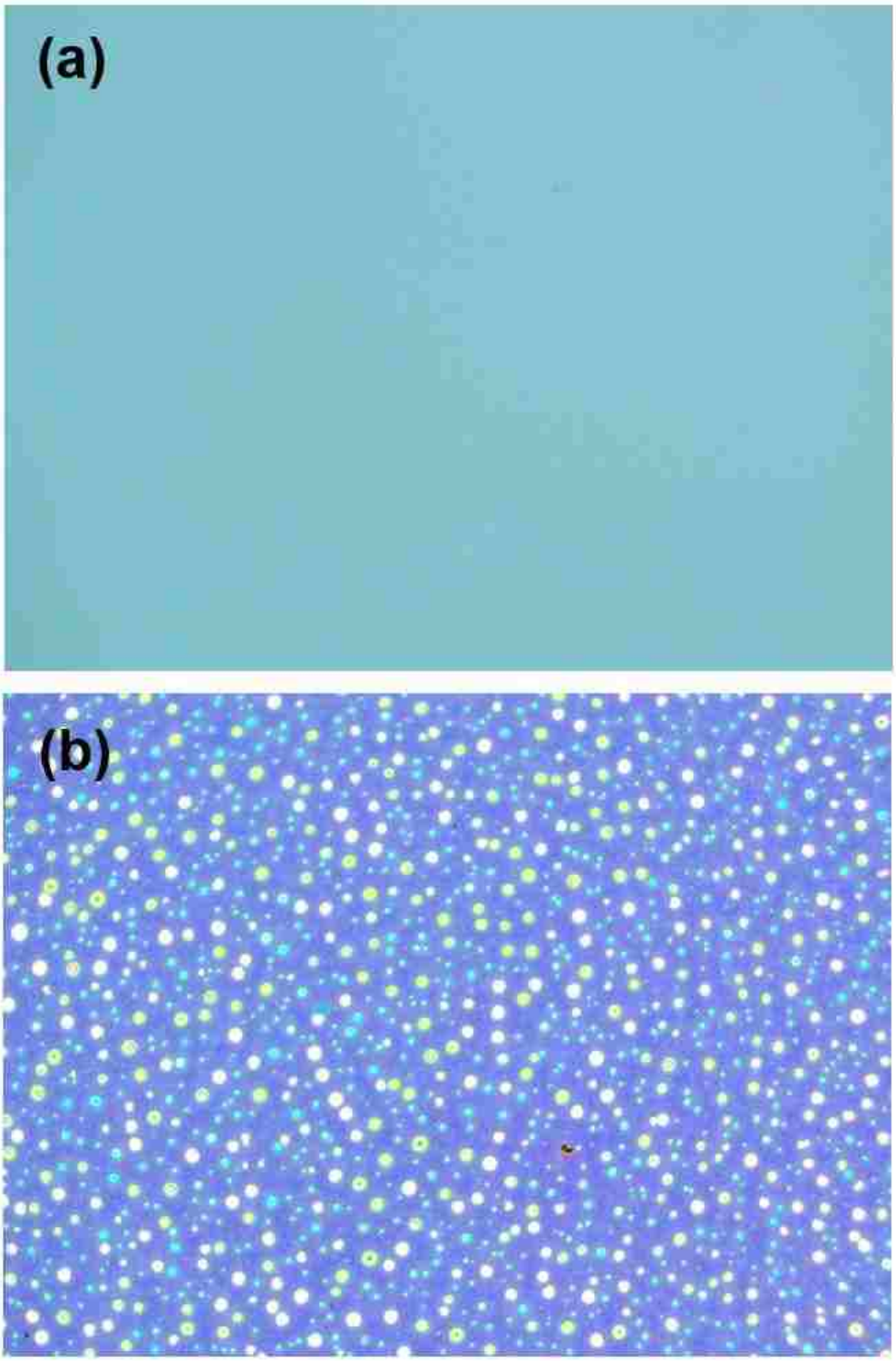

Figure 3.16. Magnified optical images of crystallized 100-nm-thick polysilicon films from (a) a PECVDed i-aSi layer at 450 mTorr with 50 W RF power and (b) a PEVCDed i-aSi layer at 250 mTorr with 50 W RF power.

3.4.3. Metal Contact Fabrication

We deposited a top metal contact grid by an e-beam evaporator. To selectively deposit metal on a region of top contact grid, a mask with grid opening scribed by a laser cutter was used. We prepared the mask made of pure c-Si to avoid contamination of solar cells because the mask was contacting a solar cell during the metal deposition. Figure 3.17 (a) shows a magnified optical image of the fabricated c-Si mask at a region near the contact pad indicated as a dashed red square in Figure 3.17 (b).

We characterized the dimension of top metal contact grid by an optical microscope. Measured width of each finger was 70 μm, and the 35 fingers on each side of the busbar were equally spaced by 700 μm. Because the spacing between fingers determines average distance that needs to be traveled by a charge carrier in a semiconductor, it is closely related to a power loss from sheet resistance. Measured width and length of the busbar were 270 μm and 25 mm, respectively. We deposited a stack of 20-nm-thick Ti/1500-nm-thick Ag/20-nm-thick Pd layers for the top metal contact grid. The thin (20 nm) Ti layer was deposited before depositing the Ag layer to improve adhesion between contact grid and c-Si substrate. A thickness and a width of Ag were related to a power loss of solar cells in series resistance. Due to high conductivity of Ag, a 1500-nm-thick-Ag layer was enough to achieve the fill factor of 75 %. A capping thin (20 nm) Pd layer helped to protect an Ag metal grid from oxidation. Figure 3.17 (b) shows an optical image of the deposited top metal grid on a flat c-Si solar cell.

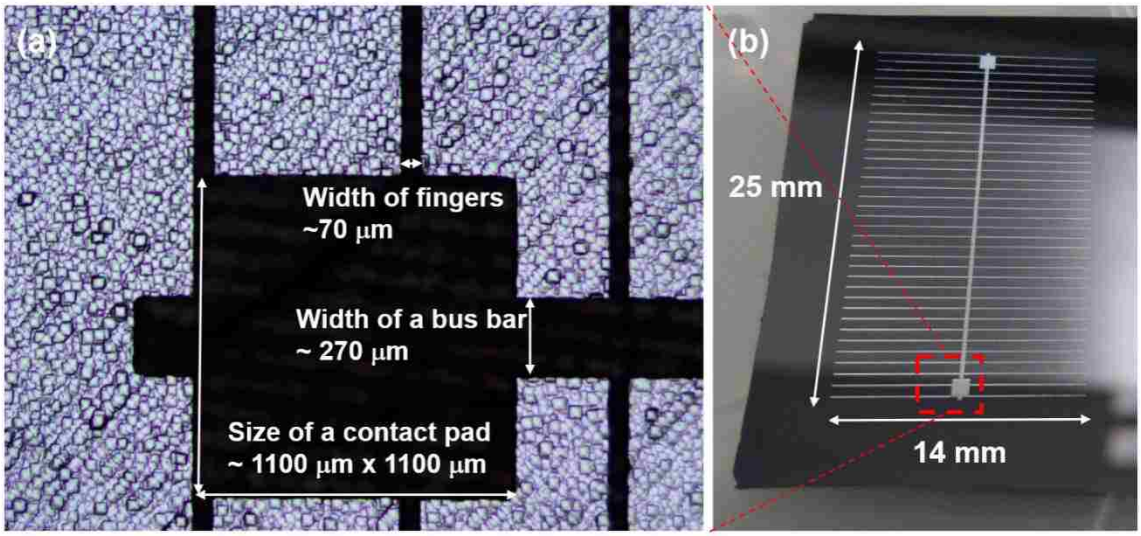

Figure 3.17. (a): A magnified optical image of the c-Si mask made by laser cutting. The black region is an opening for a contacting grid. The c-Si mask has pyramids on its surface because the mask is post-treated by KOH etching to fabricate sharp edges of the opening. The dashed red square in (b) indicates the magnified region of the mask to obtain an image of (a). (b): A photograph of the deposited top metal contact grid on a flat-c-Si solar cell.

3.4.4. Anti-reflective Coating

We deposited a quarter-wavelength anti-reflective coating layer on top of the structure to minimize reflection losses in solar cells. The refractive index of c-Si at 633 nm of wavelength is about 3.88, hence the optimum refractive index of the anti-reflective coating layer for a c-Si solar cell in the air is a square root of the c-Si's refractive index (n=1.97). An optical response of a solar cell is sensitive to the refractive index of an anti-reflective layer, so we characterized the deposited SiN_x films by ellipsometry. In this experiment, the white light source of ellipsometry covered a range of wavelength from 270 nm to 1700 nm at various incidence angles from 45^o to 85^o. We deposited an anti-reflective SiN_x layer by PECVD at 300 ^oC with 50 W RF power. The feed gases

were a gas of 5% SiH_4 contains 95% Ar and a pure gas of NH_3,and they were precisely controlled by mass flow controllers. The ellipsometry results of deposited SiN_x films were compared with two models, a Cauchy/c-Si model and a Palik's Si_3N_4/c-Si model. The deposited SiN_x films were fitted into the Cauchy/c-Si model to find out the refractive index of deposited SiN_x films. If the deposited SiN_x film had zero extinction coefficients over the entire wavelength range of source light, the deposited SiN_x film would be fitted into a Cauchy layer which is essentially a transparent dielectric layer. However, the SiN_x and reference Si_3N_4 layers have non-zero but small extinction coefficients at a short wavelength range of our source light, hence the good quality SiN_x film would be slightly off from the Cauchy model. This is why we used the second model, Palik Si_3N_4/c-Si, to compare with the optical constants of reference Si_3N_4. A good quality of deposited SiN_x film will show good fits with both of the two models. We used mean square errors (MSE) to quantify the goodness of fit with the models. Basically, the MSE is root of mean square errors between measured data and model generated data. We obtained MSE using Eq. (2) as below

$$\mathrm{MSE} = \sqrt{\frac{1}{3n-m}\sum_{i=1}^{n}\left[\left(\frac{N_{Ei}-N_{Gi}}{0.001}\right)^2+\left(\frac{C_{Ei}-C_{Gi}}{0.001}\right)^2+\left(\frac{S_{Ei}-S_{Gi}}{0.001}\right)^2\right]} \qquad (2)$$

where n is the number of measured wavelengths, m is the number of fit parameters, subscription E represents experimented data, subscription G represents generated data by model, N=cos(2 × Psi), C=sin(2 × Psi) × cos(Delta), and S= sin(2 × Psi) × sin(Delta). The three parameters are non-zero components of Mueller-matrix for the case of isotropic sample. The Mueller-matrix mathematically describes how an electromagnetic wave interacts with the sample. The details for analysis of ellipsometry results with the

Mueller-matrix formalism are introduced in Ref[86, 87]. In general, the lower the MSE values are, the better agreements between data from an actual SiN_x film and generated data from the model are expected. The experimental condition of PECVD and elipsometry results are summarized in Table 3.4. As we changed the volumetric flow ratio of SiH_4/Ar to NH_3 from 1.0 to 4.0, the refractive index of the Cauchy layer increased from 1.76 to 1.9. The deposited SiN_x films with the flow ratio of SiH_4/Ar to NH_3 from 1.0 to 3.0 were represented as a Cauchy layer but significantly different from the reference Palik Si_3N_4 layer (MSE > 50) due to their low refractive indices. When the volumetric flow ratio of SiH_4/Ar to NH_3 was higher than 5.0, the film was neither a Cauchy layer nor a Palik Si_3N_4 layer due to its high extinction coefficients. We obtained the best SiN_x film when the flow ratio of SiH_4/Ar to NH_3 was 4.0. The film deposited in this condition could be considered as both the Cauchy layer and the Palik Si_3N_4 layer. Figure 3.18 compares the ellipsometry results of a deposited SiN_x film (solid lines, using volumetric ratio of 4.0) with the reference model of Palik Si_3N_4/c-Si (doted lines). The optical response of the deposited SiN_x layer agreed well with the reference model; hence the deposited film was close to the reference Palik Si_3N_4 film.

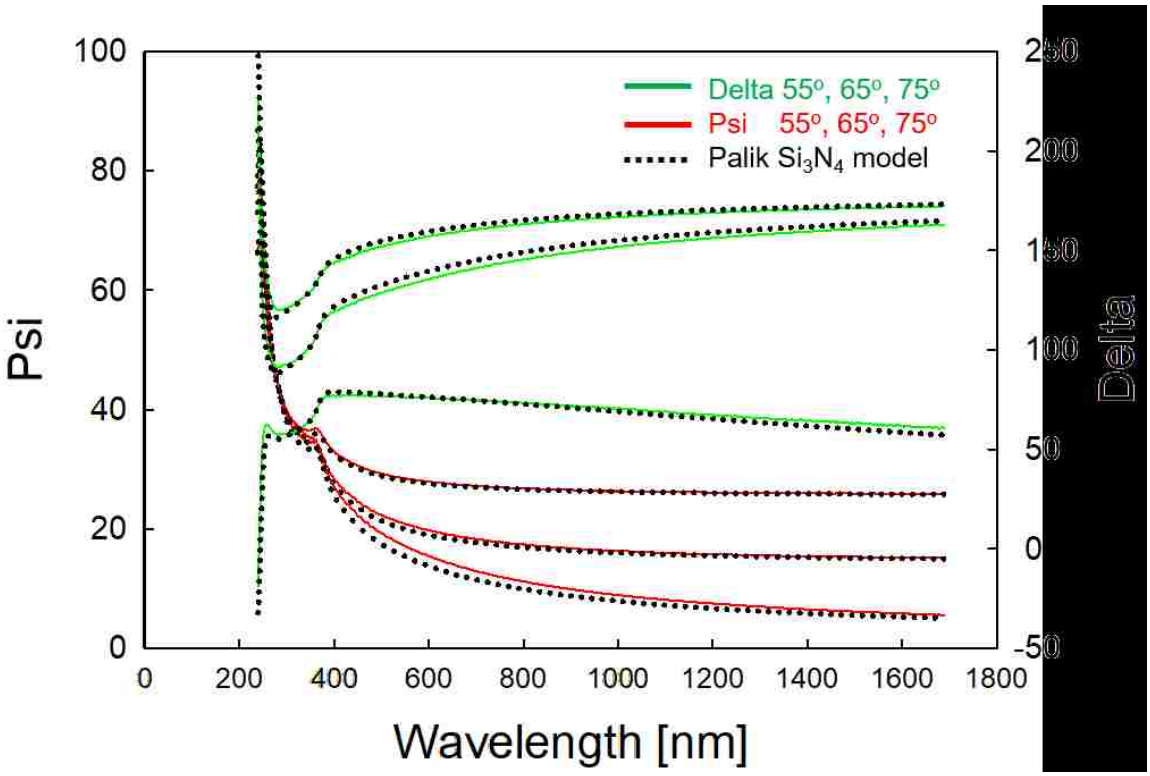

Figure 3.18. Comparison of ellipsometry results (Psi and Delta) at various incidence angles (55, 65 and 75°) between deposited SiN_x film by PECVD and the reference model of Palik's Si_3N_4 film.

Table 3.4 Summary of ellipsometry results on SiN_x PECVD

The volumetric flow ratio of 5% SiH_4/Ar to NH_3	Deposition pressure [mTorr]	n of Cauchy layer at 633 nm	MSE of Cauchy on c-Si	MSE of Palik Si_3N_4 on c-Si	Remarks
1.0	600	1.76	4.72	96.99 (out of spec.)	Cauchy layer
2.0	600	1.77	4.45	94.36 (out of spec.)	Cauchy layer
3.0	800	1.81	3.42	52.67 (out of spec.)	Cauchy layer
4.0	1000	1.9	8.28	26.01	Cauchy layer & Palik Si_3N_4
5.0	1200	1.9	111.09 (out of spec.)	157.54 (out of spec.)	None

4. RESULTS AND DISCUSSION

4.1. Light Trapping of Various Symmetries of Inverted Nanopyramid Arrays

A square lattice of the C_{4v} symmetry structure has two lattice vectors which are parallel and perpendicular to the c-Si[110] directions [32]. The first level of symmetry breaking can be achieved by rotating the lattice vectors of the etch template with respect to the c-Si[110] direction around the c-Si[001] axis. This lattice rotation effectively results in each inverted nanopyramid rotated around its own apex. Consequently, the mirror symmetry is completely broken while the 4-fold rotational symmetry is preserved. In addition to the rotation, the symmetry can be further broken by arranging the etch windows in non-square-lattice patterns. The possible two-dimensional non-square lattices are rectangular, triangular, centered-rectangular, and oblique lattices [88]. With the previously described sequence of symmetry breaking in Section 3.3.3, we can reduce the symmetry of inverted nanopyramid arrays from C_{4v} to C_2.

The symmetry-breaking inverted nanopyramids can be directly fabricated on kerfless thin c-Si films or KOH thinned c-Si films. The c-Si films of a few μm to tens of μm in thickness are produced using a kerfless process and commercially available today. In this Section, solely for the convenience of handling samples, we used silicon-on-insulator (SOI) wafers to obtain the light-trapping structures on thin c-Si films. The SOI wafers consisted of a 10-μm-thick device layer, a 500-nm-thick buried SiO_2 layer, and a thick handle layer. The etch masks were fabricated on the device layer of SOI wafers using interference lithography (IL) and reactive ion etching (RIE) [Figure 4.1(a) left]. The SOI wafers with the etch masks were etched in a KOH solution to define the inverted nanopyramids into the underlying c-Si, and the etch masks were subsequently

removed [Figure 4.1(a) middle]. Since the anisotropic etching step leaves flat unetched areas between the inverted pyramids, which reduces light trapping [32], we used a HNO_3/HF aqueous solution to further etch the c-Si isotropically [89]. Then, a 73-nm-thick silicon nitride (SiN_x) layer was deposited on the nanopyramids for antireflection using plasma-enhanced chemical vapor deposition (PECVD). The refractive index of the SiN_x layer was determined by ellipsometry to be 1.7 – 1.9 at the wavelength of 632.8 nm. A depression window was then created in the handle wafer using etching in a KOH solution over an area defined by lithography. To protect the front SiN_x layer and nanopyramids during the depression window etching, we spin-coated a polymer (Protek B3, Brewer Science) on the front surface before etching. The buried SiO_2 layer in the SOI wafer served as the etch stop. After etching the depression window, the polymer protective film was removed, and a 100-nm-thick Ag film was deposited on the exposed surface of the SiO_2 layer as a backside reflector [Figure. 4.1(a) right]. In our current effort, we defined the thin-film structures over a 2.5 cm × 1 cm area in SOI wafers. Similar procedures for preparing a thin c-Si film using SOI wafers can be found in References [5, 32].

Figure 2(b)-(d) show SEM images of inverted nanopyramid arrays with C_{4v}, C_4, and C_2 symmetry fabricated on SOI wafers before the SiN_x layer was deposited. The pitch in the square lattice was 700 nm for C_{4v} and C_4 symmetry. For C_2 symmetry, we used a rectangular lattice where the pitches along the lattice vectors were 800 and 900 nm, respectively. The C_4 and the C_2 structures were obtained by rotating the square and rectangular template lattices according to our scheme in Figure 3.8 (2nd and 3rd rows) in Section 3.3.4. The rotation angle was approximately 22.5^o. This angle was chosen to

be half of 45° to reduce the symmetry from C_{4v} to C_4; 45° rotation would result in the same C_{4v} symmetry. The isotropic etching time was kept for 10 minutes to minimize the unetched area while maintaining the shape definition of inverted nanopyramids. Prolonged isotropic etching tends to blur the shape of nanopyramids and makes it difficult to be compared with modeling results. Figure 4.1 illustrates this uniformity over 10 μm range, and multiple scans over ~1 cm range at sampled regions show similar uniformity. Overall, we have established a systematic approach to break the symmetry in an inverted nanopyramid array on a c-Si(001) surface, using scalable lithography and simple wet etching steps.

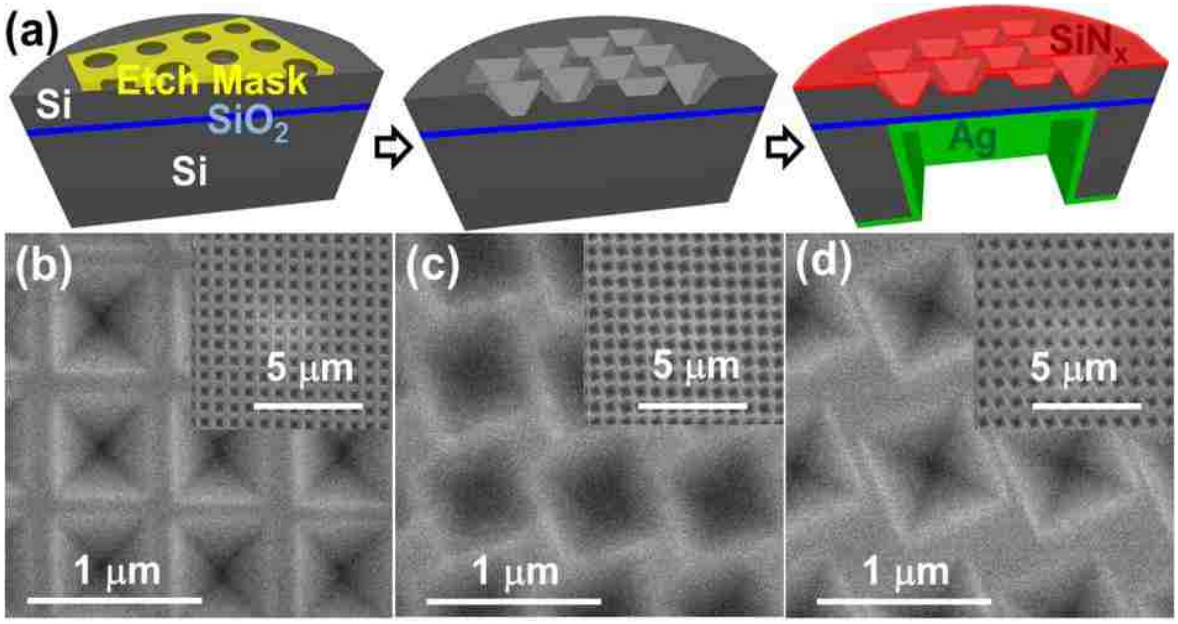

Figure 4.1. (a) An illustration of the fabrication process for light-trapping structures on thin c-Si films. (b)-(d) Scanning electron micrographs of the inverted nanopyramid arrays with (b) C_{4v}, (c) C_4, and (d) C_2 symmetry. The insets are a de-magnified view of each structure. These structures were obtained after 8-min anisotropic etching at 55℃ followed by 10-min isotropic etching at 25℃. In (c) and (d), each pyramid was rotated by approximately 22.5° around its own apex from a lattice vector. The periodicity in the two orthogonal directions was 700 nm × 700 nm for (b)-(c) and 800 nm × 900 nm for (d). "Reprinted with permission from ref[78]. Optical Society of America."

The pitches of the three structures correspond to the maximum absorption for ~2-μm-thick c-Si films based on optical calculations. To find the optimum pitches, we performed optical calculations based on the transfer matrix method [90]. To save computation time in searching through many parameter values, we considered the nanostructures etched into a 2-μm-thick or 2.33-μm-thick c-Si film. For the C_4 and C_2 symmetry inverted nanopyramid arrays, the angle between one of the lattice vectors and the c-Si[110] direction was set to 22.5°. We assumed the inverted nanopyramid arrays have no unetched horizontal areas by complete isotropic etching after KOH etching. The structures were conformally coated with a 60-nm-thick SiN_x layer with a refractive index of 1.9 for anti-reflection. On the backside of the c-Si film, a 717-nm-thick SiO_2 film and a 150-nm-thick Ag layer were placed as a reflector. Figure 4.2 (a) shows the periodicity dependence of the calculated photovoltaic efficiency for the C_{4v} and C_4 symmetry inverted nanopyramid arrays on 2.33-μm-thick and 2-μm-thick c-Si films, respectively. In both cases, the optimized periodicity was found at 700 nm. Figure 4.2 (b) displays the efficiency map of the C_2 symmetry (C_4 symmetry on the diagonal) structures for various combinations of periodicities from 500 to 1000 nm in the x and y directions which correspond to the lattice vectors. This map reveals that the maximum efficiency occurs when the periodicities are 800 and 900 nm in the x and y directions, respectively. Thus, for the maximum light trapping with inverted nanopyramids, the symmetry should be broken from C_4 to C_2 but not by a great degree of change in periodicity from that of C_4. The optimum periodicities found in the calculations are employed in our experiment as shown in Figure 4.1 (b)-(d). The calculated efficiencies at the optimum periodicities for C_{4v} (2.33 μm thickness), C_4 (2 μm thickness), and C_2 (2

μm thickness) symmetry inverted nanopyramids were 0.228, 0.237, and 0.251, respectively.

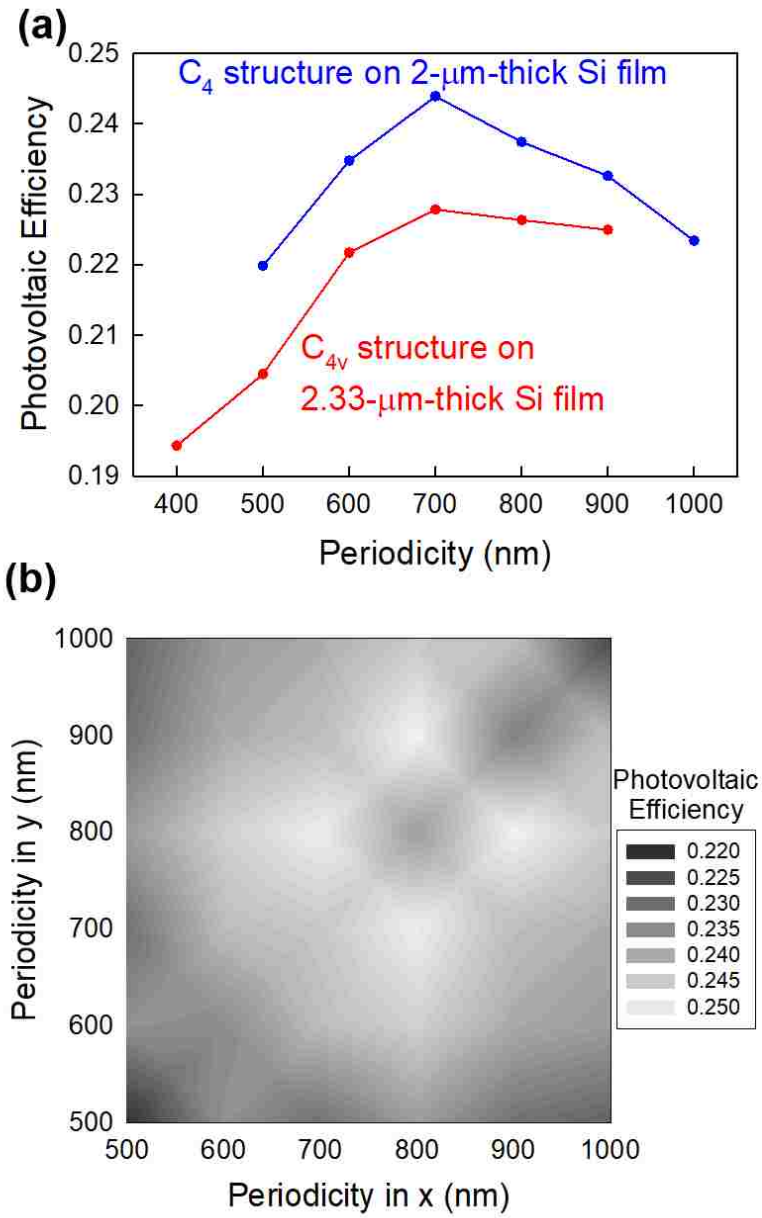

Figure 4.2. (a) Calculated photovoltaic efficiency based on absorption in a 2.33-μm-thick and 2-μm-thick c-Si film for the C_{4v} and C_4 symmetry light-trapping structures, respectively, as a function of the periodicity. (b) Calculated efficiency for the C_2 symmetry structures based on a rotated rectangular lattice with various periodicities in x and y directions where the angle between x-axis and c-Si[110] direction is 22.5°. "Reprinted with permission from ref[78]. Optical Society of America."

Light absorption by the periodic structures is strongly governed by the number of resonance peaks and the coupling strength of the resonances to external radiation [50, 91]. In general, the number of peaks can be increased by breaking the symmetry, while the coupling strength is not trivial to be controlled or estimated. Group theory predicts that, at normal incidence, the number of peaks, N, within a spectrum should be $N(C_{4v}) = N(C_4) < N(C_2)$ when N is large [50]. Using the transfer matrix method [90], we calculated the absorption spectrum from 0.99 to 1 μm for our 3 samples in Figure 4.1 (b)-(d) and count N. The large-scale difference between the etch depth of ~0.5 μm and the film thickness of 10 μm poses a significant challenge in numerical calculations. To efficiently overcome the challenge, we used a layer-doubling technique in the transfer matrix method. In this technique, a transfer matrix for a thick Si layer was easily obtained by doubling the matrix for a thin layer multiple times. The calculated absorption spectrum is shown in Figure 4.3. For accurate counting of the number of peaks, we used high spectral resolution at small intervals of 5×10^{-5} eV and took the second derivative of the spectrum. Peak positions were identified as the points where the second derivative was negative and local minimum. In an agreement with group theory, N increased from 23 for the C_{4v} and C_4 structures to 34 for the C_2 structure. For C_{4v} and C_4 symmetries, the optical response was the same for two orthogonal linear polarizations, resulting in degeneracy in the peaks. For C_2 symmetry, the 4-fold rotation symmetry was broken, and the degeneracy was lifted resulting in resonance peak splitting and increased absorption. While the spectral range of investigation was very narrow, the results were a proof-of-concept demonstration of how the number of resonance peaks depends on the symmetry. Therefore, it is expected that the light absorption will

increase as the symmetry is reduced from C_{4v} (or C_4) to C_2. Moreover, the light absorption can increase despite the same number of resonance peaks (e.g., C_4 vs. C_{4v}) [50], if light coupling can be strengthened. As a result, the light absorption progressively increases as the symmetry is reduced from C_{4v} to C_4 to C_2.

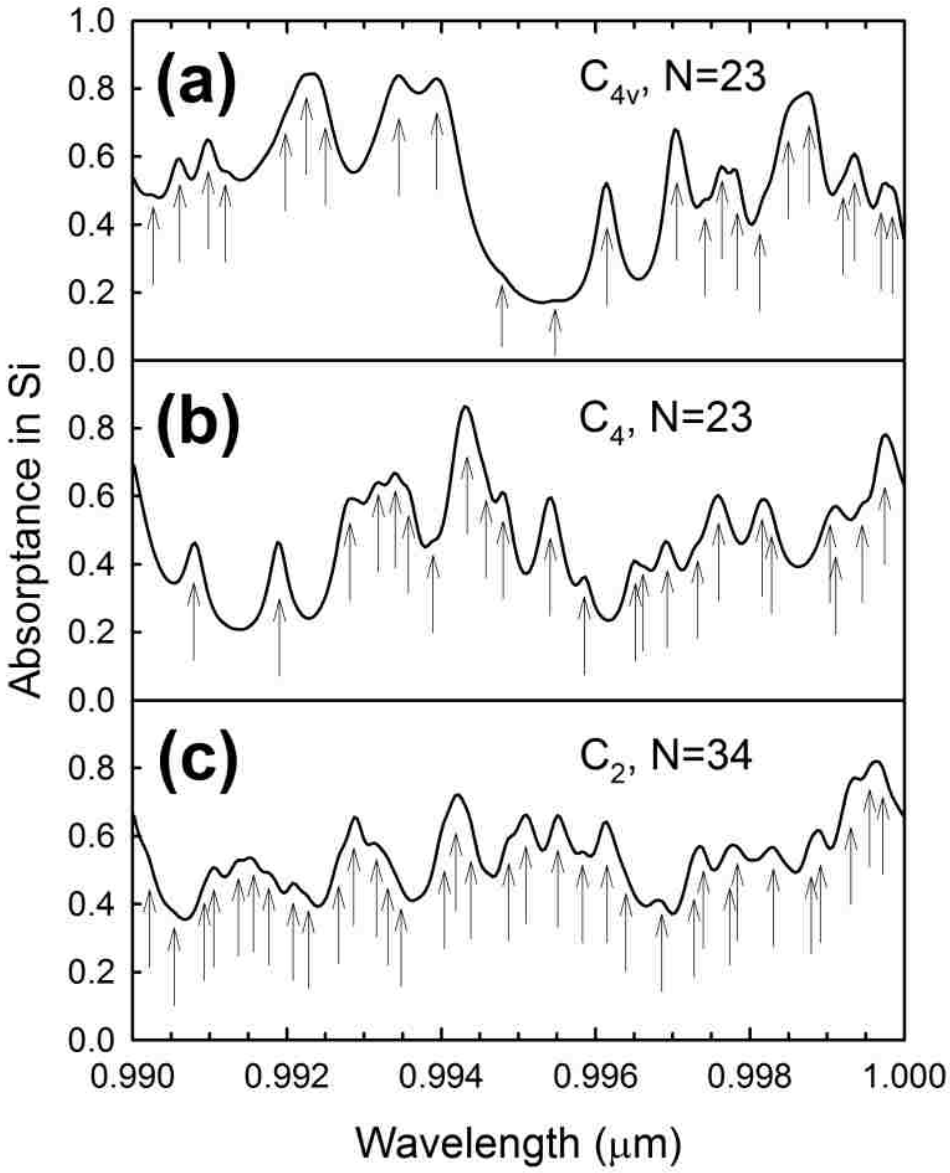

Figure 4.3. Calculated spectra of absorption in a 10-μm-thick c-Si film for the C_{4v}, C_4, and C_2 symmetry light-trapping structures shown in Figure 4.1(b)-(d). Arrows indicate peak positions found from the second derivatives of the spectra. "Reprinted with permission from ref[78]. Optical Society of America."

The optical absorption spectra of the C_{4v}, C_4, and C_2 symmetry samples have been measured using a spectrophotometer with an integrating sphere (Lambda 950, Perkin-Elmer). The angle of incidence was 8° from the surface normal. Figure 4.4 (a)-(c) show the measured and calculated spectra of total absorption for the samples of C_{4v}, C_4, and C_2 symmetry, respectively. In general, good agreement between the measured and calculated absorption is observed. Calculated absorption in Ag is also displayed in Figure 4.4 (a)-(c). The metal loss is appreciable only for wavelengths greater than 900 nm.

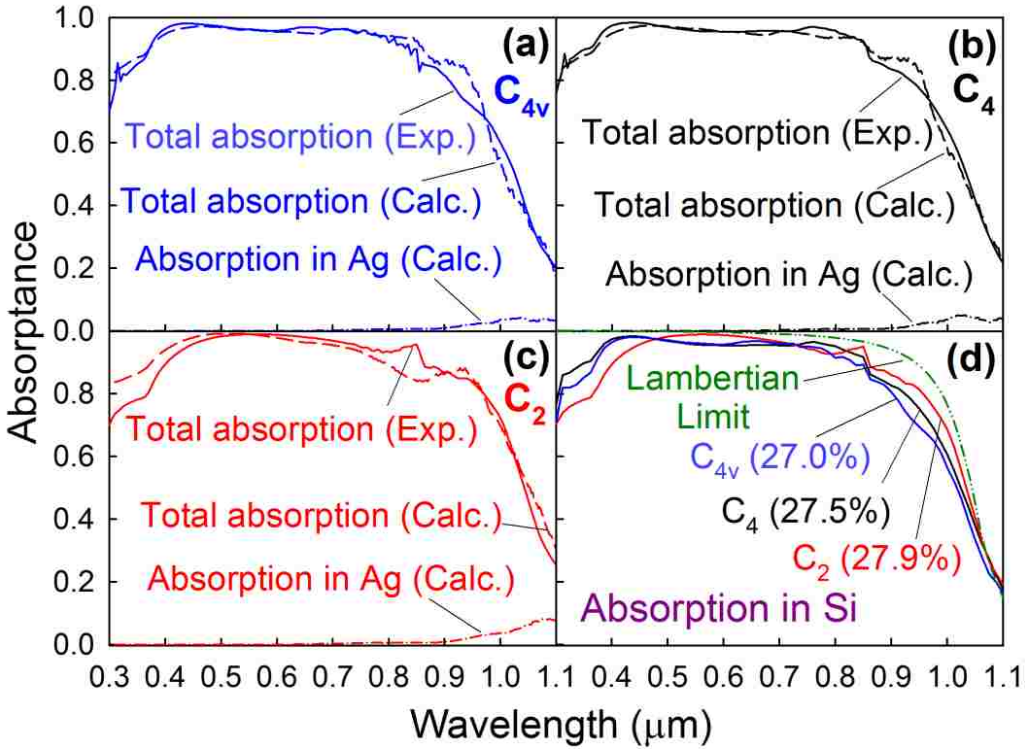

Figure 4.4. (a)-(c) Comparison of experimental (solid line) and calculated (dashed line) total absorptance and calculated absorption in Ag (dot-dashed) for the inverted nanopyramid arrays of (a) C_{4v}, (b) C_4 and (c) C_2 symmetry shown in Figure 4.1(b)-(d). For the calculated absorption, the spectra were averaged over a photon energy range of 0.06 eV to smoothen sharp peaks. The refractive index of the SiN_x coating was 1.7 for (a), (b) and 1.9 for (c) in the calculations. (d) Absorptance in c-Si for the inverted nanopyramid arrays of C_{4v} (blue), C_4 (black), and C_2 (red) symmetry. The calculated photovoltaic efficiency for each nanopyramids structure is introduced in the parenthesis. "Reprinted with permission from ref[78]. Optical Society of America."

The absorption in c-Si is determined by subtracting the calculated absorption in Ag from experimentally measured total absorptance and displayed in Figure 4.4(d). Absorption in the SiN_x coating is negligible while it exhibits slight absorption below 0.4 μm in wavelength. When the refractive index of SiN_x films is relatively low (< 1.9) as found in the films, the solar-weighted average absorption in the films is estimated to be less than 0.1% even over a corrugated surface [92]. Figure 4.4(d) shows that the systematic symmetry breaking along the $C_{4v} \rightarrow C_4 \rightarrow C_2$ sequence increases the absorption in c-Si in the long wavelengths, approaching closely to the Lambertian light-trapping limit [10]. For photovoltaic applications, light trapping in the long wavelengths is important because the charge thermalization loss is minimal in these wavelengths. To estimate the effect of symmetry breaking on the photovoltaic efficiency enhancement, we calculated the photovoltaic efficiency using the spectra in Figure 4.4(d). The efficiency calculation assumed that the charge carrier loss is only due to radiative recombination and the solar cell is at room temperature. With this assumption, the current density J is given by

$$J(V) = \int_0^{\lambda_g} \frac{\lambda}{hc} A_{Si}(\lambda) I(\lambda) d\lambda + \frac{2\pi E_g^{\ 2} k_B T}{h^3 c^2} e^{-\frac{E_g}{k_B T}} \left(1 - e^{\frac{eV}{k_B T}}\right), \qquad (1)$$

where V, λ, h, c, A_{Si}, I, e, E_g, λ_g, k_B, and T denote voltage, wavelength, Planck's constant, light speed, absorption in c-Si, AM1.5G solar spectrum electronic charge, c-Si band gap, wavelength corresponding to the band gap, Boltzmann's constant, and solar cell temperature, respectively. The efficiency is the maximum of J product V divided by incident power. When absorption is perfect, this efficiency leads to the Shockley-Queisser limit [93]. Note that Eq. (1) is different from Eq. (16) in Ref. [94]. This is because the substrate is a metal in our case while Ref. [94] assumes an absorbing

semiconductor substrate. The efficiencies for the C_{4v}, C_4, and C_2 symmetry samples were calculated to be 27.0%, 27.5%, and 27.9%, respectively. That is, the efficiency increases by the systematic symmetry breaking in the inverted nanopyramid arrays. The absolute increase of 0.9% in the efficiency by symmetry breaking could further increase when the corrugation structure is optimized and when the active layer thickness increases. For example, we consider the structures where the unetched flat areas between nanopyramids are completely removed by isotropic etching. In this case, the efficiencies for C_{4v}, C_4, and C_2 symmetry inverted nanopyramids on a 20-μm-thick silicon layer are estimated to be 28.1%, 29.1%, and 30.0%, respectively. This indicates that, if wet etching steps are further optimized, and the active layer thickness is doubled, our symmetry breaking method would increase the efficiency by 1.9%, a significant number for Si photovoltaics. Considering 15.7% device efficiency experimentally demonstrated by Han and his collaborators [5] from C_{4v} symmetry surface corrugation on 10-μm-thick substrates, we can extrapolate the device efficiency for our structures. For example, because the calculated efficiencies are 27.0% and 30.0% for a 10-μm-thick Si film with the C_{4v} symmetry structure and a 20-μm-thick Si film with the C_2 symmetry structure, one could potentially achieve $15.7\% \times 30.0 / 27.0 = 17.4\%$ efficiency for 20-μm-thick solar cells with C_2 symmetry structures when flat areas between nanopyramids are minimal.

4.2. Dopant Diffusion Through Selective Regions

In our experiments, a series of conventional pre-deposition (Section 3.4.1) and drive-in (Section 3.4.2.3) results in inhomogeneity of dopant concentration profile due to the geometric effect of nanostructures on diffusion. The concentration at the top is twice more than that at the bottom of the triangular grooves as shown in Figure 3.15. When doping is performed long enough to avoid underdoped regions, the top region would be overdoped resulting in a reduction in minority carrier lifetime. Oppositely, when an overall doping level is low to avoid overdoped regions, the bottom regions would be underdoped, and the series resistance of solar cells would increase. Thus, in both cases, solar cell efficiency decreases in general due to the doping inhomogeneity. To resolve this inhomogeneity problem in the concentration of dopant, a new method for dopant diffusion has been introduced.

A conventional process for diode fabrication removes an etch mask after texturing, and subsequently, a pn-junction is created. This can cause inhomogeneity of dopant concentration due to the geometry of texture as explained above. We used the etch mask as a barrier of dopant diffusion in the pre-deposition process to reduce inhomogeneity of dopant concentration. Figure 4.5 illustrates our process flow for a dopant diffusion through selective regions of the surface by an etch mask. In this process flow, etching was performed to define an inverted nanopyramid array when a perforated etch mask was placed on a c-Si substrate. A spin-on-dopant (SOD) layer was spin-coated on the structure which includes the etch mask. During pre-deposition, the dopant atoms were infiltrated selectively through the c-Si surface regions that directly

contact the SOD layer. The etch mask and the SOD layer were subsequently removed, and the dopant drive-in was performed to obtain Gaussian concentration profile.

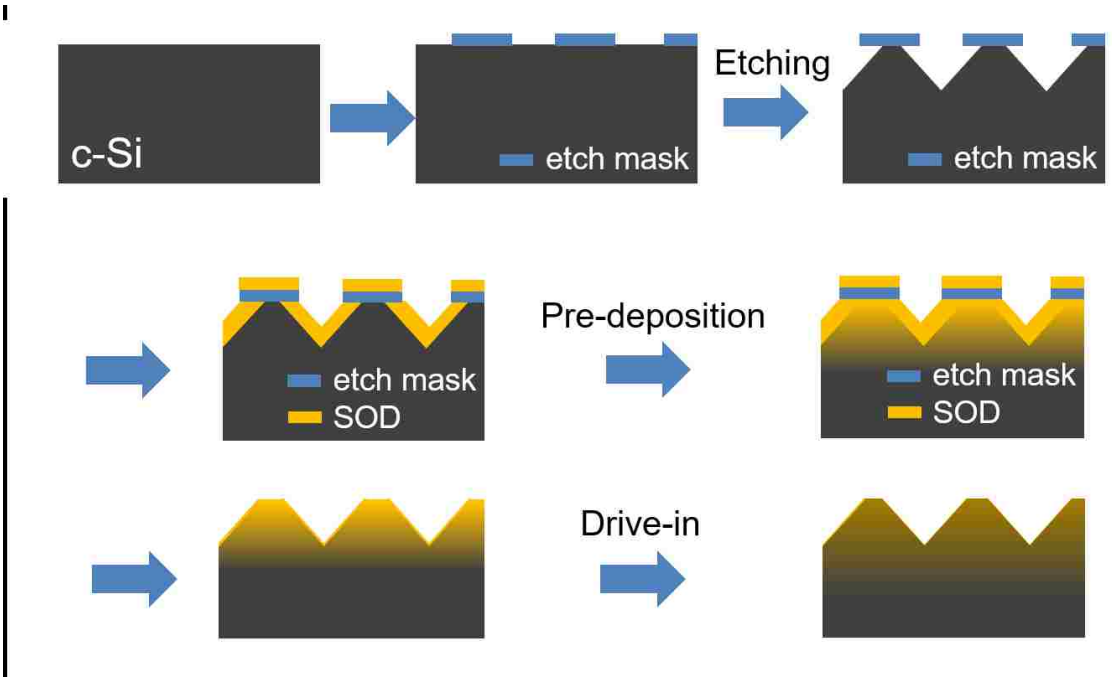

Figure 4.5. A process flow for pn-junction fabrication by dopant diffusion through selective regions of the surface into micro/nanotextured c-Si substrate.

We estimated the effect of dopant diffusion through the selective regions of the surface on concentration profile by a computer simulation. As a rough approximation, we calculated the concentration profile of phosphorous in a 2D triangular groove structure using a finite difference method. Figure 4.6 shows concentration profiles before pre-deposition [Figure 4.6 top], after pre-deposition [Figure 4.6 middle], and after drive-in [Figure 4.6 bottom] for the both cases of diffusion through selective regions of the surface [left column of Figure 4.6] and conventional diffusion [right column of Figure 4.6]. When the dopant diffusion through selective regions of the surface was performed, the KOH etch mask was intentionally unremoved from a top of the groove structure, so

the c-Si substrate was covered by the etch mask for the dopant diffusion through selective regions. The dopant concentration near the top region covered by the etch mask was significantly reduced, whereas that near the bottom of the grooves was negligibly altered. The inhomogeneity of dopant concentration was mitigated considerably using the dopant diffusion through selective regions.

When the dopant concentration is below 3.7×10^{20} cm^{-3} at the diffusion temperature of 950 ℃ and the thickness of the doped region is on the order of 500 nm, the solar cell would function well [66]. In the calculations, after drive-in, the thickness of doped region at the bottom was ~270 nm, and the concentration at the top region with conventional diffusion was above 3.7×10^{20} cm^{-3}. These results indicate that the underdoped bottom region may lead to relatively high sheet resistance, and the overdoped top region would result in strong charge recombination. In this work, the effect of dopant diffusion through selective regions of the surface on the concentration in the top region is focused. Figure 4.7 displays excess dopant concentration above 3.7×10^{20} cm^{-3} which represents the concentration of electrically inactive dopant in c-Si. By the dopant diffusion through selective regions, the excess concentration was reduced by a factor of two under the same diffusion conditions. Thus, our new method would increase open circuit voltage (V_{oc}), fill factor (FF), and photovoltaic efficiency of the cells by reducing the concentration of inactive dopant.

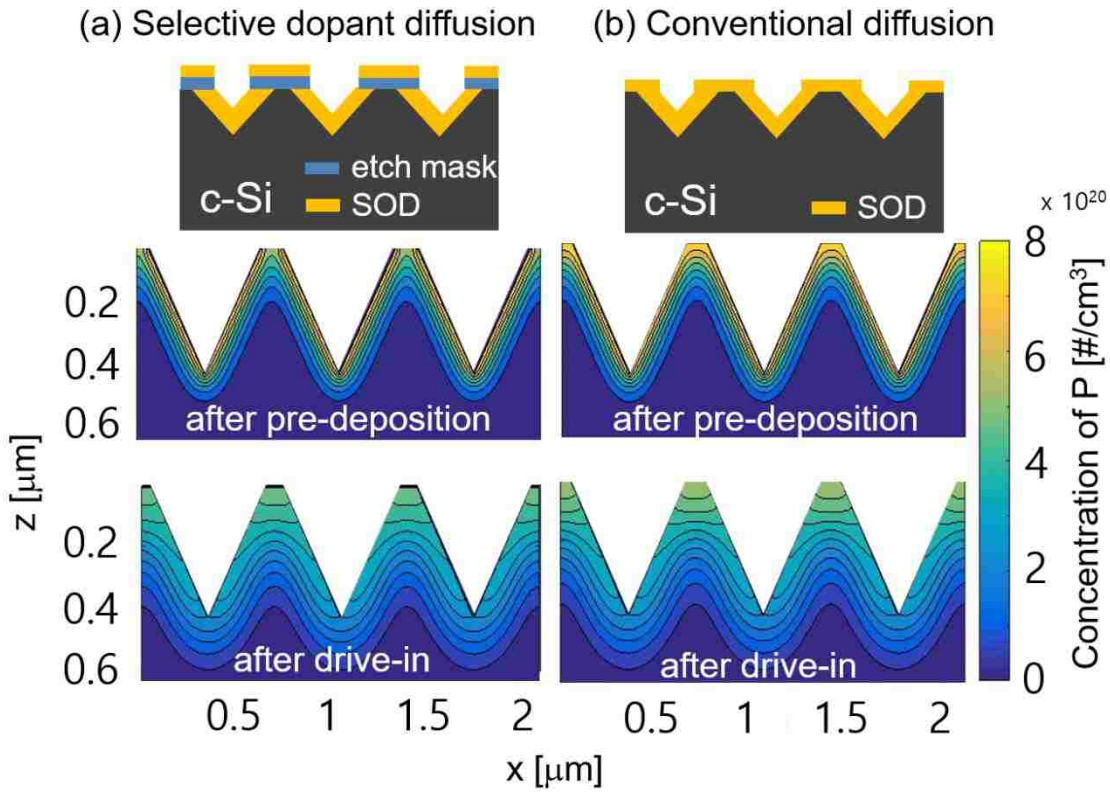

Figure 4.6. Calculated dopant concentration profile in periodic triangular grooves for (a) dopant diffusion through selective regions of the surface and (b) conventional diffusion after pre-deposition and drive-in.

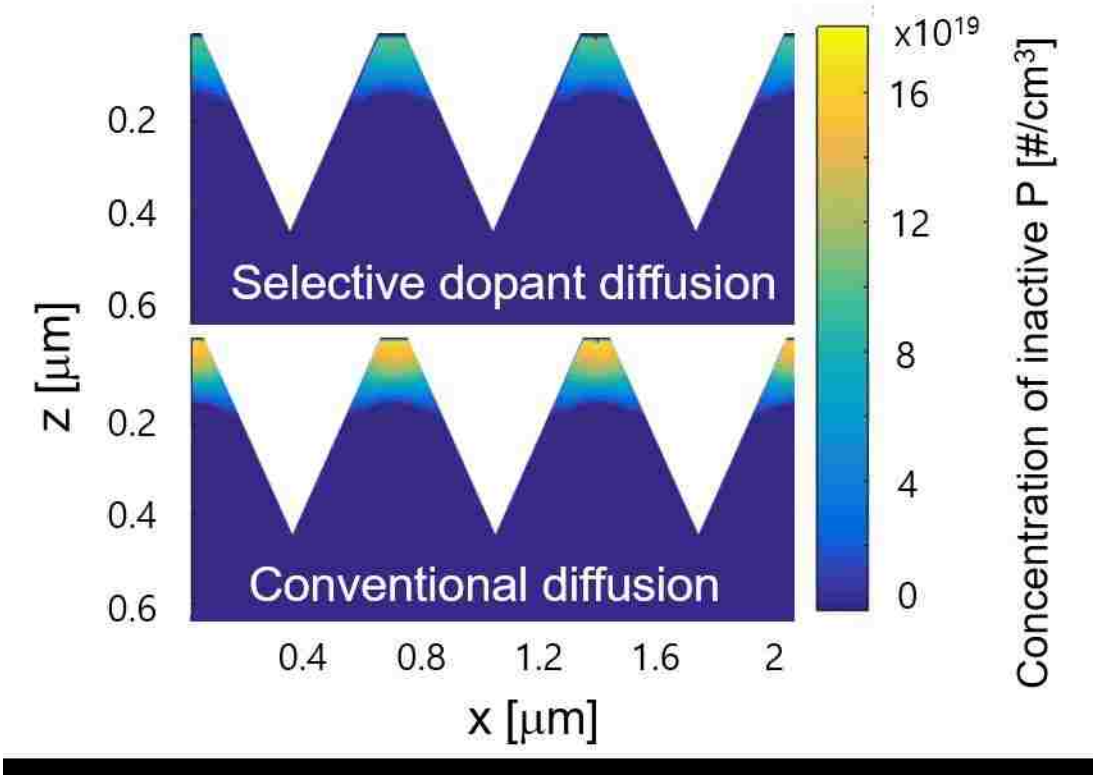

Figure 4.7. Electrically inactive dopant concentration extracted from Figure 4.6.

4.3. Application to Thin c-Si Solar Cells

Figure 4.8 shows a process flow for fabrication of three different types of thin c-Si solar cells: (1) a C_{4v} symmetry structured thin c-Si solar cell (through a blue colored path), (2) a C_2 symmetry structured thin c-Si solar cell (through a red colored path), and (3) a C_{4v} symmetry structured thin c-Si solar cell with dopant diffusion through selective regions of the surface (through a green colored path). The first two samples, (1) and (2), are for investigating the effect of inverted nanopyramid array's symmetry on the efficiency of thin c-Si solar cells. The samples with the same C_{4v} symmetry structure, (1) and (3), are used for comparing photovoltaic efficiencies between a thin c-Si solar cell fabricated by conventional diffusion and a thin c-Si solar cell fabricated by dopant diffusion through the selective regions of the surface.

To make thin c-Si solar cells, p-type Float-zone 250-μm-thick c-Si wafers were thinned down to 14 μm as described in Section 3.2. The thinned c-Si wafers were free-standing without frames, and there were no issues on handling by tweezers. The surface flatness of thinned c-Si wafers was good enough for an application of interference lithography as shown in Section 3.2. A 30-nm-thick Si_3N_4 layer for a KOH etch mask was deposited on the thinned c-Si wafer as described in Section 3.3.1. When the Si_3N_4 film was thicker than 30 nm, tensile stress was developed between a Si_3N_4 layer and a c-Si layer, hence the underlying thin c-Si wafer was bent. Two different lattice types of etch mask openings, a square lattice for a C_{4v} symmetry structure and a rotated rectangular lattice for a C_2 symmetry structure, were fabricated by interference lithography and reactive ion etching (RIE) as discussed in Section 3.3.3 and 3.3.4. Then, the samples were etched in a KOH solution to define an inverted nanopyramid

array on the free-standing thin c-Si wafers as described in Section 3.3.5. For fabrication of pn-junctions, the etch masks were removed, and the phosphorous dopant pre-deposition was performed at 960 ^{o}C for 2 hours as described in Section 3.4.1 (C_{4v} and C_2 symmetries cells through the blue and red paths, respectively). In case for the solar cell with dopant diffusion through selective regions, the etch mask was not removed to be used as a diffusion barrier in pre-deposition as introduced in Section 4.2 (a C_{4v} symmetry cell through the green path). Then, all the samples were cleaned, and the surfaces were passivated by thermally grown 1.2 nm-thick SiO_2 layers as described in Section 3.4.2.1. Remaining dangling Si bonds were terminated by hydrogen (Si-H) using forming gas (H_2) annealing at 400 ^{o}C for 10 minutes. 50-nm-thick i-aSi layers were deposited on top and bottom of the cell by PECVD as described in Section 3.4.2.2, and the sample was continued to the drive-in for crystallization and bi-directional dopant diffusion as described in Section 3.4.2.3. During the drive-in, the temperature was slowly ramped from 200 to 950 ^{o}C at the rate of 83 ^{o}C/hour to crystallize i-aSi layers. The bi-directional drive-in was performed at 950 ^{o}C for 3 hours and formed highly doped poly-Si layers for ohmic contacts of electrodes. These diffusion conditions and passivation approaches led to fill factor of 75% in our experiment. As described in Section 3.4.3, the e-beam evaporator was used for depositing a metal contact grid (20-nm-thick-Ti/1500-nm-thick-Ag/20-nm-thick-Pd) and a metal reflector (1500-nm-thick-Ag) on the top and bottom of the cell, respectively. Then an anti-reflective Si_3N_4 layer (90-nm-thick with a refractive index of 1.9 at 633 nm of wavelength) was deposited by PECVD on the top of the solar cell as discussed in Section 3.4.4.

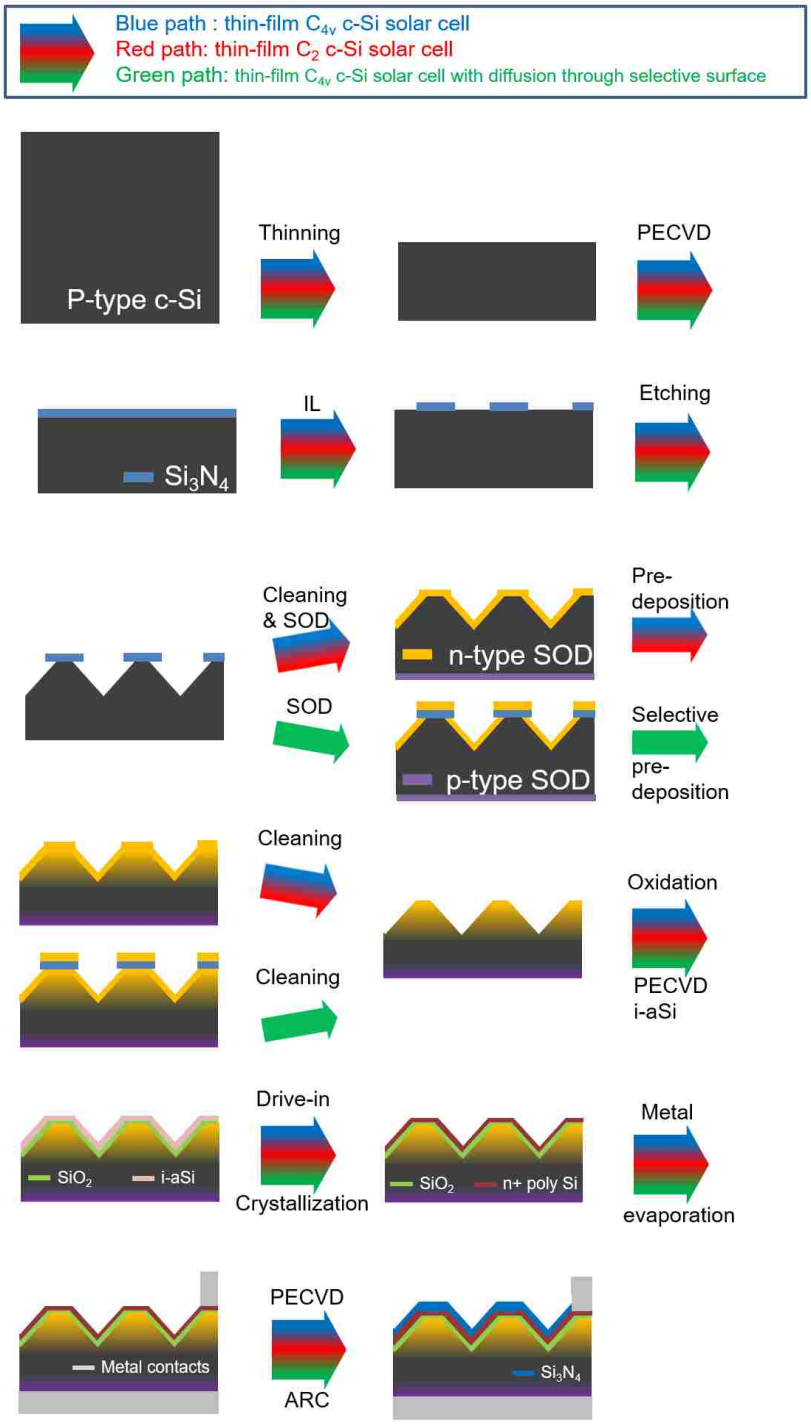

Figure 4.8. A fabrication process flow for various types of thin c-Si solar cells, a C_{4v} symmetry of inverted nanopyramid array thin c-Si solar cells (through a blue path), a C_2 symmetry of inverted nanopyramid array thin c-Si solar cells (through a red path), and a C_{4v} symmetry of inverted nanopyramid array thin c-Si solar cells with dopant diffusion through the selective regions of the surface(through a green path).

Figure 4.9 (a)-(c) show top view SEM images of inverted nanopyramid arrays of (a) a reference C_{4v} symmetry solar cell, (b) a symmetry broken C_2 symmetry solar cell, and (c) a C_{4v} symmetry solar cell processes by dopant diffusion through selective regions of the surface. As discussed in Section 4.1, we targeted lattice types and periodicities of C_{4v} and C_2 symmetry inverted nanopyramid array as a square lattice with periodicities of 700 nm × 700 nm and a rotated rectangular lattice with periodicities of 800 nm × 900 nm, respectively. The actual periodicities are shown in Figure 4.9 (a)-(c). Notice that we fabricated the identical C_{4v} symmetry inverted nanopyramid arrays [Figure 4.9 (a) & (c)] to check the effect of dopant diffusion through selective regions of the surface on solar cells, eliminating the effect of light-trapping nanostructures. The symmetry-broken C_2 symmetry structure [Figure 4.9 (b)] had a rotated rectangular lattice (785 nm x 900 nm). For fabrication of pn-junction, we removed Si_3N_4 etch masks on the samples with the C_{4v} and C_2 symmetry inverted nanopyramid arrays [Figure 4.9 (a) & (b)] before pre-deposition. On the other hand, the sample with the C_{4v} symmetry inverted nanopyramid array [Figure 4.9 (c)] was proceeded for dopant diffusion through selective regions of the surface without removing the etch mask. In this case, the etch mask was used as a diffusion barrier for pre-deposition. Figure 4.9 (d)-(f) show the cross-sectional SEM images of a C_{4v} reference solar cell, a C_2 symmetry solar cell, and a C_{4v} symmetry solar cell processed with dopant diffusion through selective regions of the surface, respectively. All the solar cells had almost the same thickness of c-Si layer.

Figure 4.10 (a)-(c) show photographs of free-standing 14-μm-thick c-Si solar cells. Top metal contact grids were on the nanopyramid arrays, and diffraction patterns were visible on top metal grids. The sizes of the solar cells were about 1 cm × 0.5 cm.

We are fabricating a full size (1.4 cm × 2.5 cm) solar cell with a wavy shaped c-Si substrate, and it will be introduced in Section 5.2 as future work.

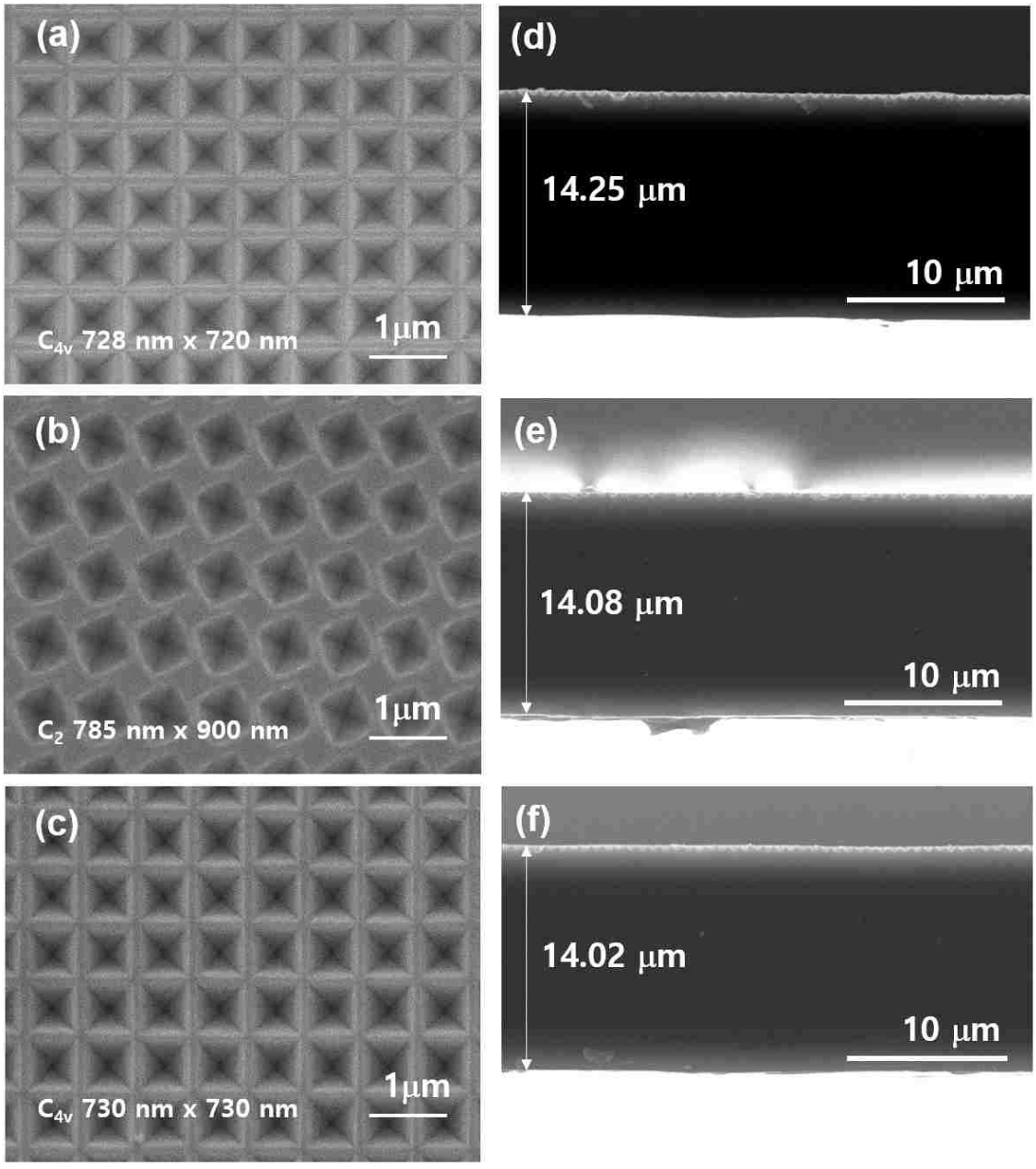

Figure 4.9. Top view SEM images of inverted nanopyramid arrays on thin c-Si solar cells: (a) a C_{4v} symmetry for a reference solar cell, (b) a C_2 symmetry for a reduced symmetry solar cell, and (c) a C_{4v} symmetry for dopant diffusion through selective regions of the surface. (d)-(f) show side view SEM images of each solar cell.

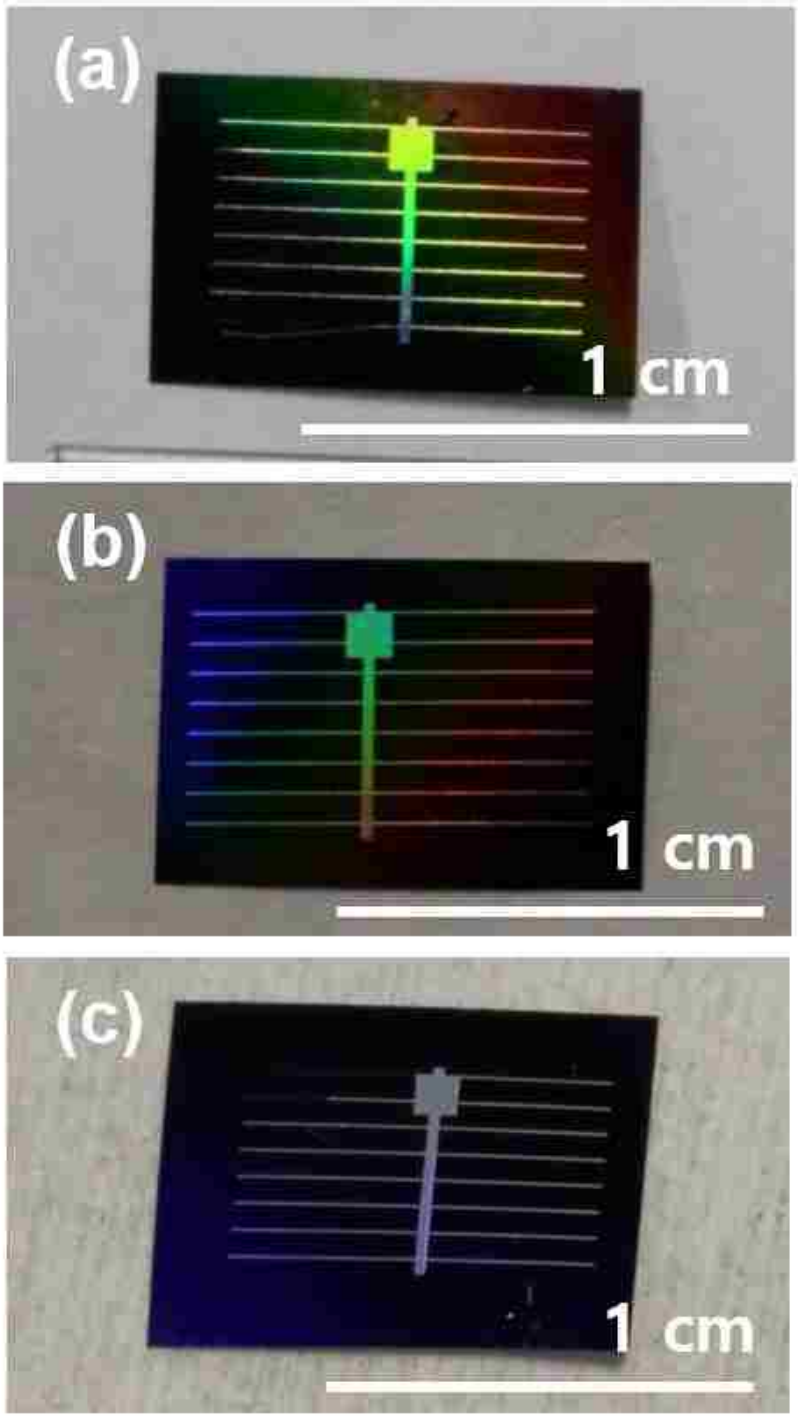

Figure 4.10. Photographs of fabricated 14-μm-thick c-Si solar cells with (a) a C_{4v} light trapping reference structure, (b) a symmetry-broken C_2 symmetry structure, and (c) a C_{4v} symmetry structure processed by dopant diffusion through selective regions of the surface.

We measured I-V characteristics of the solar cells using a source meter (Keithley 2400). A voltage bias was linearly increased from -0.5 V to 0.7 V with a constant step size of 0.018 V. A probing station including four-point sensors and a vacuum stage (TFI-5M, PV Measurements) was used for voltage sweeps. For light I-V characteristics, the cells were illuminated by a light beam of the AM1.5 spectrum from a solar simulator (ABET, LS-150). The power of the beam was measured by a thermopile sensor (Newport, 919P-003-10) to set the power of the light to be 1000 W/cm^2. Figure 4.11 shows an example of an I-V characterization of a solar cell under a solar simulator.

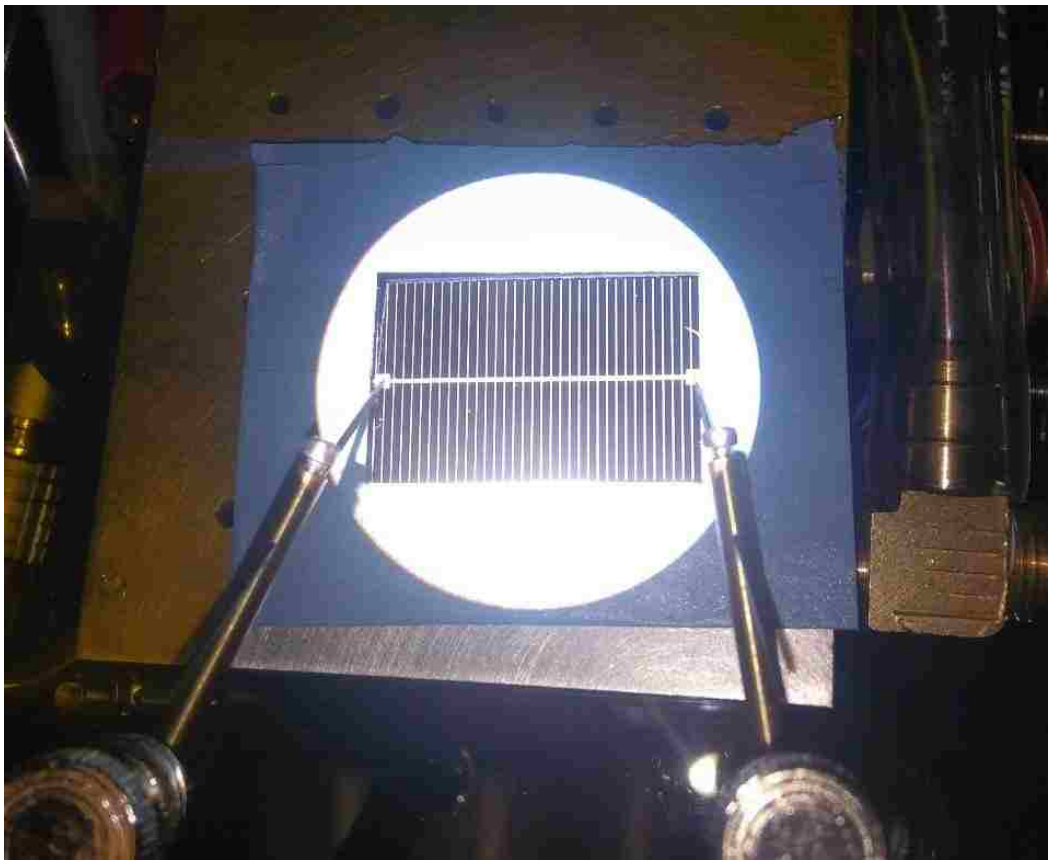

Figure 4.11. An optical image of a flat solar cell on a vacuum probe station for a light I-V characterization.

The light I-V characteristics of three different thin c-Si solar cells are shown in Figure 4.12. As the symmetry of inverted nanopyramid array was reduced from C_{4v} (solid blue line) to C_2 (dash-dot red line), the short circuit current density (J_{sc}) was enhanced from 28.2 mA/cm^2 to 29.9 mA/cm^2. The optical calculations and experiments in Section 4.1 showed that the symmetry reduction of inverted nanopyramid array from C_{4v} to C_2 increased light absorption by increasing the number of absorption peaks. The enhanced light absorption generates more charge carriers in a solar cell. Hence, the short circuit current can be increased. We investigated the optical properties (total reflectance and transmittance) of solar cells by a Spectrometer (VERTEX 70, Bruker and Lambda 950, Perkin-Elmer) with an integrating sphere (A562, Bruker). The inset SEM images in Figure 4.13 show six inverted nanopyramids of C_{4v} and C_2 symmetry arrays. The maximum absorption was about 86% because of the shaded area from top metal contact grids. The shaded area of our solar cells was about 10% of the active solar cell area. Figure 4.13 shows a clear enhancement of total light absorption in the thin c-Si solar cell with a C_2 symmetry inverted nanopyramid array. The efficiency enhancement due to the symmetry breaking of nanopyramids was 1.1%, and it was mainly due to the enhancement in J_{sc}. The I-V curves (solid blue line vs. dashed green line) in Figure 4.12 demonstrate that the dopant diffusion through the selective regions of the surface increases both fill factor (FF) and open circuit voltage (V_{oc}). In this case, the J_{sc} stayed at the same level because the symmetry and the lattice constants of nanopyramid arrays were almost identical. This effect amounted to an increase of photovoltaic efficiency from 12.5% to 13.3%.

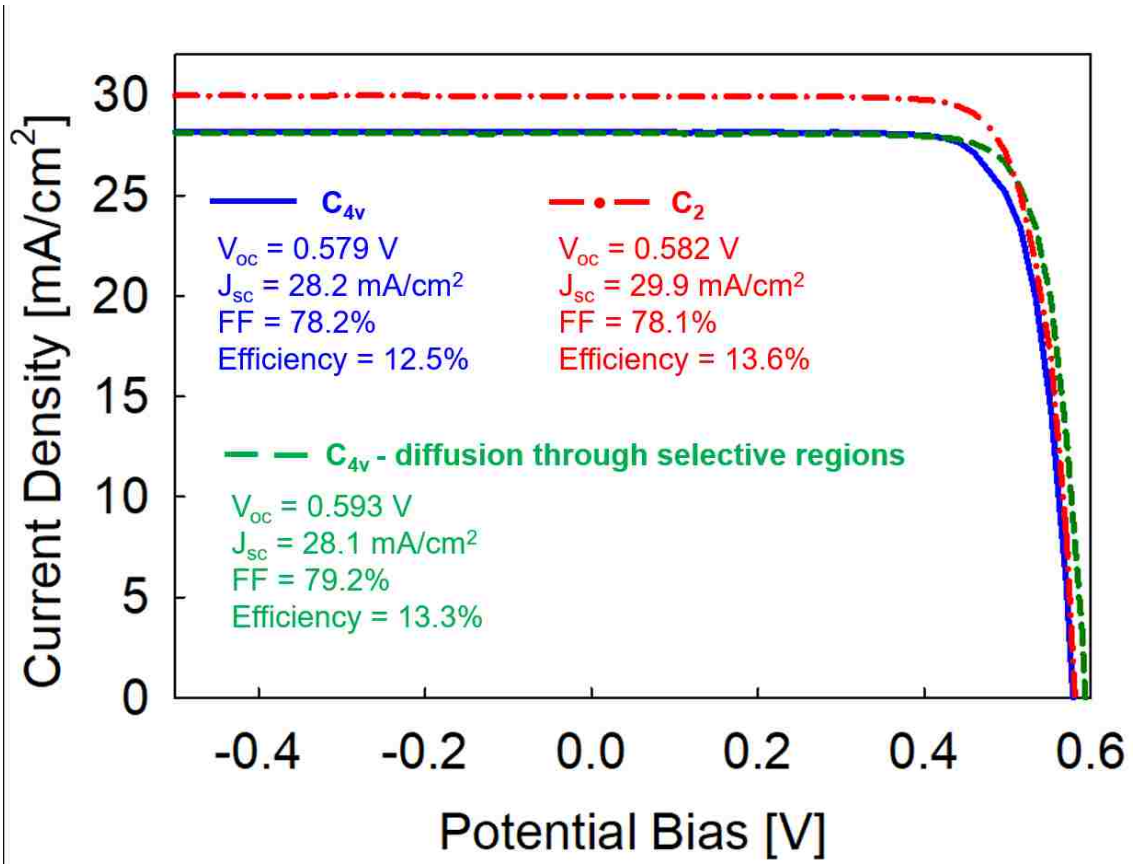

Figure 4.12. Comparison of I-V curves among a C_{4v} thin c-Si solar cell (solid blue line), a C_2 thin c-Si solar cell (dash-dot red line), and a C_{4v} thin c-Si solar cell with dopant diffusion through the selective regions of the surface (dashed green line).

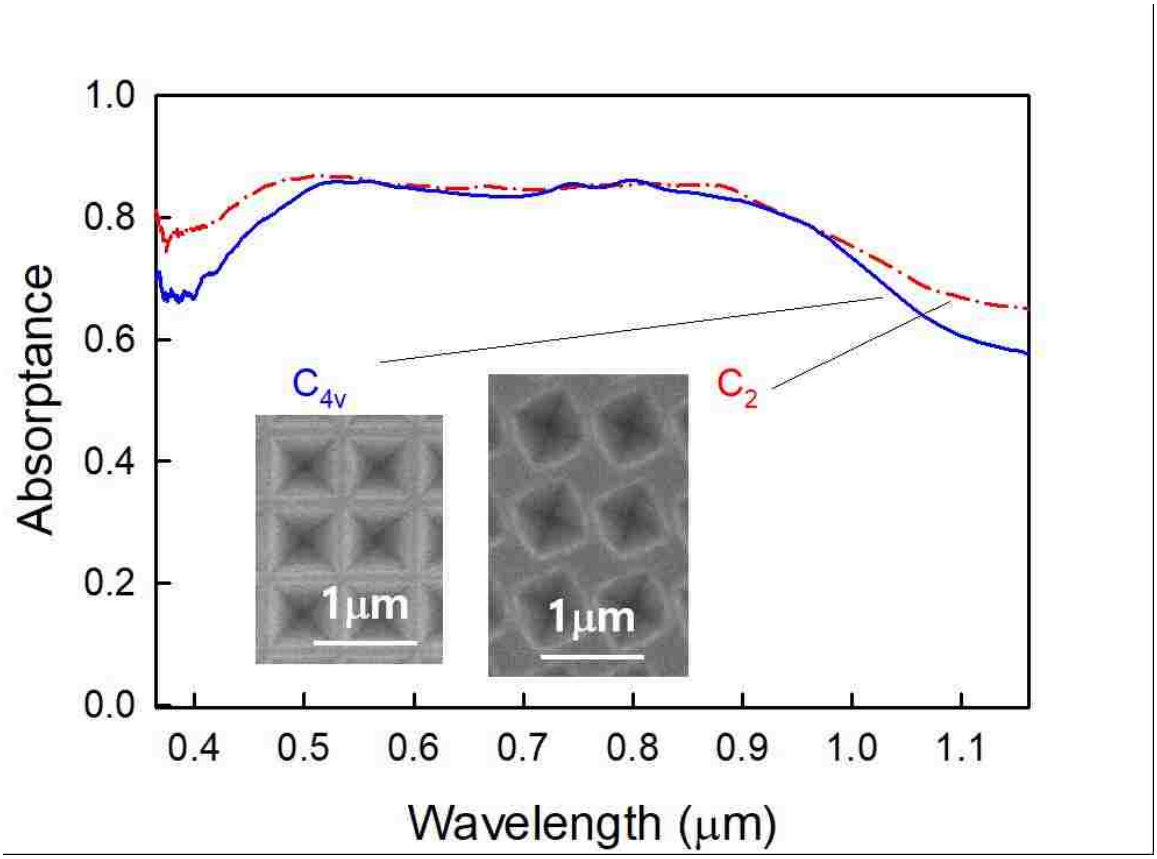

Figure 4.13. Comparison of total absorptance between C_{4v} and C_2 symmetry inverted nanopyramids thin c-Si solar cells. Inset SEM images show six inverted nanopyramids of each structure.

5. CONCLUSION AND FUTURE WORKS

5.1. Conclusion

An application of inverted nanopyramid arrays to thin c-Si solar cells has been investigated in two different aspects, an optical property and an electrical property of solar cells.

For further enhancement of light absorption in thin c-Si solar cells, a simple method to systematically break the symmetry on inverted nanopyramid array has been introduced. This method makes use of cost-effective and manufacturable wet etching steps directly applicable to kerfless or thinned c-Si films. Following this approach, the symmetry was reduced from C_{4v} to C_4 to C_2. Our experiment and calculation results show that the optical absorptance increases with the symmetry breaking. As the symmetry of the inverted nanopyramid array is broken in the sequence of $C_{4v} \rightarrow C_4 \rightarrow C_2$, the light trapping efficiency would increase along the path. In this research, the optimized inverted nanopyramid array for thin c-Si solar cells was C_2 symmetry structure with a rotated rectangular lattice of 800 nm × 900 nm. In general, the number of absorption peaks can be increased by breaking the symmetry of the inverted nanopyramid array.

The C_{4v} (700 nm × 700 nm) and C_2 (800 nm × 900 nm) symmetry thin c-Si solar cells have been fabricated on a thinned 14-μm-thick c-Si wafer. Our experiments show that the total light absorption of a thin c-Si solar cell is improved as the symmetry of inverted nanopyramid array is reduced from C_{4v} to C_2. Our I-V characteristic experiments show that the photovoltaic efficiency increased from 12.5% to 13.6% as the

symmetry was broken from C_{4v} to C_2, and the enhancement of solar cell efficiency was attributed to an increase of short circuit current.

When nanostructure is integrated into thin solar cells, strong doping inhomogeneity can develop while a pn-junction is made along a nanostructured surface. Such inhomogeneity often develops when the texture size is comparable to or smaller than the characteristic diffusion length, and the inhomogeneity decreases solar cell efficiency significantly. Our calculations show that dopant concentration along a textured surface can vary by a factor of two when conventional diffusion is performed.

To improve inhomogeneity in dopant concentration, we introduced a unique method for dopant diffusion through the selective regions of the surface. The method uses a KOH etch mask as a diffusion barrier for pre-deposition. In this case, the inhomogeneity is reduced by diffusing dopant atoms through the selective regions of the surface exposed by an etch mask remaining on the surface after texturing. Our 14-μm-thick c-Si solar cell which was fabricated by the dopant diffusion through selective regions increased photovoltaic efficiency from 12.5% to 13.3% by increasing both open circuit voltage and fill factor. While we demonstrate the effectiveness of the dopant diffusion through selective regions of the surface in thin c-Si solar cells, our method would be broadly applicable to other semiconductor materials, light-trapping structures, and optoelectronic devices.

5.2. Future Work

In this study, the solar cells have been fabricated through the process flows shown in Figure 4.5. There is another version of the solar cell fabrication process which can

provide much better open circuit voltage (0.64 V). The disadvantage of this fabrication process is taking longer time to finish the solar cell. I have further modified this fabrication process by integrating three processing steps, crystallization, PECVD, and drive-in, into a single step. This modified process sacrifices the efficiency of the solar cells for the better reproducibility of results with simplified experiments. However, I am still suspecting that my modified fabrication processes have not drawn the full potential of solar efficiencies. Therefore, if we solve the reproducibility issues in the old fabrication processes, I am expecting a thin (5-15 μm) c-Si solar cell with a C_1 or C_2 inverted nanopyramid array fabricated by the old process flow shown in Figure 5.1 can achieve an efficiency level close to the world's record.

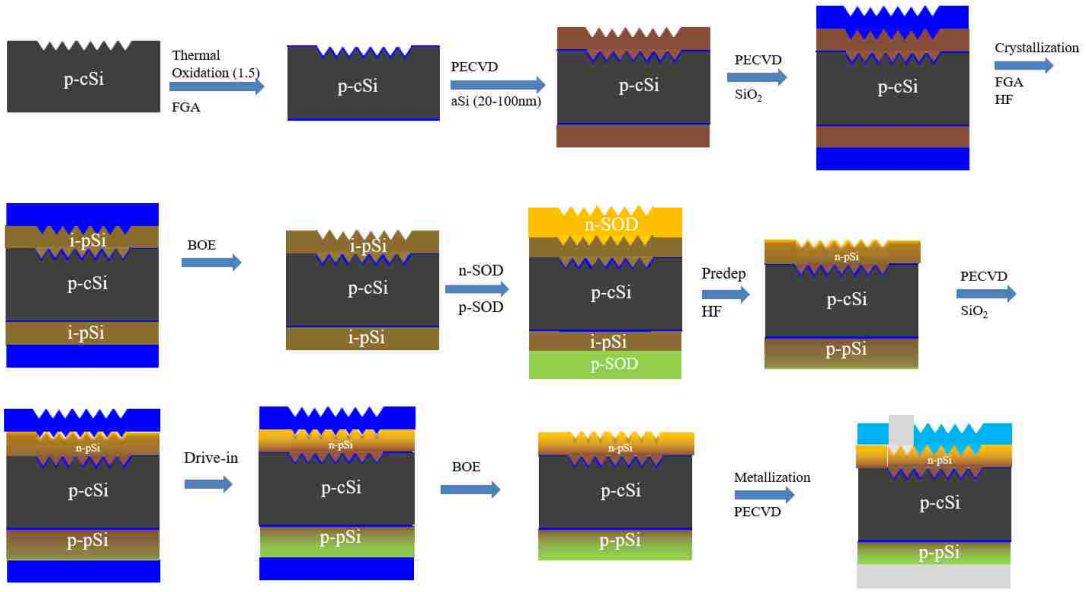

Figure 5.1. The process flow for better photovoltaic efficiency with ~0.64 V of V_{oc} and 75% of FF. This process flow still needs to be optimized for better reproducibility.

A free-standing thinned c-Si wafer has excellent flexibility. A solar cell on Ethylene-vinyl acetate (EVA) can be cured on a wavy shaped polymer substrate to transform the macroscopic geometry of a thin c-Si solar cell. The schematic diagram is

shown in Figure 5.2. This wavy structured solar cell will have advantages in macroscopic solar cell properties, better heat dissipation, improved impact resistance, and an additional geometric light trapping effect. Fabricating this wavy solar cell is in progress, and Figure 5.3 shows optical images of the wavy c-Si wafer.

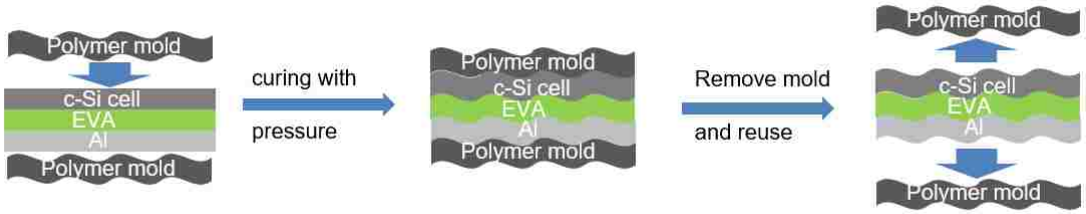

Figure 5.2. The process flow for fabricating various geometries of a solar cell with re-usable template molds.

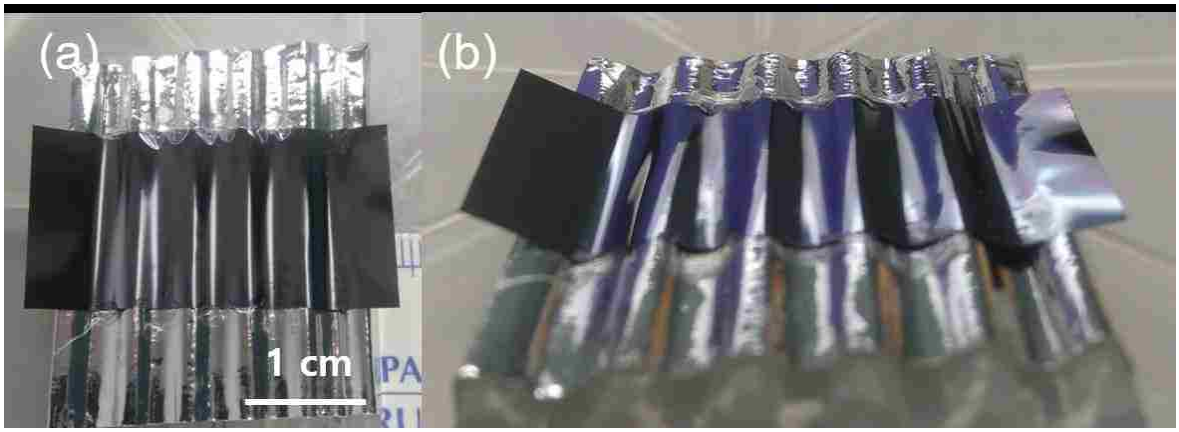

Figure 5.3. Optical images of a wavy shaped c-Si wafer from (a) a top view and (b) a bird's-eye view.

Highly boron-doped c-Si is often used as an etch stop layer [76], so boron diffusion through the selective regions of the surface shown in Section 4.2 can be used for fabricating a second etch mask. The first KOH etching step produces inverted pyramid structures, and the subsequent second KOH etching step after boron diffusion

through selective regions etches the region around the inverted nanopyramids. As a result, a new shape of nanostructure, volcano structure, can be fabricated as shown in Figure 5.4. Although it is not clear whether an optical response of the volcano structure is better than that of the inverted pyramids or not, the C_2 symmetry volcano structure can be fabricated without unetched area. As we manipulated interference lithography to fabricate various symmetries of inverted nanopyramid arrays, the unetched area was unavoidable as shown in Figure 3.8. This volcano structure can solve this problem.

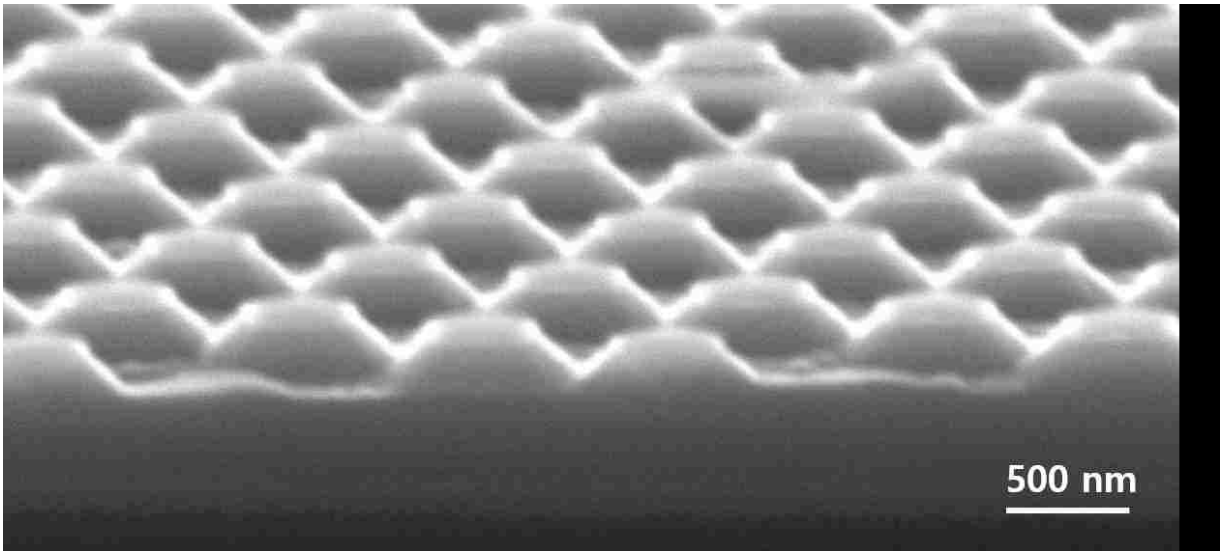

Figure 5.4. A SEM image of volcano structure after second KOH etching using a mask from the boron diffusion through selective regions of the surface.

SUMMARY IN KOREAN

결정질 실리콘 (crystalline silicon) 박막 태양전지는 가볍고 유연하여 자동차, 비행기, 이동식 군용 텐트 등에 이용 가능합니다. 필요한 실리콘의 양이 기존 태양전지의 1/10 수준으로 줄어 셀 제조 비용 또한 줄일 수 있습니다. 하지만, 빛 흡수층이 얇아 효과적인 태양 빛 흡수를 위해서는 효율적인 빛 가둠 (light trapping) 기술이 필요합니다.

본 연구에서는 결정질 실리콘 박막 태양전지의 효율을 높이고자 다양한 대칭성의 역나노피라미드 배열(inverted nanopyramid arrays)을 적용하였습니다. 다양한 대칭성의 역나노피라미드 구조를 얻기 위해 간단하고 예측 가능하며 비용이 효과적인 새로운 방법을 제시하였습니다. 일반적으로 대칭성이 줄어들면 중첩된(degenerated) 흡수피크(absorption peaks)가 나누어지고 새로운 공명의 흡수피크를 만들어내 태양전지의 빛 흡수가 증가합니다.

태양전지 나노 구조 배열의 대칭성이 $C_{4v} \rightarrow C_4 \rightarrow C_2$ 로 줄어들 때 실리콘층의 빛흡수가 증가함을 컴퓨터 시뮬레이션과 광학실험을 통해 확인하였습니다. 태양전지 적용에 최적화된 구조는 C_2 대칭성을 갖고, 800 nm × 900 nm의 직사각형 격자구조가 실리콘 [100] 방향을 따라 실리콘 [110]으로부터 약 22.5 도 회전한 역나노피라미드 배열의 구조입니다.

이러한 나노 구조를 태양전지에 적용할 때 태양전지의 전자기적 현상 또한 고려해야 합니다. PN 접합이 나노 구조를 따라 확산에 의해 형성될 때 도펀트의 농도는 나노 구조의 위치에 따라 불균일해 졌고, 이는 컴퓨터 시뮬레이션을 통해 확인하였습니다. 이러한 농도의 불균일함은 태양전지의

효율에 악영향을 미치므로 이를 해결하기 위해 나노 구조를 만드는 데 사용했던 마스크를 재활용하여 도펀트의 선택적 확산 방법을 제시하였습니다.

세 가지 종류의 박막 태양전지를 제작하여 태양전지의 효율에 대칭성과 선택적 확산이 어떻게 영향을 미치는지 실험하였습니다. 태양전지 나노 구조의 대칭성이 줄어들 때 효율이 12.5%에서 13.6%로 좋아짐을 확인하였습니다. 이는 효율적인 빛흡수를 통해 더 많은 전하 캐리어(charge carriers)가 생성되어 단락 전류(short circuit current)가 증가했기 때문입니다. 선택적 확산을 이용해 만든 태양전지의 경우 개방 회로 전압(open circuit voltage)과 채우기 팩터(fill factor)가 증가하였으며 이로 인해 효율은 12.5%에서 13.3%로 증가하였습니다

REFERENCES

[1] M. P. Thekaekara, R. Kruger, and C. H. Duncan, “Solar Irradiance Measurement from a Research Aircraft,” *Applied Optics*, 8, pp.1713-1732, 1969

[2] “Terrestrial Photovoltaic Measurement Procedures,” *Report ERDA/NASA/1022-77/16*, June 1977

[3] B. C. Boots, *Egy123a - alternative photovoltaic solar cell technologies: Global markets*; BCC Research: 2014.

[4] International technology roadmap for photovoltaic (itrpv), 6th ed.; July 2015, http://www.itrpv.net/Reports/Downloads/.

[5] M. S. Branham, W.-C. Hsu, S. Yerci, J. Loomis, S. V. Boriskina, B. R. Hoard, S. E. Han, and G. Chen, "15.7% efficient 10-μm-thick crystalline silicon solar cells using periodic nanostructures," *Adv. Mater.*, 27(13), pp. 2182-2188, 2015

[6] S. Pillai, K. R. Catchpole, T. Trupke, and M. A. Green, “Surface plasmon enhanced silicon solar cells,” *J. Appl. Phys.* 101(9), 093105, 2007.

[7] H. A. Atwater and A. Polman, "Plasmonics for improved photovoltaic devices," *Nature Mater.*, 9(3), pp. 205-213, 2010

[8] K. R. Catchpole and A. Polman, "Plasmonic solar cells," *Opt. Express*, 16(26), pp. 21793-21800, 2008

[9] H. R. Stuart and D. G. Hall, "Absorption enhancement in silicon-on-insulator waveguides using metal island films," *Appl. Phys. Lett.* 69(16), pp. 2327-2329, 1996

[10] E. Yablonovitch, "Statistical ray optics," *J. Opt. Soc. Am.*, 72(7), pp. 899-907, 1982

[11] K. Vynck, M. Burresi, F. Riboli, and D. S. Wiersma, "Photon management in two-dimensional disordered media," *Nature Mater.* 11(12), pp. 1017-1022, 2012

[12] A. Oskooi, P. A. Favuzzi, Y. Tanaka, H. Shigeta, Y. Kawakami, and S. Noda, "Partially disordered photonic-crystal thin films for enhanced and robust photovoltaics," *Appl. Phys. Lett.* 100(18), p. 181110, 2012

[13] V. E. Ferry, M. A. Verschuuren, H. B. T. Li, E. Verhagen, R. J. Walters, R. E. I. Schropp, H. A. Atwater, and A. Polman, “Light trapping in ultrathin plasmonic solar cells,” *Optics Express*, 18(S2), pp. A237-A245, 2010

[14] S. E. Han and G. Chen, "Optical absorption enhancement in silicon nanohole arrays for solar photovoltaics," *Nano Lett.*, 10(3), pp. 1012-1015, 2010

[15] L. Hu and G. Chen, "Analysis of optical absorption in silicon nanowire arrays for photovoltaic applications," *Nano Lett.,* 7(11), pp. 3249-3252, 2007

[16] E. Garnett and P. Yang, "Light trapping in silicon nanowire solar cells," *Nano Lett.*, 10(3), pp. 1082-1087, 2010

[17] M. D. Kelzenberg, S. W. Boettcher, J. A. Petykiewicz, D. B. Turner-Evans, M. C. Putnam, E. L. Warren, J. M. Spurgeon, R. M. Briggs, N. S. Lewis, and H. A. Atwater, "Enhanced absorption and carrier collection in Si wire arrays for photovoltaic applications," *Nature Mater.*, 9(3), pp. 239-244, 2010

[18] M. D. Kelzenberg, D. B. Turner-Evans, M. C. Putnam, S. W. Boettcher, R. M. Briggs, J. Y. Baek, N. S. Lewis, and H. A. Atwater, "High-performance Si microwire photovoltaics," *Energ. Environ. Sci.,* 4(3), pp. 866-871, 2011

[19] O. L. Muskens, J. G. Rivas, R. E. Algra, E. P. A. M. Bakkers, and A. Lagendijk, "Design of light scattering in nanowire materials for photovoltaic applications," *Nano Lett.,* 8(9), pp. 2638-2642, 2008

[20] K. Peng, Y. Xu, Y. Wu, Y. Yan, S.-T. Lee, and J. Zhu, "Aligned single-crystalline Si nanowire arrays for photovoltaic applications," *Small,* 1(11), pp. 1062-1067, 2005

[21] L. Tsakalakos, J. Balch, J. Fronheiser, B. A. Korevaar, O. Sulima, and J. Rand, "Silicon nanowire solar cells," *Appl. Phys. Lett.*, 91(23), pp. 233117-233113, 2007

[22] C. Lin and M. L. Povinelli, "Optical absorption enhancement in silicon nanowire arrays with a large lattice constant for photovoltaic applications," *Opt. Express*, 17(22), pp. 19371-19381, 2009

[23] S. L. Diedenhofen, O. T. A. Janssen, M. Hocevar, A. Pierret, E. P. A. M. Bakkers, H. P. Urbach, and J. G. Rivas, “Controlling the Directional Emission of Light by Periodic Arrays of Heterostructured Semiconductor Nanowires,” *ACS Nano*, 5(7), pp. 5830-5837, 2011.

[24] S. E. Han and G. Chen, "Toward the Lambertian limit of light trapping in thin nanostructured silicon solar cells," *Nano Lett.,* 10(11), pp. 4692-4696, 2010

[25] P. Bermel, C. Luo, L. Zeng, L. C. Kimerling, and J. D. Joannopoulos, "Improving thin-film crystalline silicon solar cell efficiencies with photonic crystals," *Opt. Express*, 15(25), pp. 16986-17000, 2007

[26] A. Chutinan, N. P. Kherani, and S. Zukotynski, "High-efficiency photonic crystal solar cell architecture," *Opt. Express*, 17(11), pp. 8871-8878, 2009

[27] S. B. Mallick, M. Agrawal, and P. Peumans, "Optimal light trapping in ultra-thin photonic crystal crystalline silicon solar cells," *Opt. Express*, 18(6), pp. 5691-5706, 2010

[28] J. N. Munday and H. A. Atwater, "Large integrated absorption enhancement in plasmonic solar cells by combining metallic gratings and antireflection coatings," *Nano Lett.*, 11(6), pp. 2195-2201, 2010

[29] H. Sai, Y. Kanamori, K. Arafune, Y. Ohshita, and M. Yamaguchi, "Light trapping effect of submicron surface textures in crystalline Si solar cells," *Prog. Photovolt. Res. Appl.*, 15(5), pp. 415-423, 2007

[30] P. Sheng, A. N. Bloch, and R. S. Stepleman, "Wavelength-selective absorption enhancement in thin-film solar cells," *Appl. Phys. Lett.*, 43(6), pp. 579-581, 1983

[31] D. Zhou and R. Biswas, "Photonic crystal enhanced light-trapping in thin film solar cells," *J. Appl. Phys.*, 103(9), pp. 093102-093105, 2008

[32] A. Mavrokefalos, S. E. Han, S. Yerci, M. S. Branham, and G. Chen, "Efficient light trapping in inverted nanopyramid thin crystalline silicon membranes for solar cell applications," *Nano Lett.* 12(6), pp. 2792-2796, 2012

[33] M. Peters, C. Battaglia, K. Forberich, B. Bläsi, N. Sahraei, and A. G. Aberle, "Comparison between periodic and stochastic parabolic light trapping structures for thin-film microcrystalline Silicon solar cells," *Opt. Express*, 20(28), pp. 29488-29499, 2012

[34] B. Hoex, J. Schmidt, P. Pohi, M. C. M. Sanden, and W. M. M. Kessels, "Silicon surface passivation by atomic layer deposited Al_2O_3," *J. Appl. Phys*., 104, p. 044903 2008

[35] B. Nemeth, D. L. Young, M. R. Page, V. Lasalvia, S. Johnston, R. Reedy, and P. Stradins, "Polycrystalline silicon passivated tunneling contacts for high efficiency silicon solar cells,", *J. of Mat. Res.*, 31(6), pp. 671-681, 2016

[36] A. G. Aberle, "Surface passivation of crystalline silicon solar cells: a review," *Progress in Photovoltaics: Research and Applications*, 8 (5), pp. 473-487, 2000

[37] B. L. Sharma, "Diffusion in semiconductors," *Trans. Tech. Pub. Germany*, 87, 1970

[38] S. M. Sze and J. Irwin, "Resistivity, mobility and impurity levels in GaAs, Ge, and Si at 300°K," *Solid State Electronics*, 11, p.599-602, 1968

[39] S. Sivasubramaniam and M. M.Alkaisi, "Inverted nanopyramid texturing for silicon solar cells using interference lithography," *Microelectronic Engineering*, 119, pp. 146-150, 2014

[40] D. Shi, Y. Zeng, and W. Shen, "Perovskite/c-Si tandem solar cell with inverted nanopyramids: realizing high efficiency by controllable light trapping," *Scientific Reports*, 5, 16504, 2015

[41] G. Li, H. Li, J. Y. L. Ho, M. Wong, and H. S. Kwok, “Nanopyramid Structure for Ultrathin c-Si Tandem Solar Cells,” *Nano Lett.*, 14 (5), pp 2563–2568, 2014

[42] S. Zhou, Z. Yang, P. Gao, X. Li, X. Yang, D. Wang, J. He, Z. Ying, and J. Ye, Nanoscale Research Letters, 11(194), 2016

[43] A.W.Smith and A.Rohatgi, “Ray tracing analysis of the inverted pyramid texturing geometry for high efficiency silicon solar cells,” 29(1), pp.37-49, 1993

[44] H. Siedel, L. Csepregi, A. Heuberger, and H. Baumgarter, “Anisotropic Etching of Crystalline Silicon in Alkaline Solutions,” *J. Electrochem. Soc.*, 137, p. 3616, 1990

[45] M.Shikida, K. Sato, K. Tokoro, and D. Uchikawa, “Differences in anisotropic etching properties of KOH and TMAH solutions,” *Sensors and Actuators A: Physical*, 80, pp. 179-188, 2000

[46] K. E.Bean, “Anisotropic Etching of Silicon”, *IEEE Transactions on Electron Devices*, 25, pp. 1185-1193, 1978

[47] H. Angermann, W. Henrion, A. Roseler, and M. Robien, “Wet-chemical passivation of Si(111)- and Si(100)-substrates,” *Material Science and Engineering B*, 73, pp. 178-183, 2000

[48] H. Angermann, W. Henrion, M. Robien, and A. Roseler, “Wet-chemical passivation and characterization of silicon interfaces for solar cell applications,” *Solar energy materials and solar cells*, 83, pp. 331-346, 2004

[49] H. R. Stuart and D. G. Hall, “Thermodynamic limit to light trapping in thin planar structures,” *J. Opt. Soc. Am. A*, 14(11), pp. 3001-3008, 1997

[50] T. Cai and S. E. Han, "Effect of symmetry in periodic nanostructures on light trapping in thin film solar cells," *J. Opt. Soc. Am. B*, 32(11), pp. 2264-2270, 2015

[51] J. Gjessing, A. S. Sudbø, and E. S. Marstein, "Comparison of periodic light-trapping structures in thin crystalline silicon solar cells," *J. Appl. Phys.*, 110(3), p. 033104, 2011

[52] C. Heine and R. H. Morf, "Submicrometer gratings for solar energy applications," *Appl. Opt.*, 34(14), pp. 2476-2482, 1995

[53] Z. Yu, A. Raman, and S. Fan, "Nanophotonic light-trapping theory for solar cells," *Appl. Phys. A*, 105(2), pp. 329-339, 2011

[54] S. V. Kesapragada and D. Gall, "Two-component nanopillar arrays grown by Glancing Angle Deposition," *Thin Solid Films* 494(1–2), 234-239 (2006)

[55] P. Campbell, S. R. Wenham, and M. A. Green, "Light trapping and reflection control in solar cells using tilted crystallographic surface textures," *Sol. Energy Mater. Sol. Cells* 31(2), pp. 133-153, 1993

[56] K. M. McPeak, C. D. van Engers, M. Blome, J. H. Park, S. Burger, M. A. Gosálvez, A. Faridi, Y. R. Ries, A. Sahu, and D. J. Norris, "Complex chiral colloids and surfaces via high-index off-cut silicon," *Nano Lett.* 14(5), 2934-2940 (2014)

[57] Y.-C. Chang, S.-C. Lu, H.-C. Chung, S.-M. Wang, T.-D. Tsai, and T.-F. Guo, "High-throughput nanofabrication of infra-red and chiral metamaterials using nanospherical-lens lithography," *Sci. Rep.* 33339 (2013)

[58] C. Battaglia, C.-M. Hsu, K. Söderström, J. Escarré, F.-J. Haug, M. Charrière, M. Boccard, M. Despeisse, D. T. L. Alexander, M. Cantoni, Y. Cui, and C. Ballif, "Light trapping in solar cells: Can periodic beat random?," *ACS Nano*, 6(3), pp. 2790-2797, 2012

[59] M. S. Branham, W.-C. Hsu, S. Yerci, J. Loomis, S. V. Boriskina, B. R. Hoard, S. E. Han, A. Ebong, and G. Chen, "Empirical comparison of random and periodic surface light-trapping structures for ultrathin silicon photovoltaics," *Adv. Opt. Mater.* 4(6), 858-863 (2016)

[60] V. E. Ferry, M. A. Verschuuren, M. C. v. Lare, R. E. I. Schropp, H. A. Atwater, and A. Polman, "Optimized spatial correlations for broadband light trapping nanopatterns in high efficiency ultrathin film a-Si:H solar cells," *Nano Lett.*, 11(10), pp. 4239-4245, 2011

[61] E. R. Martins, J. Li, Y. Liu, V. Depauw, Z. Chen, J. Zhou, and T. F. Krauss, "Deterministic quasi-random nanostructures for photon control," *Nat. Commun.*, p. 42665, 2013

[62] P. Campbell and M. A. Green, "Light trapping properties of pyramidally textured surfaces," *J. Appl. Phys.* 62(1), pp. 243-249, 1987

[63] J. I. Pankove, “Optical Processes in Semiconductors”, Englewood Cliffs, *N.J.: Prentice-Hall*, 1971

[64] M. A. Green, “Solar Cells: operating principles, technology and system application”, *University of New South Wales*, 1986

[65] J. C. C. Tsai, “Shallow Phosphorus Diffusion Profiles in Silicon”, *Proceedings: IEEE*, 57, pp. 1499-1506, 1969

[66] S. Solmi, A. Parisini, R. Angelucci, A. Armigliato, D. Nobili, and L. Moro, “Dopant and carrier concentration in Si in equilibrium with monoclinic SiP precipitates,” *Phys. Rev. B*, vol. 53, pp. 7836-7841, 1996

[67] J. Lindmayer and J. F. Allison, “The violet cell: an improved solar cell,” *IEEE Photovoltaic Specialists Conference*, Silver Spring, p.83, 1972

[68] J.R. Davis, A. Rohatgi, R.H. Hopkins, P.D. Blais, P. Rai-Choudhury, J.R. McCormick, and H.C. Mollenkopf, “Impurities in silicon solar cells,” *IEEE Transaction on Electron Devices*, vol.27, pp. 667-687, 1980

[69] C. T. Sah, R. N. Noyce, and W. Shockley, “Carrier generation and recombination in p-n junctions and p-n junction characteristics,” *Proceedings of the IRE 45*, p. 1228, 1957

[70] S. M. Sze and K. K. Ng, “Physics of Semiconductor Devices, 3rd Edition,” *Wiley*, 2006

[71] W.G. Pfann, “Zone Melting,” *Wiley*, 1966

[72] P. H. Keck and M. J. E. Golay, “Crystallization of Silicon from a Floating Liquid Zone,” *Phys. Rev.* 89, p. 1297, 1953

[73] S. Wang, B. D. Weil, Y. Li, K. X. Wang, E. Garnett, S. Fan, and Y. Cui, “Large-Area Free-Standing Ultrathin Single-Crystal Silicon as Processable Materials,” *Nano Lett.*, 13(9), pp.4393-4398, 2013

[74] D. B. Lee, “Anisotropic etching of silicon,” *J. of App. Phys.*, 40, p. 4596, 1969

[75] H.Tanakaac, S. Yamashitac, Y. Abec, M. Shikidab, and K. Satoa, “Fast etching of silicon with a smooth surface in high temperature ranges near the boiling point of KOH solution,” *Sensors and Actuators A: Physical*, 114, pp. 516-520 2004

[76] H. Seidel, L. Csepregi, A. Heuberger, and H. Baumgärtel, “Anisotropic Etching of Crystalline Silicon in Alkaline Solutions II . Influence of Dopants,” *J. Electrochem. Soc.*, 137, pp. 3626-3632, 1990

[77] A.E. amrani, I. Menous, L.Mahiou, R.Tadjine, A.Touati, and A.Lefgoum, “Silicon nitride film for solar cells,” *Renewable Energy*, 33, pp. 2289-2293, 2008

[78] S. J. Han, S. Ghosh, O. K. Abudayyeh, B. R. Hoard, E. C. Culler, J. E. Bonilla, S. M. Han, and S. E. Han, “Symmetry-breaking nanostructures on crystalline silicon for enhanced light trapping in thin film solar cells,” *Optics Express*, 24(26), pp. A1586-A1596, 2016

[79] C. J. Mogab, A. C. Adams, and D. L. Flamm, “Plasma etching of Si and SiO_2—The effect of oxygen additions to CF_4 plasmas,” *Journal of Applied Physics*, 49, pp. 3796-3803, 1978

[80] T. C. Mele, J. Nulman, and J. P. Krusius, “Selective and anisotropic reactive ion etch of LPCVD silicon nitride with CHF_3 based gases,” *Journal of Vacuum Science & Technology B,* 2, p.684, 1984

[81] D. K. Schroder, “Solar Cell Contact Resistance – A Review”, *IEEE Transactions on Electron Devices,* ED-31, pp. 637-647 (1984)

[82] B. E. Deal and A. S. Grove , “General relationship for the thermal oxidation of silicon,” *Journal of Applied Physics,* 36, pp. 3770-3778, 1965

[83] J. Perrin, J. Schmitt, C. Hollenstein, A. Howling, and L. Sansonnens, “The physics of plasma-enhanced chemical vapour deposition for large-area coating: industrial application to flat panel displays and solar cells,” *Plasma Phys. Control. Fusion,* 42, pp. B353–B363, 2000

[84] J. Perrin and C. Hollenstein, “Sources and growth of particles Dusty Plasmas: Physics, Chemistry and Technological Impacts in Plasma Processing*,” Wiley* p 77

[85] M. Serényi, C. Frigeri,, Z. Szekrényes, K. Kamarás, L. Nasi, A. Csik, and N. Q. Khánh, “On the formation of blisters in annealed hydrogenated a-Si layers,” *Nanoscale Res Lett.*, 8, p. 84, 2013

[86] A. Laskarakis, S. Logothetidis, E. Pavlopoulou, and M. Gioti, “Mueller matrix spectroscopic ellipsometry: formulation and application,” *Thin Solid Films*, 455-456, pp. 43-49, 2004

[87] F.L. Roy-Brehonnet and B.L. Jeune, “Utilization of Mueller matrix formalism to obtain optical targets depolarization and polarization properties,” Progress in Quantum Electronics, 21(2), pp. 109-151, 1997

[88] C. Kittel, Introduction to Solid State Physics. 8th ed.; *Wiley: USA*, 2004

[89] Y. Yin, Z.-Y. Li, and Y. Xia, "Template-directed growth of (100)-oriented colloidal crystals," *Langmuir,* 19(3), pp. 622-631, 2003

[90] P. M. Bell, J. B. Pendry, L. M. Moreno, and A. J. Ward, "A program for calculating photonic band structures and transmission coefficients of complex structures," *Comput. Phys. Commun*. 85(2), pp. 306-322, 1995

[91] Z. Yu, A. Raman, and S. Fan, "Fundamental limit of nanophotonic light trapping in solar cells," *Proc. Natl. Acad. Sci.* 107(41), pp. 17491-17496, 2010

[92] S. Duttagupta, F. Ma, B. Hoex, T. Mueller, and A. G. Aberle, "Optimised antireflection coatings using silicon nitride on textured silicon surfaces based on measurements and multidimensional modelling," *Energy Procedia,* 1578-83 2012

[93] W. Shockley and H. J. Queisser, "Detailed balance limit of efficiency of p-n junction solar cells," *J. Appl. Phys.*, 32(3), pp. 510-519, 1961

[94] C. H. Henry, “Limiting efficiencies of ideal single and multiple energy gap terrestrial solar cells,” *J. Appl. Phys.*, 51 (8), pp. 4494-4500, 1980